High-resolution modeling of ocean energy southwest of Japan

刘, 天然

https://hdl.handle.net/2324/4784726

High-resolution modeling of ocean energy southwest of Japan

Tianran Liu

January 2022

Abstract

The development of high-performance computing promotes the realistic simulations with high-resolution ocean models for fishery, navigation safety, ocean oil tracking, and many other applications. One example is the ocean power, which is the object of this thesis. The ocean owns enormous amounts of natural energy. The ocean renewable energy can be classified into five types: tidal energy, wave energy, current energy, thermal energy, and salinity gradient energy. Among them, the ocean current power can achieve high efficiency, and the Kuroshio current, as the strongest western boundary current, flows very close to Japan coast. In 2017, New Energy and Industrial Technology Development Organization (NEDO) and Ishikawajima-Harima Heavy Industries (IHI) carried out the Kuroshio current power generation experiment in the Tokara Strait. The ocean thermal energy conversion (OTEC) is also receiving more increasing attention because of its sustainability and environment-friendly characteristics. In addition, it is a stable resource that can generate power at all times. In 2013, an experimental plant called Okinawa OTEC Demonstration Facility was constructed in Kumejima Island. Therefore, this thesis attempts to estimate the ocean current power and thermal energy potential southwest of Japan using high-resolution regional ocean models, in order to select the proper site and depth for ocean renewable power plants. The impacts of Kuroshio large meander and tides are considered for better understanding. The thesis even tackles to enhance the accuracy of the model representing the thermal structure and velocity distribution by inverse modeling.

In Chapter 2, the DR_E model was used to represent the ocean state south of Japan. The ocean current power potential of the Kuroshio Current was estimated based on the simulation results. To choose the proper site for ocean current power generation experiment, three candidate areas were assessed by comparing the average current speed, the stability of the current vector, and the ocean current power potential. To study the impact of Kuroshio large meander, two experiments during the

periods with and without large meander were carried out. The model was validated by comparing the results with ADCP measurements across the Tokara Strait and south of Cape Shionimisaki.

The results showed that the average current speed around the Tokara Strait is the weakest of the three candidate areas. In addition, the current speed south of Cape Shionomisaki is the greatest during non-large-meander period. However, the average current speed and stability there decrease significantly when the Kuroshio large meander appears. By comparison, the current is stable and strong south of Cape Ashizuri regardless of the Kuroshio large meander. Thus, the area south of Cape Ashizuri is a promising site for ocean current power generation experiment, and the average ocean current power density there can reach 1 kW/m^2. However, an extraordinary strong and long-term Kuroshio large meander occurred since August 2017. The Kuroshio axis occasionally left far away from the coast south of Cape Ashizuri, which has not been expected by these results. Four criteria were selected to further determine the promising area south of Cape Ashizuri. We found that the maximum number of ocean current power plants constructed in the promising area is 378. The corresponding total power is about 458 MW, if we assume that the power for a single plant with 1.5 m/s current speed is 2 MW.

In Chapter 3, the ocean thermal energy potential around the Aguni Basin west of the Okinawa Island was estimated using DR_Ek model. The Aguni Basin lies near the eastern boundary of the Okinawa Trough where the tidal mixing is strong. The DR_Ek model was able to resolve the strong and complex tidal motions near the coast. To study the tidal effect, the simulations with and without tides were conducted. The simulated potential temperature and salinity were compared with the XCTD measurements near the OTEC plant on Kumejima Island.

In the Aguni Basin, the cold deep water intrusion cools the water, which is balanced by vertical eddy diffusion due to tidal mixing. Based on this deep layer thermal equilibrium, we proposed the perturbation method estimating the ocean thermal energy potential. This method and the modified Wick-Schmitt method were compared with the original Wick-Schmitt method and Nihous method.

The results showed that the Wick-Schmitt method and Nihous method overestimate the ocean thermal energy potential with the realistic turnover time in the Aguni Basin, implying that the methods and parameters used for global estimation may not be applicable to the Aguni Basin. On the other hand, the modified Wick-Schmitt and perturbation methods proposed in this study can improve the estimation. The results also showed that the ocean thermal energy potential in the Aguni Basin is five orders greater than the present mechanical limit. The strong and sustainable power generation is available near the northeastern slope of Kumejima Island within a short distance to the coast. The strong upwelling near the boundary of the Aguni Basin results from the strong tidal mixing. The large OTEC power can be also expected in the East China Sea due to vigorous tidal mixing.

It is noted that the surface warm water was assumed to keep its temperature much easier than the deep cold water, so the heat transport in deep layers of Aguni Basin was considered as the environmental limit of ocean thermal energy potential in this study. Thus, the temperature gradient in deep layers determines the potential instead of the temperature difference between surface and deep layers.

An ocean model reflecting realistic ocean state is critical for the estimation of ocean power potential. Thus, the satellite altimeter data assimilation based on the approximate Kalman filter was studied in Chapter 4. The domain of the DR_Ep model covers part of the shallow East China Sea shelf and deep Okinawa Trough southwest of Japan. Twin experiments were adopted to evaluate the data assimilation. The pseudo observations were generated along the tracks of AVISO multi-satellite altimeter data in the East China Sea.

To compare the data assimilation effects of surface and lateral boundary control, the process noises of the surface and lateral boundary forcings were separately determined by minimizing the root-mean-square difference of temperature. The results showed that traditional surface boundary control performs well in shallow area of the model domain, but the assimilation effects decay

rapidly to depths. By comparison, the lateral boundary control improves the surface and subsurface representation of the ocean state. The effect of lateral/surface boundary control can/cannot propagate to deep layers. The cross-spectral analysis indicated that the long-term variability with period longer than several weeks can be effectively improved by assimilating satellite altimeter data. Thus, other measurements should be assimilated in the meantime to promote the representation of the Kuroshio variations.

Acknowledgment

Contents

List of Figures

List of Tables

Chapter 1. General introduction

Recent development of high-performance computing (HPC) promoted the realistic simulations with high-resolution ocean models. Based on these models, swift and high-resolution ocean forecasting systems were constructed (e.g., Francis et al. 2020), which is beneficial to fishery, navigation safety, and so on.

Among such interesting applications, ocean renewable energy has been receiving more attention due to its environment-friendly property. The ocean owns enormous amounts of natural energy that may be divided into several forms: surface wave, current, tide, thermal and salinity gradient energy (Wick and Schmitt 1977). They are originated from solar energy except the tidal power. To promote the development and deployment of industrial, energy, and environmental technologies, Japanese government set up the New Energy and Industrial Technology Development Organization (NEDO) in 2003. This office inspires us to create a high-resolution regional ocean simulation system facilitating the selection of proper position for the future's construction of ocean renewable energy plants around Japan.

For example, the kinetic energy of ocean currents are able to be converted into electricity by turbines. In 2017, NEDO and Ishikawajima-Harima Heavy Industries (IHI) started the Kuroshio current power generation experiment in the Tokara Strait (see http://www.nedo.go.jp/). As one of the major western boundary currents in the world, the Kuroshio current is from the eastern coast of the Philippines and flows along the continental slope of the East China Sea. After that, this current turns to the east and flows along the south coast of Japan. Then it merges into the North Pacific Current. The most striking phenomenon of the Kuroshio current south of Japan is the large meander which has been extensively studied in the previous literature (e.g., Kawabe 1980). These studies suggest that the Kuroshio large meander can significantly change the ocean state south of Japan. As

a result, the selection of proper site for ocean current power density in this area should concern about the large meander.

To harness the thermal energy, ocean thermal energy conversion (OTEC) was proposed by d'Arsonval (1881) for the first time. This technology generates electricity using the temperature difference between warm surface and cold deep waters in the ocean. In 2013, an experimental OTEC plant was constructed in Kumejima Island (see http://otecokinawa.com/). Tidal mixing may play a key role around the Okinawa Trough which has complicated topography. It leads to large vertical diffusivities of 3 to 4 order-of-magnitude greater than the typical values in the open ocean (Nishina et al. 2016). Therefore, regional ocean thermal energy potential near the coast is difficult to be estimated using methods and parameters for global ocean, and the tidal effect should be involved into the estimation of ocean thermal energy potential.

As quasi-routine ocean observations, satellite altimeter data were commonly assimilated into the ocean models to improve the simulations (e.g., Hirose et al. 2005). The effect of data assimilation relies much on the determination of process noise regardless of linear or nonlinear capabilities. The process noise has been frequently ascribed to surface meteorological conditions, whose influence may decay rapidly to depths. However, the representation of deep ocean state is crucial for the estimation of ocean thermal energy potential. Thus, we attempt to improve the satellite altimeter data assimilation by comparing the surface and lateral boundary conditions data assimilations.

In the previous studies, satellite altimeter data were assimilated into the regional ocean models around Japan using various methods (e.g., Kamachi et al. 2004; Miyazawa et al. 2012). As one of optimal data assimilation schemes, the ensemble Kalman filter proposed by Evensen (1994) was frequently employed in nonlinear models with enormous degrees of freedom. However, the ensemble Kalman filter requires large computational cost. Therefore, the approximate Kalman filter based on Fukumori and Malanotte-Rizzoli (1995) will be adopted in this study.

In this thesis, a high-resolution regional ocean forecasting system considering the long-term (Kuroshio large meander) and short-term (tides) impacts will be set up, in order to facilitate the objective selection of proper sites for constructing the ocean renewable energy plants. This thesis will also improve the satellite altimeter data assimilation into regional ocean model based on the approximate Kalman filter, in order to enhance the accuracy of the high-resolution regional ocean forecasting system.

This thesis is organized as follows. The ocean current power near the south coast of Japan is estimated, and the impact of the Kuroshio large meander is also studied in Chapter 2. The ocean thermal energy potential in the Aguni Basin near the eastern boundary of the Okinawa Trough is estimated using different methods, and the tidal effect is studied as well in Chapter 3. The satellite altimeter data assimilation in the region southwest of Japan is studied based on an approximate Kalman filter, and the lateral boundary condition data assimilation is compared with the traditional surface meteorological condition data assimilation in Chapter 4. This thesis is concluded in the last chapter.

Chapter 2. High-resolution modeling of the Kuroshio current power south of Japan

2.1 Introduction

Ocean currents provide enormous amounts of energy and have potential worldwide capability (Finkl and Charlier 2009). The kinetic energy of ocean currents can be converted into electrical energy by turbines. Therefore, ocean current power (or marine current power) is anticipated to provide a new stable energy source. Actually, the electrical power efficiencies of some turbines exceed 40% (Roberts et al. 2016). Historically, an ocean current turbine was installed in the Gulf Stream off Fort Lauderdale in 1985 (Davis et al. 1986). An ocean current power plant has also been planned to be built in the Kuroshio between Taitung and Green Island, Taiwan, with a power capacity up to 30 MW (Chen 2010). Recently, New Energy and Industrial Technology Development Organization (NEDO) and Ishikawajima-Harima Heavy Industries (IHI) carried out the Kuroshio current power generation experiment in the Tokara Strait, Japan (see http://www.nedo.go.jp/). The electrical power output exceeded 100 kW using a floating twin-turbine prototype system with each diameter of 11 m.

To choose the proper site for ocean current power generation experiment, observations and simulations have been conducted in previous studies. Acoustic Doppler current profiler (ADCP) measurements and corresponding simulations around the Tokara Strait indicated that the area near the southern coast of Nakanoshima (NA) is a promising choice for power plants (Komaki et al. 2013). The ADCP measurements conducted at Miyake Island, located 180 km south of Tokyo, indicated that the current is strong enough for ocean current power generation (Kodaira et al. 2013). The analysis of ocean current velocity measurements from drifters suggested that the region near Vietnam is promising for an ocean current power plant (Chang et al. 2015).

In the region south of Japan, the Kuroshio is the strongest western boundary current of the North Pacific Ocean. The Kuroshio flows from the eastern coast of the Philippines, across the East China Sea and the Tokara Strait. The current then flows along the south coast of Japan and merges into the North Pacific Current. The Kuroshio current field south of Japan has been intensively investigated in previous studies. The average current speed at the Kuroshio axis south of Japan, as estimated by satellite altimetry and drifting buoys, ranges from 0.65 to 1.45 m/s (Ambe et al. 2004). Previous studies have investigated the dynamics involved in the formation of the Kuroshio large meander (Usui et al. 2008, 2013; Li et al. 2014).

Through these previous studies, three candidate areas south of Japan for ocean current power generation are identified: around the Tokara Strait, south of Cape Ashizuri (AS), and south of Cape Shionomisaki (SH). The reason why these three candidate areas are chosen is that they are close to the land or island (< 30 km). Other areas where strong and stable currents exist are far away from the coast, so it is very difficult to construct power generation plants and transfer the electrical power. Long-term ADCP measurements around the Tokara Strait indicate that the average current speed exceeds 0.8 m/s near the north coast of Kuchinoshima (KU) and near the south coast of NA at a depth less than 60 m, making the area fit for ocean current power generation (Komaki et al. 2013). The variations of the Kuroshio in the Tokara Strait can be divided into long-term and short-term variabilities (Feng et al. 2000). In the area south of AS, the volume transport of the Kuroshio across the ASUKA-line ranges from 29.0 to 40.2 Sv (1 Sv = 10^6 m^3/s), which is relatively stable (Nagano et al. 2010). The quasi-periodic variation of the Kuroshio path south of AS was studied, and the period is between 100 and 150 days (Kashima et al. 2009). Additionally, in the region south of the Kii Peninsula, a bifurcation current was observed by ADCP measurements along the coast, but this current disappeared when the large-meander path was formed (Takeuchi et al. 1998). It suggested that the large meander can impact the current field south of the Kii Peninsula significantly.

5

However, besides these measurements, few studies have simulated the current field of the Kuroshio south of Japan with high horizontal resolution and estimated the ocean current power potential.

In the present study, the current field is accurately represented using a high-resolution ocean model to help choose proper sites for ocean current power generation experiment. One important measure may be the time-mean, unidirectional current over 1 m/s ($\sim$ 0.5 kW/m^2) which is the typical threshold proposed for instance by the Headquarters for Ocean Policy of the Japanese government. The simulation results are validated by comparison with ADCP measurements. The current field and ocean current power potential around the three candidate areas are presented by horizontal maps and section views. In Section 2.2, the model and observation data are described briefly. The simulation results are validated through comparison with ADCP measurements in Section 2.3. The current field and estimated ocean current power are then shown and analyzed in Section 2.4. The conclusion and discussion are presented in Section 2.5.

2.2 Model configuration

The DREAMS_Energy (DR_E) model used in this study is based on the Research Institute for Applied Mechanics ocean general circulation model (RIAMOM), which was originally developed by Lee et al. (2003). RIAMOM is a three-dimensional primitive equation ocean model with hydrostatic balance and Boussinesq approximation, and it adopts the Arakawa B-grid and z-coordinate. Several similar models based on RIAMOM such as DREAMS_Marginal (DR_M) (Hirose et al. 2013) and DREAMS_Coastal (DR_C) (Hirose et al. 2017) have been developed.

The shape of the bottom relief is probably the most crucial boundary condition for modeling the detailed ocean current variation. The root-mean-square difference between the raw measurements or fine-scale data of total water depth and the interpolated or gridded products is shown for the Tokara Strait in Table 2-1. Since the three datasets of ETOPO1, GEBCO08, and JTOPO30 come with large

differences to the individual measurements, we averaged JTOPO30 and ETOPO1 data to reduce the uncertainty for the model topography. The combined data indeed show the smaller root-mean-square difference to the independent measurement of KGSU.

The model covers a hexagonal domain southwest of Japan (Fig. 2-1b). The horizontal resolution of the model, 1/60° longitude by 1/75° latitude, is sufficient to resolve the islands around the Tokara Strait. The major parameters used in this model are listed in Table 2-2. The Smagorinsky scheme (Smagorinsky 1963) is adopted to calculate the horizontal viscosity and diffusion coefficients. The mixed-layer scheme developed by Noh and Kim (1999) is adopted to calculate the vertical viscosity and diffusion coefficients. The model adopts the Meso-Scale Model (MSM) meteorological forcing provided by the Japan Meteorological Agency (JMA). The MSM model adopted hydrostatic balance at first, but it was updated to the nonhydrostatic version after September 2004. It is also noted that the horizontal resolution is changed from 10 to 5 km in March 2006. The MSM model runs four times a day, but becomes eight times a day from March 2006. This means the forcing data are heterogeneous and may be more and more accurate in time.

It is well known that the Kuroshio large meander has significant impact on the current field south of Japan. The bimodel frequency distribution of the Kuroshio axis south of Japan (Fig. 5 in Taft 1972) suggests the fundamental change in the current structure of Kuroshio between the two cases with and without the large meander. Thus, the presence of large meander is distinguished in this study. The first experiment simulates from January 2007 to September 2015, designated as period N, during which the non-large-meander path is formed. The second experiment simulates from July 2004 to July 2005, designated as period L, during which the large-meander path is formed. The temperature, salinity, sea level, and velocity components at the open boundary are given by the DR_M at 1-h interval. Because simulated temperature and salinity tend to be higher than the climatological data such as World Ocean Atlas (WOA) or Japan Oceanographic Data Center (JODC), the time-mean or biased components of all open boundary conditions are calibrated

7

by a more reliable assimilation dataset of "Four-dimensional Variational Ocean Reanalysis for the Western North Pacific over 30 years" (FORA-WNP30) (Usui et al. 2017). The horizontal resolution of the DR_M is 1/12° longitude by 1/15° latitude, and its topography is shown in Fig. 2-1a. In addition, a biased experiment without the FORA-WNP30 correction is also carried out, and the results will be compared in Section 2.3. The numerical simulations are conducted with the supercomputer SX-ACE at Tohoku University. The CPU number is 64, making it take about 2 days for 1-year integration based on the Message Passing Interface (MPI).

The moving vessel ADCP data are provided by the Kagoshima University Faculty of Fisheries and Wakayama Prefectural Fisheries Experimental Station. The former data are gathered along the ferry line between Kagoshima and Naha crossing the Tokara Strait (indicated by the solid line in Fig. 2-1b) from 2005 to 2007 (e.g., Komaki et al. 2013), while the latter are taken in the area south of SH (the solid rectangle in Fig. 2-1b) from 2003 to 2014. In Section 2.3, the hourly averaged zonal and meridional velocities at 50 m depth, where we assume the ocean current power generators work, will be compared with these data.

2.3 Model validation

The average current speed simulated by DR_E is compared with ADCP measurements. For period N (L), the results from October 2007 (August 2004) to September 2015 (July 2005) are used in the validation.

The ADCP measurements across the Tokara Strait (Fig. 4 in Komaki et al. 2013) show that the strongest current at 50 m depth occurs between Yakushima (YA) and KU, where the average current speed reaches 86 cm/s. The second strongest current at 50 m depth occurs between NA and Suwanosejima (SU), where the average current speed reaches 73 cm/s.

The model successfully represents the multi-core structure across the Tokara Strait (Fig. 2-2). During period N, in agreement with the previous measurements, the strongest current at 50 m depth occurs between YA and KU. However, the average current speed of 69 cm/s is lower than the previous measurements. The average current speed at 50 m depth between NA and SU, 65 cm/s, is more consistent with the measurements. The average current speed across the Tokara Strait during period L has similar distribution as in period N.

The stability of the current vector was defined as the ratio of the magnitude of the vector average velocity to the scalar average magnitude of the velocity (Egawa et al. 1993). It was also used in Komaki et al. (2013). The formula calculating the stability is as follows:

$$S = \frac{\sqrt{\bar{u}^2 + \bar{v}^2}}{\overline{\sqrt{u^2 + v^2}}} \tag{2-1}$$

where $\bar{u}$ is the average zonal velocity component, $\bar{v}$ is the average meridional velocity component, and $\overline{\sqrt{u^2 + v^2}}$ is the average current speed. The value of stability ranges from zero to unity. The stability with the value of unity means the current direction has no change. The larger the value of stability, the more stable the current direction. Therefore, the stability of the current vector may have a large value, although the current speed is not stable. The results show that the distribution of the stability across the Tokara Strait (Fig. 2-2) is lower than those of the measurements (Fig. 5 in Komaki et al. 2013).

The average zonal velocity and standard deviation at the measurement points within the selected area south of SH are compared with the measurements at Wakayama Prefecture (Fig. 2-3). A total of 116 ADCP measurements are taken over period N, while only 17 are taken over period L. During period N, the simulation results are consistent with the ADCP measurements, especially for the average zonal velocity. The maximum velocity is between 33.0°N and 33.2°N, where the

average zonal velocity is close to 140 cm/s. Regarding standard deviation, the measurements between 33.2°N and 33.4°N are approximately 50 cm/s, but the simulation results are greater than 55 cm/s. This difference suggests that the simulation overestimates the amplitude of the Kuroshio axis shift south of SH. During period L, both the measurements and the simulation results shows low current speed near the coast. However, the model significantly underestimates the standard deviation north of 32.8°N. In the biased experiment, the average zonal velocity is greatly underestimated for both periods N and L. This means that the FORA-WNP30 correction is critical for the simulation.

In addition, a comparison of the simulation with 60-day (from April 21, 2015) ADCP measurements deployed between YA and KU (130.37°E, 30.02°N) indicates that the simulated average southeastward current speed (68 cm/s) at 50 m depth is lower than those of the measurements (77 cm/s); the phase of the current speed is also different (not shown). This discrepancy may be due to the chaos of the Kuroshio axis shift. However, the comparisons of the simulation with the long-term measurements suggest that the model can be used to estimate the statistical variables of the current south of Japan.

2.4 Results

This section shows the simulation results of the current field and the estimated ocean current power south of Japan.

2.4.1 Current field at 50 m depth

The average current vectors at 50 m depth are shown in Fig. 2-4. The average current vectors around the Tokara Strait reveal that the impact of the islands on the Kuroshio current field is

significant. The current through the channel between the adjacent islands is strong, and the direction is nearly perpendicular to the line linking them. This result indicates that a high-resolution model that can resolve the islands is critical for representing the currents around the Tokara Strait. Additionally, a cyclonic circulation forms in Tosa Bay which is between Shikoku Island and the Kuroshio during period N, but disappears during period L. It was ascribed to the onshore–offshore shift of the Kuroshio axis and the irregular topography (Awaji et al. 1991) and the frontal wave propagation (Kuroda et al. 2013). The Kuroshio axis shows large deviation from the coast east of 134°E during period L. The latitude of the Kuroshio axis south of SH is approximately 33.3°N during period N, but becomes roughly 32.5°N during period L.

The average current speed at 50 m depth is shown in Fig. 2-5. The pattern east of 134°E shows a large difference between periods N and L. However, the Kuroshio axis west of that longitude is relatively stable. The maximum average current speed in the East China Sea increases during period N. The maximum speeds southeast of Kyushu Island and the region east of 135.8°E become larger during period L. In the Tokara Strait, the strongest current occurs between KU and NA during period N, but between SU and Akusekijima (AK) during period L. For the areas near the south coasts of AS and SH, the average current speed exceeds 100 cm/s during period N. However, the Kuroshio axis east of 134°E deviates from the coast during period L. As a result, the average current speed greatly decreases south of SH during period L.

The stability of the current vector at 50 m depth is shown in Fig. 2-6. The value is large near the Kuroshio axis. For the Tokara Strait, the value between the adjacent islands is large. This result indicates that the current direction is stable between the adjacent islands. Notably, the stability in the area south of SH during period L is much lower than that in the area south of AS. This difference is due to the Kuroshio large meander south of SH.

2.4.2 Current field across the sections of the three candidate areas

To choose the proper site for the ocean current power generation experiment, three candidate areas are examined: around the Tokara Strait, south of AS, and south of SH. The average current speed and the stability of the current vector indicate that the presence of the large-meander path has little impact on the current field around the Tokara Strait (Fig. 2-2). However, the impact of the islands is significant. The strongest current occurs between YA and KU, where the stability of the current vector reaches 0.9 during period N.

The average current speed and the stability of the current vector across the area south of Cape AS (133°E) are shown in Fig. 2-7. The maximum average current speed of the shallow water area adjacent to the coast with depth less than 200 m exceeds 130 cm/s during period N and 120 cm/s during period L. The average current speed decreases as the depth increases. Additionally, the stability of the current vector at 50 m depth exceeds 0.97 in the shallow water area during periods N and L. This result indicates that the direction of the current is stable near the coast, making this area favorable for ocean current power generation.

The average current speed and the stability of the current vector across the area south of SH (135.8°E) are shown in Fig. 2-8. Unlike in the other two candidates, the large meander has a great impact on the current field in this area. During period N, the Kuroshio axis is close to the coast, but it deviates from the coast during period L. The average current speed decreases as the depth increases. The stability of the current vector at 50 m is greater than 0.9 in the area adjacent to the coast during period N, but less than 0.5 during period L. This result indicates that the Kuroshio large meander should be distinguished when studying the current field south of SH.

2.4.3 Ocean current power estimation

$$P = \frac{1}{2}\rho_0 \sqrt{u^2 + v^2}^3 \qquad (2\text{-}2)$$

The ocean current power density is calculated by Eq. 2-2, where ρ_0 is the average seawater density (1025 kg/m^3), u is the zonal velocity, and v is the meridional velocity. The average ocean current power density at 50 m depth is shown in Fig. 2-9. Compared with that of the areas south of AS and SH, the ocean current power density is much lower around the Tokara Strait. The maximum (0.482 kW/m^2) occurs between KU and NA during period N, while the maximum (0.433 kW/m^2) occurs between SU and AK during period L. For the region south of Shikoku Island, the maximum is 2.152 kW/m^2 at 133.88°E, 32.74°N during period N and 2.083 kW/m^2 at 133.81°E, 32.62°N during period L. As a result, the maximum decreases by roughly 3% and its position moves southwestward by only 14 km, when the large-meander path is formed. The large meander has less impact on the ocean current power south of Shikoku Island, west of 134°E. The current power density at 50 m depth exceeds 1 kW/m^2 within 23 km from AS even for period L. However, the large meander has a significant impact in the region south of the Kii Peninsula. The average ocean current power southeast of SH reaches 2.227 kW/m^2 at 136.14°E, 33.26°N separating the large meander period, but less than 0.1 kW/m^2 during period L.

The standard deviation of the ocean current power density at 50 m depth is shown in Fig. 2-10. The pattern of the standard deviation is similar to the average ocean current power density. The value becomes generally larger downstream along the Kuroshio path. During period N, the maximum power density (1.725 kW/m^2) appears southeast of SH. This result may be due to the high-frequency meridional shift of the Kuroshio axis. During period L, the position of the maximum moves southeastward. For the Tokara Strait, the maximum standard deviation occurs between KU and NA during periods N (0.611 kW/m^2) and L (0.507 kW/m^2).

The ocean current power density values for 20, 50, and 80% cumulative frequency at 50 m depth of the areas south of AS (133°E) and SH (135.8°E) are shown in Fig. 2-11. The vertical axis is the latitude and the distance from the nearest coast (unit: km). As the distance increases, the mean

13

value and standard deviation increase sharply at the beginning, except for SH during period L. For the area south of AS during period N, the distance between the coast and the area where the ocean current power density exceeding 1 kW/m^2 has a 50% chance ranges from 17 to 42 km. However, it ranges from 29 to 53 km during period L. This means that the Kuroshio axis shifts only 10 km southward when the large-meander path is formed south of AS. For the area south of SH, the impact of large meander is much larger than the area south of AS. Proper sites for ocean current power generation should be where the average ocean current power density and stability of the current vector are large, but the standard deviation, distance from the coast, and the impact of large meander are small. Therefore, the area south of AS, where the stable nearshore power density is found around 1 kW/m^2 (20–30 km offshore only), is relatively a rational choice. However, the horizontal resolution of the model used in this study is approximately 1.5 km, so the simulation results may be inaccurate near the coast.

2.5 Conclusions and discussion

In the present study, a high-resolution ocean model was used to simulate the current field south of Japan, and the assessment of ocean current power potential of the Kuroshio was carried out. Two experiments were designed to distinguish the impact of the Kuroshio large meander. The average current speed, the stability of the current vector, and the ocean current power potential were calculated. It is noted that the actual electrical power obtained by turbines is expected to be smaller than that presented by power maps in the present study. Roughly speaking, electrical power efficiency may be around 40% (Roberts et al. 2016). The model results were validated by comparison with ADCP measurements. Three candidate areas were assessed to help choose the proper site for ocean current power generation experiment: around the Tokara Strait, south of AS, and south of SH.

The results show that the average current speed in the area south of SH is normally the greatest of the three candidates during period N, but decreases significantly during period L. In the Tokara Strait, the current is the weakest among the three candidate areas. In the region south of Shikoku Island, the current is stable south of AS, but the Kuroshio axis east of 134°E deviates from the coast during period L. The area near the south coast of AS is promising for ocean current power generation. It is noted that the ocean current speed we focused on is the average value, instead of the maximum value which may be much greater than the former one.

We confirmed the strong influence of the island topography in the Tokara Strait. The current across the channel between the adjacent islands is strong, and the direction is nearly perpendicular to the line linking them. The maximum ocean current power density occurs between NA and KU during period N. In period L, the maximum density area slightly shifts southward and occurs between SU and AK.

For the area south of AS, the Kuroshio axis hardly deviates from the coast regardless of the period N or L in our experiments. An earlier study of Fujimoto et al. (1985) also reported that the short durations (1–3 years) of the large meander did not allow the separation of Kuroshio from the vicinity of AS. Thus, the shallow area 20–30 km offshore south of AS with the stable current power density around 1 kW/m^2 has long been a promising site for ocean current power generation. However, it should be noted that the long duration ($\sim$ 5 years) of the large meander actually caused the long-term offshore deviation of the Kuroshio current axis from AS in the late 1970s (Fujimoto et al. 1985).

During period L, the current speed was very weak near SH (Fig. 2-9). We can easily confirm the loss of current energy from the coastal area with the Kuroshio large meander by definition. Using long-term reanalysis data, Usui et al. (2013) found that the durations of the large meanders were shorter if the Kuroshio transport increased. Sakamoto et al. (2005) pointed out that the eastward current of Kuroshio will accelerate if the atmospheric carbon dioxide concentration

increases based on their long-term numerical experiments. Therefore, we can expect that the durations of the Kuroshio large meander become shorter with the climate warming in the future. The area south of SH tends to be more attractive for ocean current power generation.

To further select the candidate area for ocean current power generation south of AS, we choose 4 criteria; the average current speed and its stability at 50 m during period N, the water depth, and the distance to the nearest coast (Fig. 2-12). The shades indicate the area satisfying the corresponding criterion. The threshold values are 1 m/s, 0.97, 200 m, and 20 km, respectively. The area satisfying all the four criteria are presented by the black shade in Fig. 2-12d, which consists of 42 model grids. If we assume the minimum horizontal interval between two ocean current power plants is 500 m, 9 plants can be constructed in each model grid. As a sum, the maximum number of ocean current power plants constructed in the promising area is 378. The corresponding total power is about 458 MW, if we assume the power for a single plant with 1.5 m/s current speed is 2 MW. It should be noted that the power is expected to decrease by about 20% in the south of AS when the large-meander appears.

In addition, the statistical quantities of current field and power density estimated by this DR_E model have been published in the website of Kagoshima University (http://me.oce.kagoshima-u.ac.jp/).
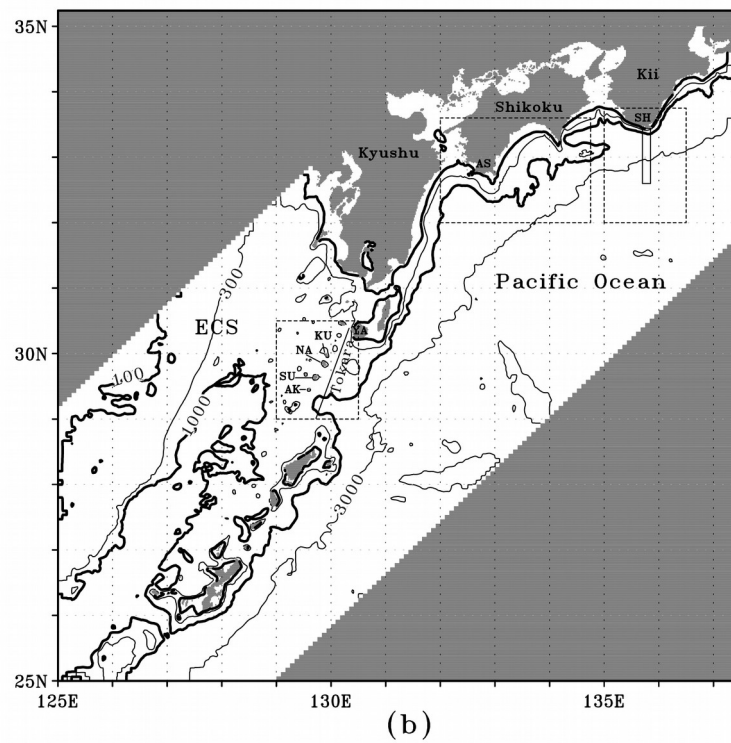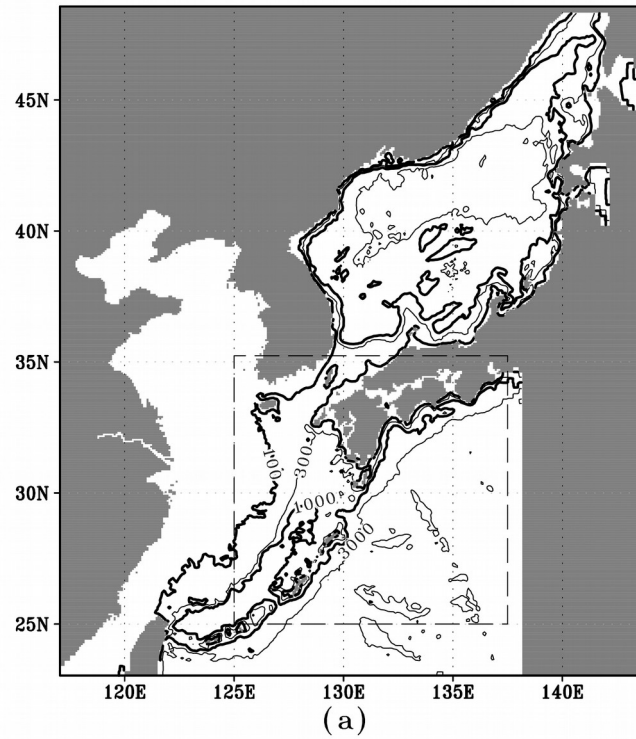
Fig. 2-1 Model topography (unit: m). a DR_M, b DR_E (ECS East China Sea, AS Cape Ashizuri, SH Cape Shionomisaki, YA Yakushima, KU Kuchinoshima, NA Nakanoshima, SU Suwanosejima, AK Akusekijima)
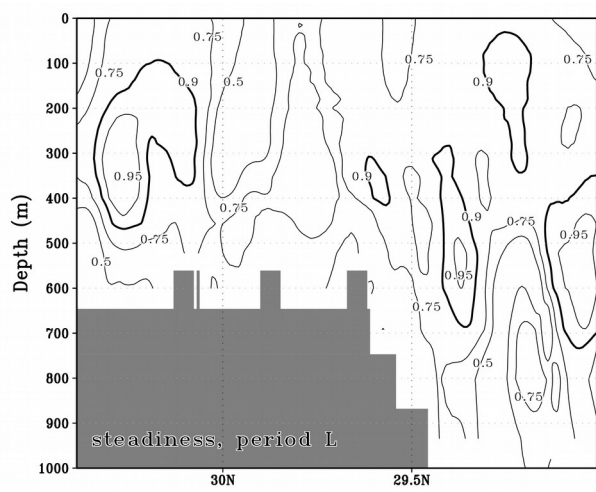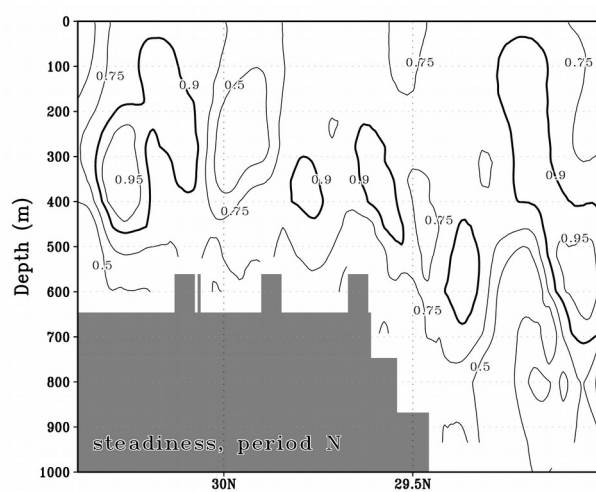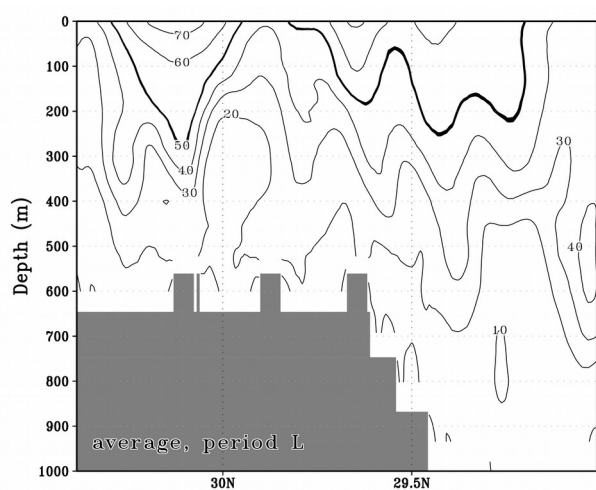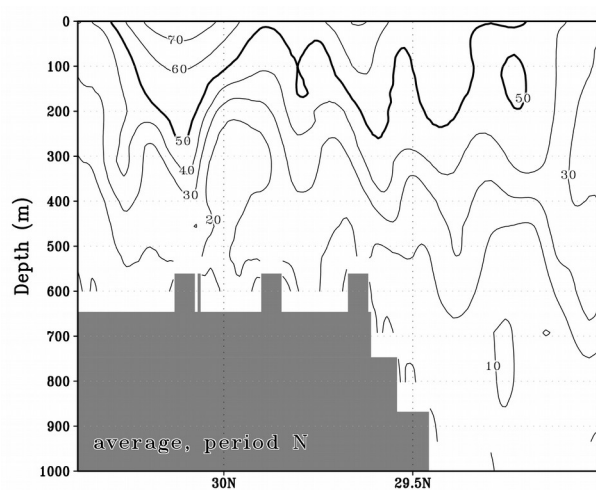
Fig. 2-2 Average current speed (unit: cm/s) and the stability of the current vector across the Tokara Strait (the solid line in Fig. 2-1b) during periods N and L (YA Yakushima, KU Kuchinoshima, NA Nakanoshima, SU Suwanosejima)
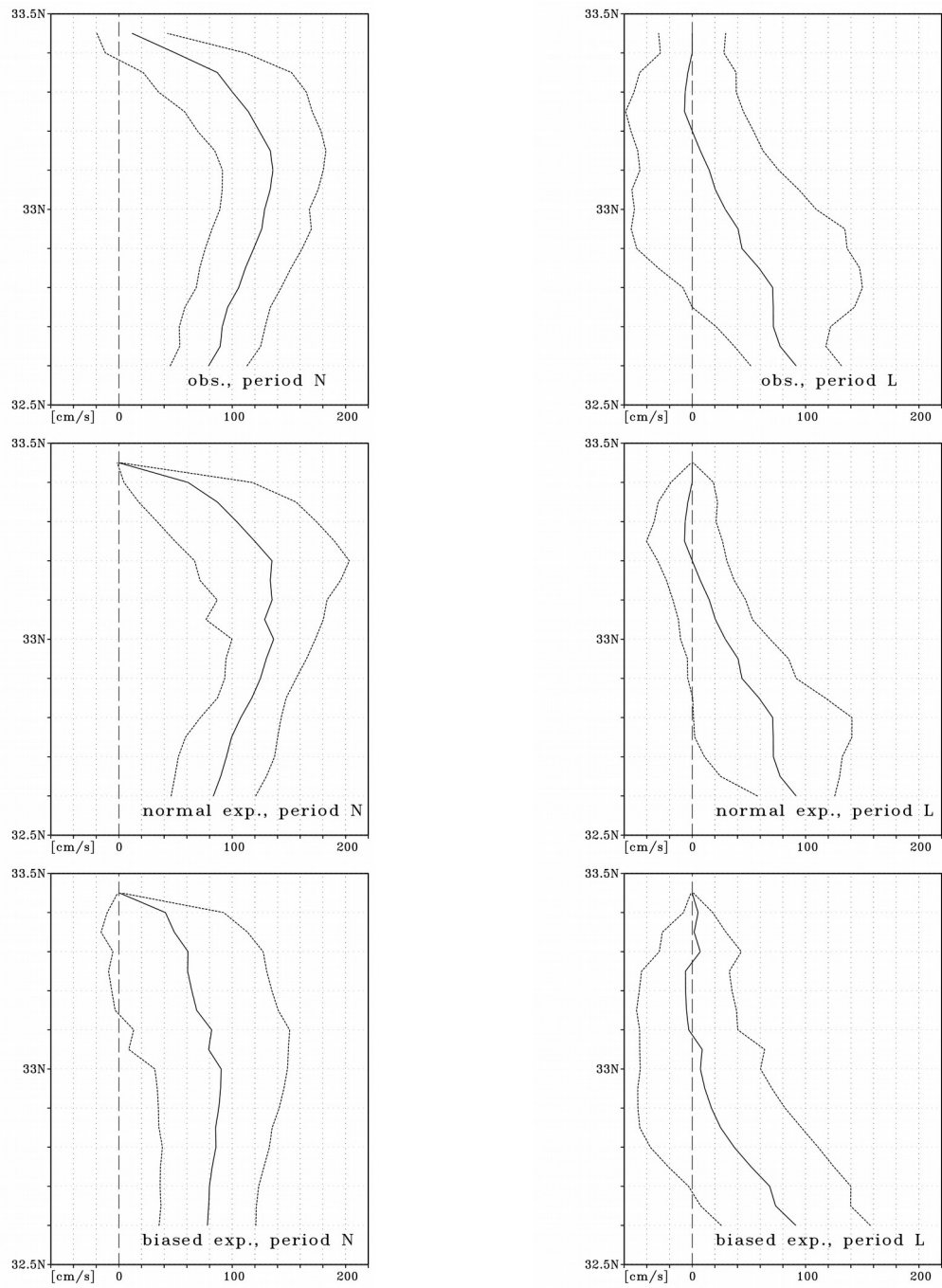
Fig. 2-3 Observed (by the Wakayama Prefectural Fisheries Experiment Station) and simulated

(normal experiment and biased experiment) average zonal velocity components (solid line) with the

envelope of standard deviations (dotted line) at 50 m depth south of Cape Shionomisaki (the solid

rectangle in Fig. 2-1b) during periods N and L
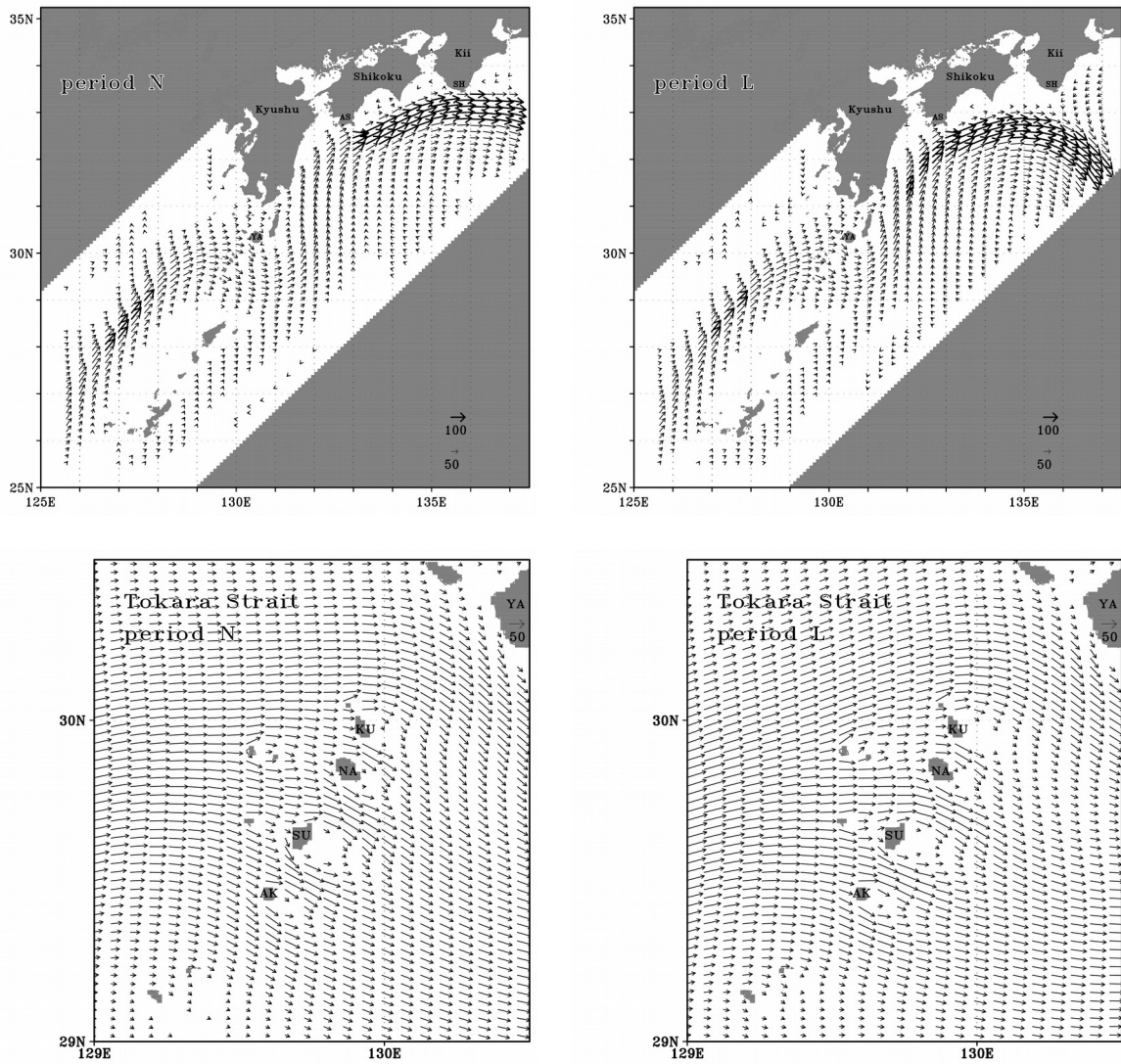
Fig. 2-4 Average current vectors (unit: cm/s) at 50 m depth during periods N and L (Currents with magnitude ≥ 100 cm/s are shown by thick vectors, while currents with magnitude ≥ 10 cm/s but < 100 cm are shown by thin vectors. AS Cape Ashizuri, SH Cape Shionomisaki, YA Yakushima, KU Kuchinoshima, NA Nakanoshima, SU Suwanosejima, AK Akusekijima)
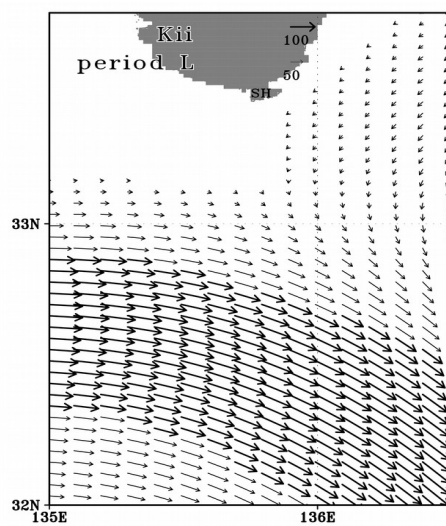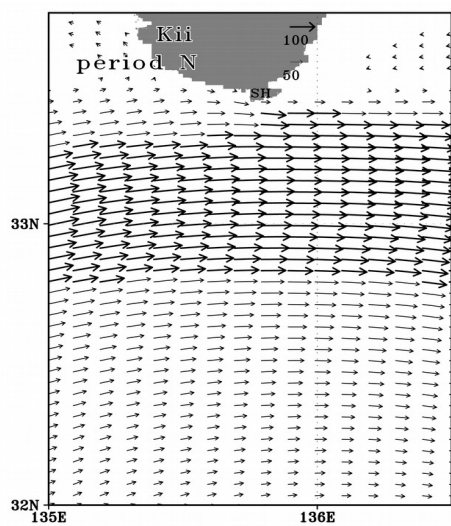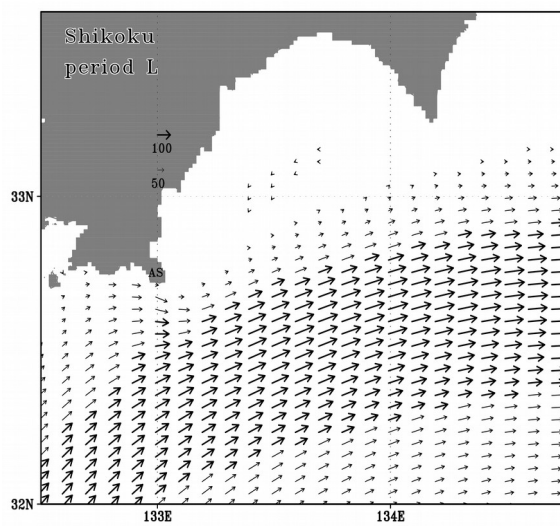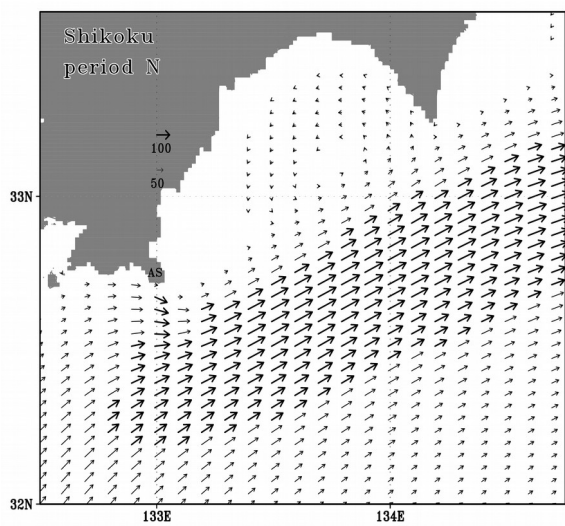
Fig. 2-4 continued
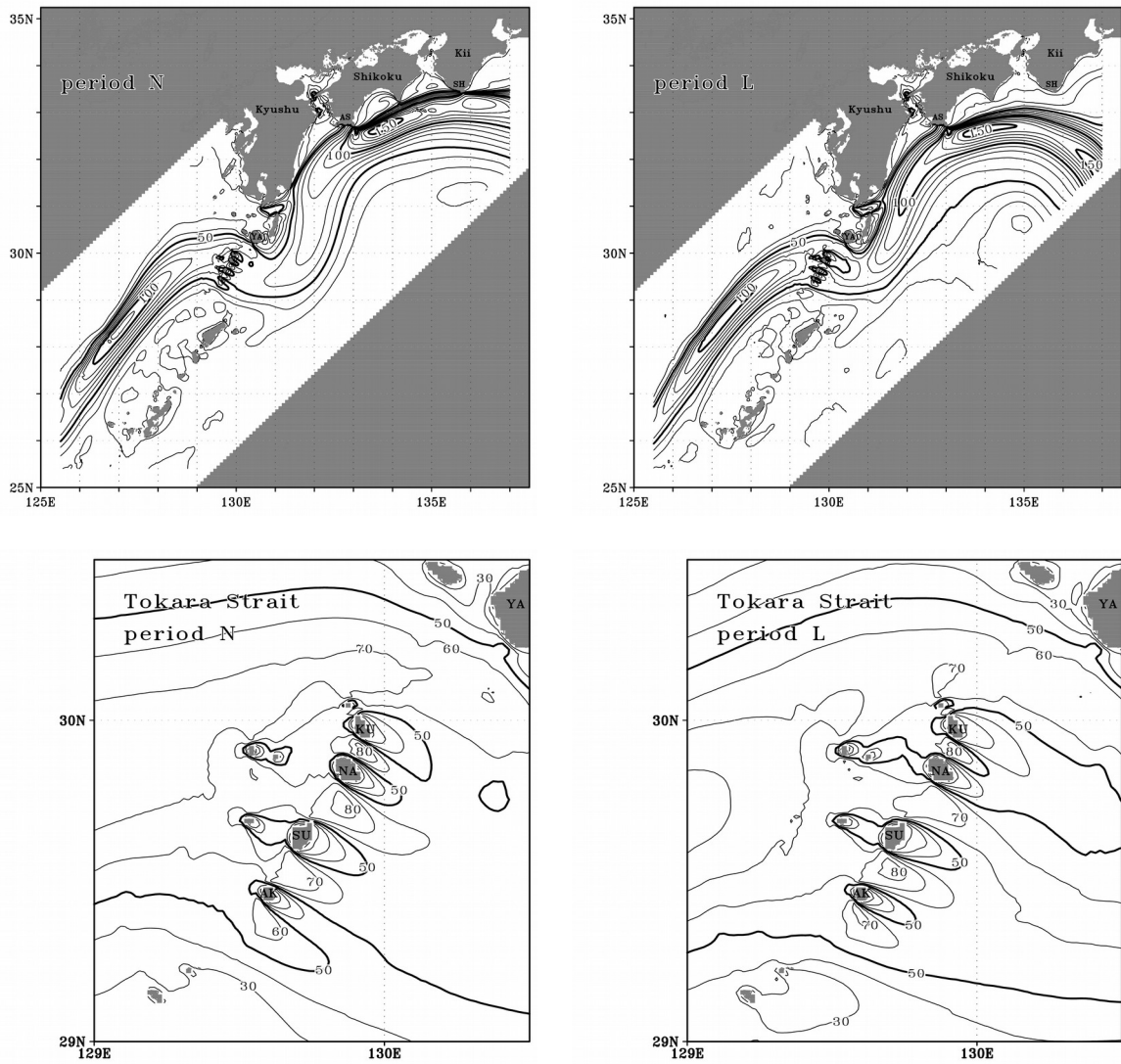
Fig. 2-5 Average current speed (unit: cm/s) at 50 m depth during periods N and L (ECS East China

Sea, AS Cape Ashizuri, SH Cape Shionomisaki, YA Yakushima, KU Kuchinoshima, NA

Nakanoshima, SU Suwanosejima, AK Akusekijima)

Fig. 2-5 continued

23
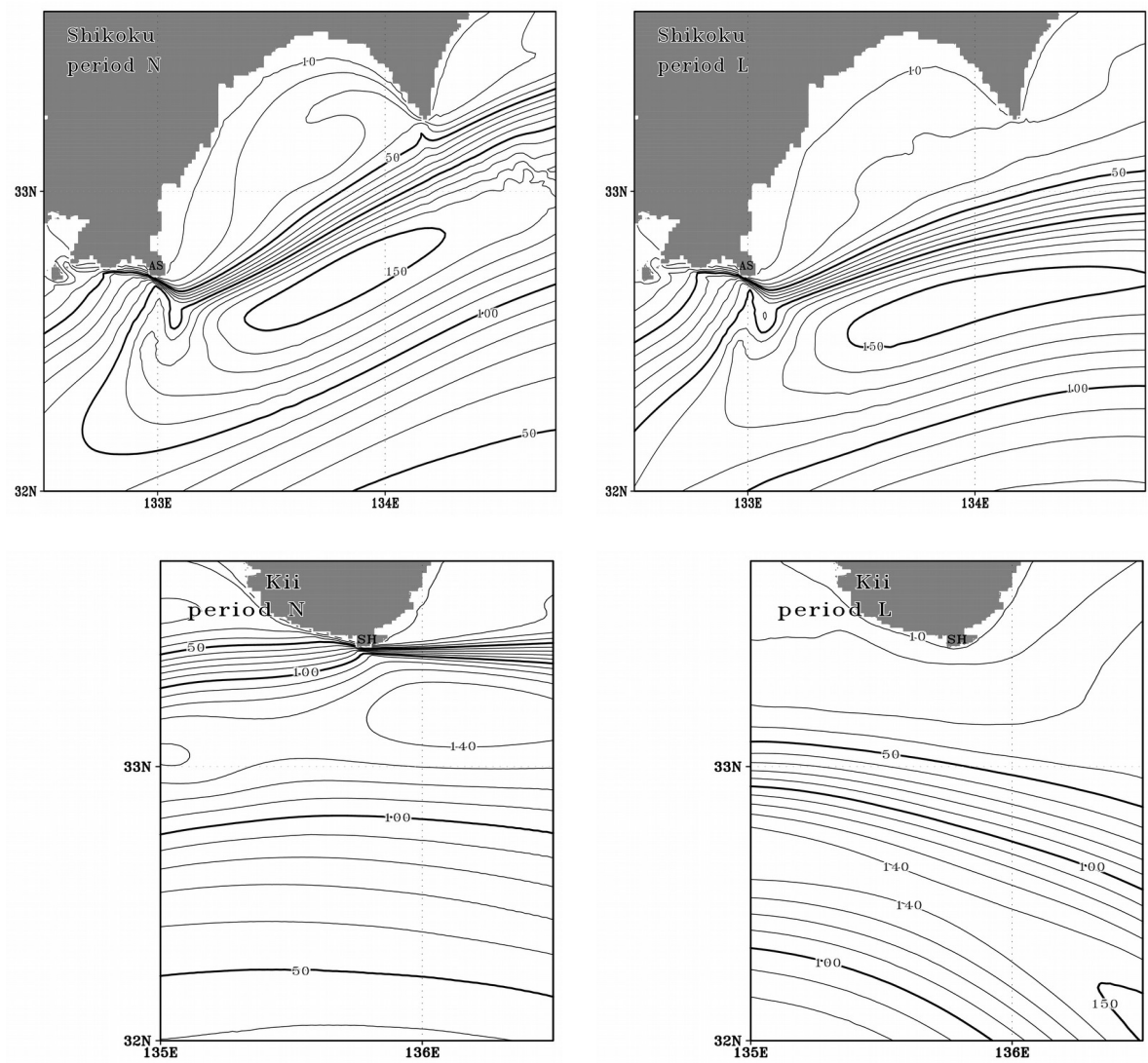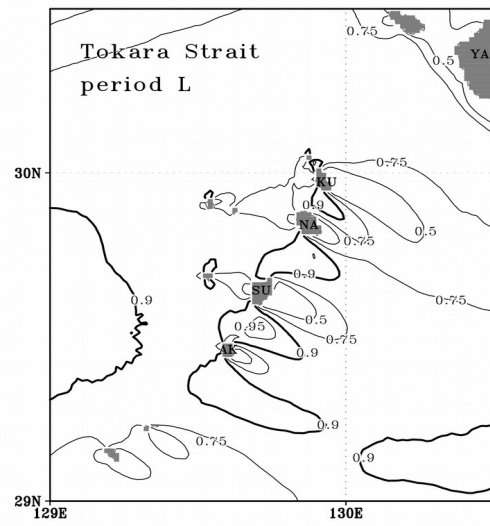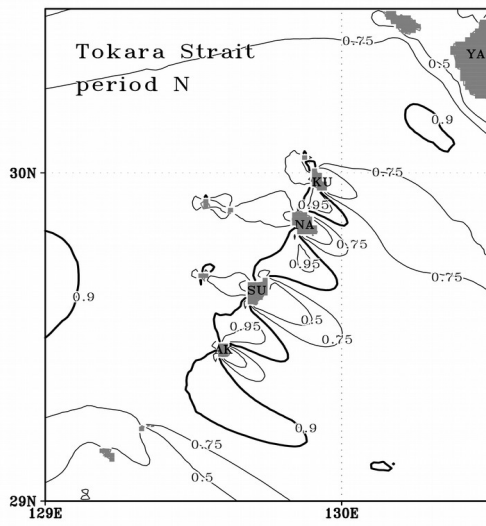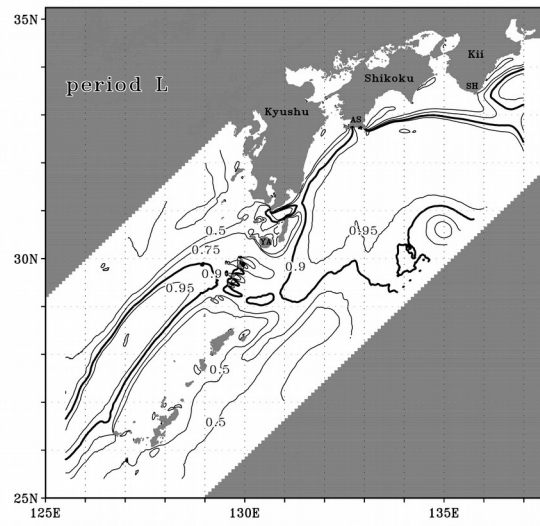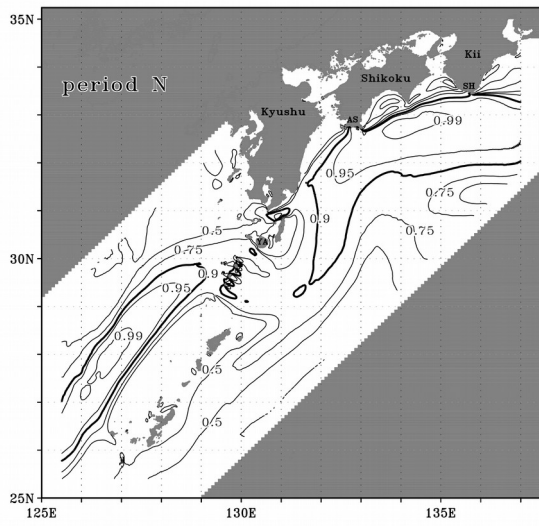
Fig. 2-6 Stability of the current vector at 50 m depth during periods N and L (ECS East China Sea,

AS Cape Ashizuri, SH Cape Shionomisaki, YA Yakushima, KU Kuchinoshima, NA Nakanoshima,

SU Suwanosejima, AK Akusekijima)
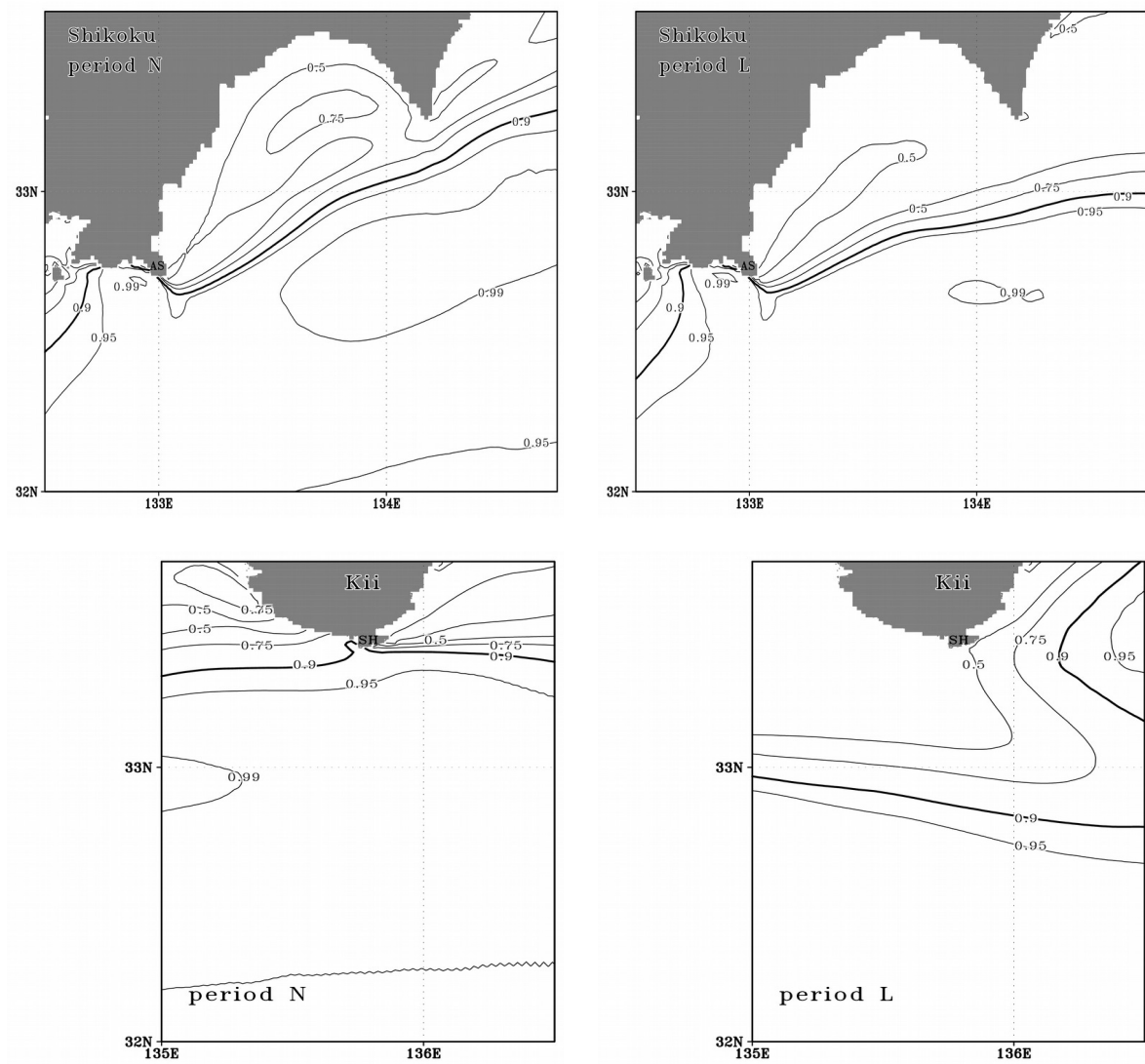
Fig. 2-6 continued
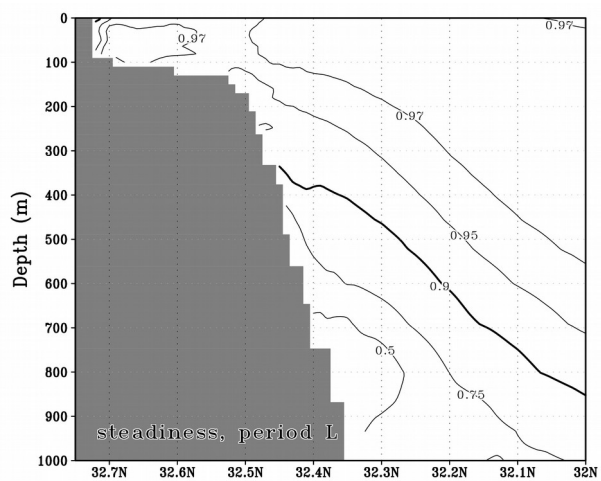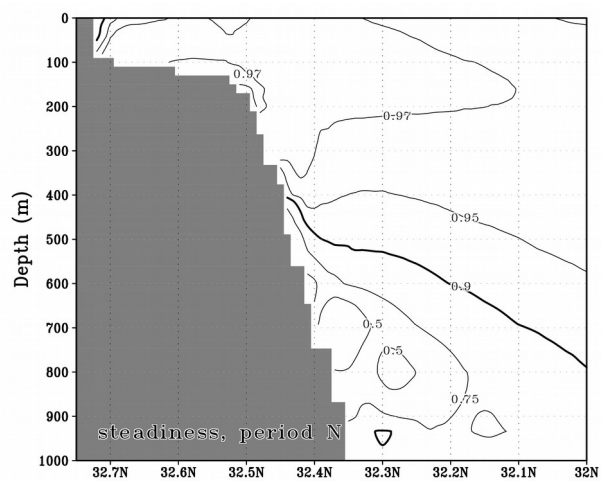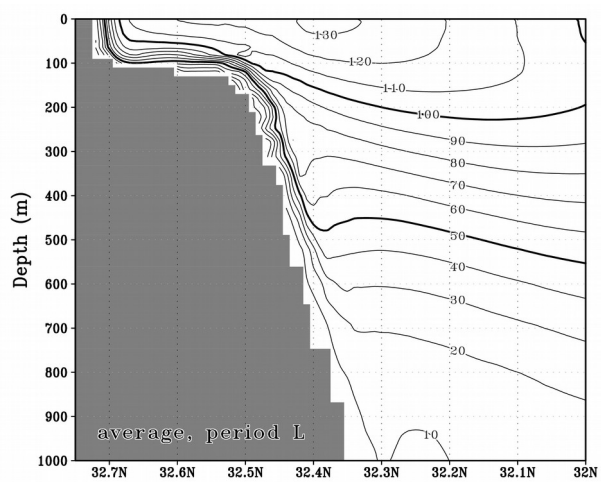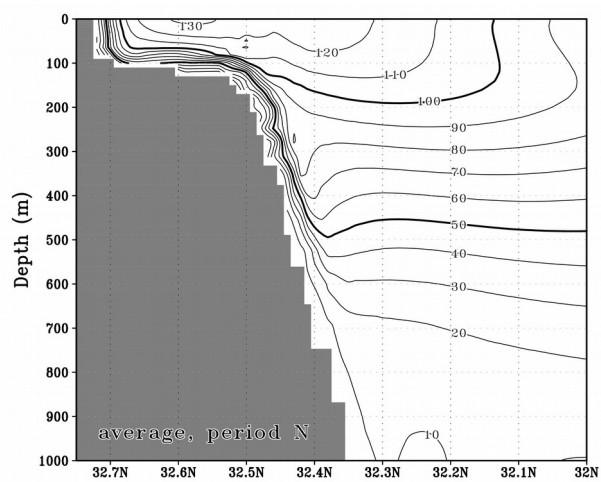
Fig. 2-7 Average current speed (unit: cm/s) and stability of the current vector across the area south

of Cape Ashizuri (133°E) during periods N and L
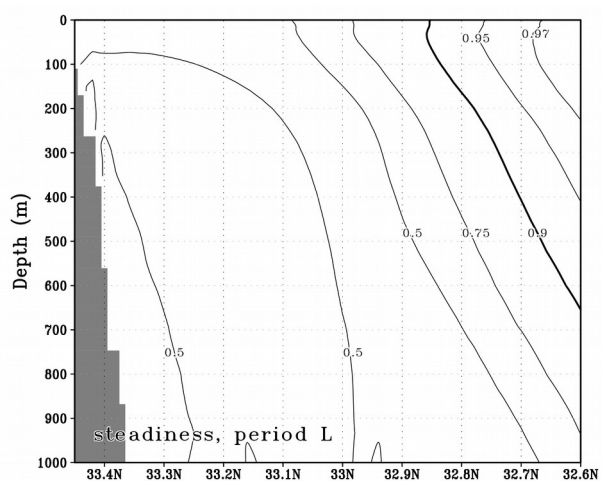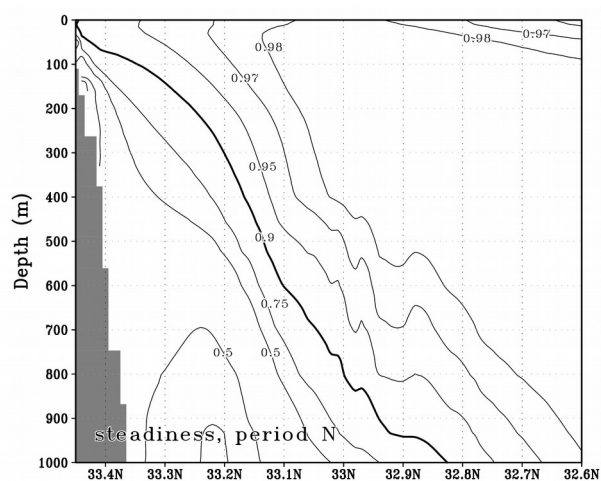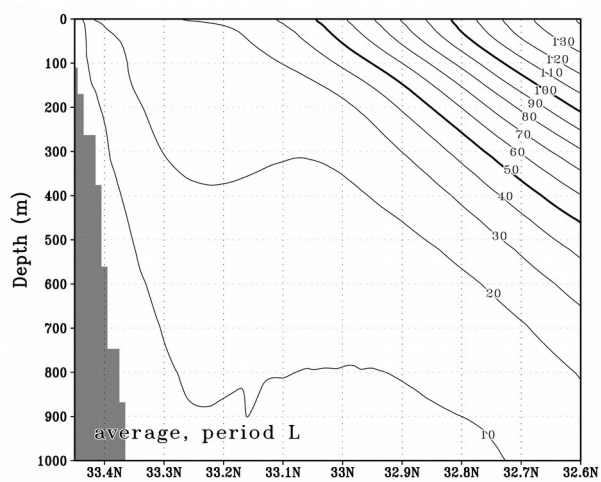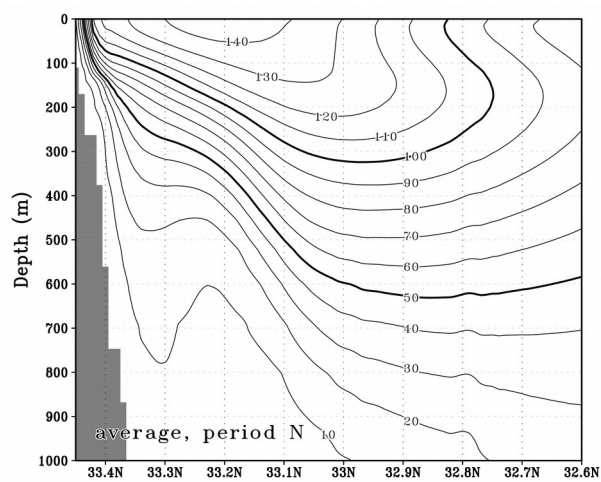
Fig. 2-8 Average current speed (unit: cm/s) and stability of the current vector across the area south

of Cape Shionomisaki (135.8°E) during periods N and L
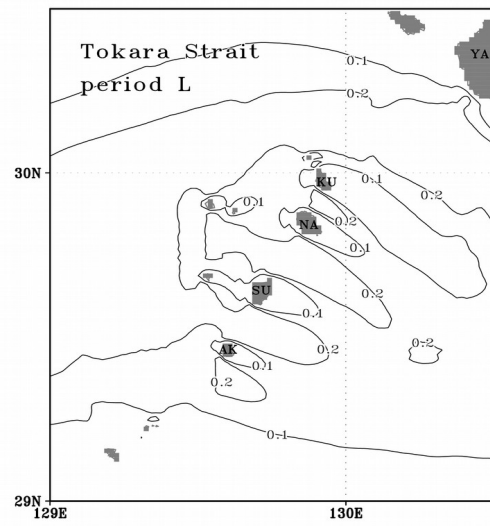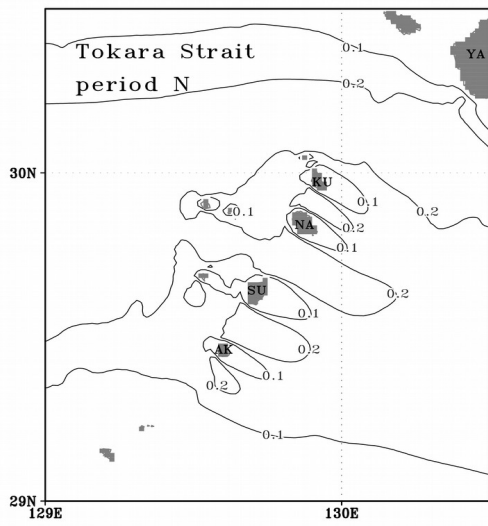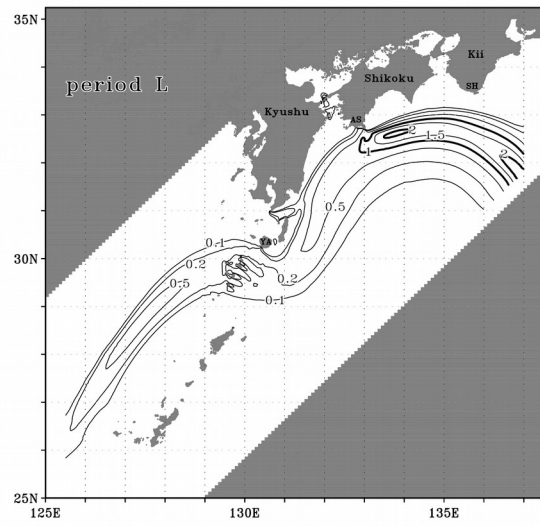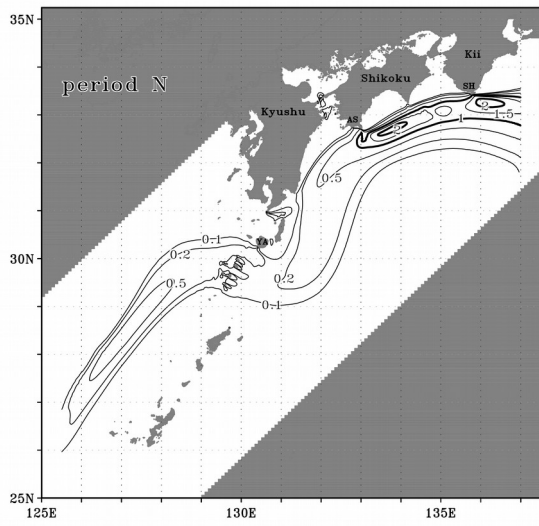
Fig. 2-9 Average ocean current power density (unit: kW/m^2) at 50 m depth during periods N and L

(ECS East China Sea, AS Cape Ashizuri, SH Cape Shionomisaki, YA Yakushima, KU

Kuchinoshima, NA Nakanoshima, SU Suwanosejima, AK Akusekijima)

28
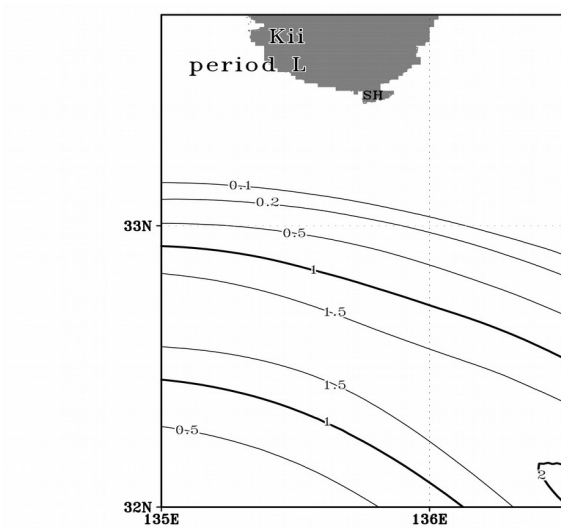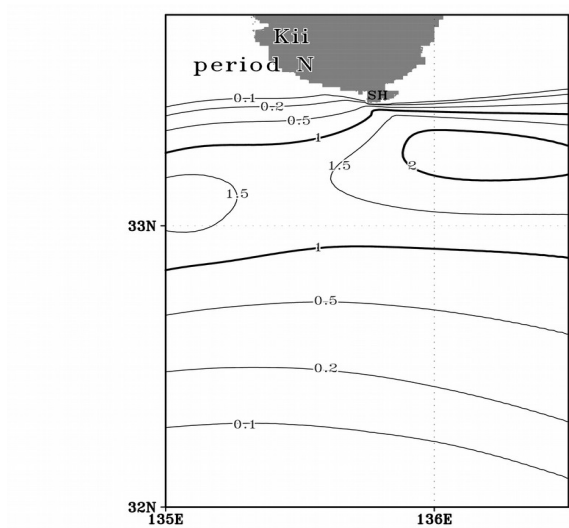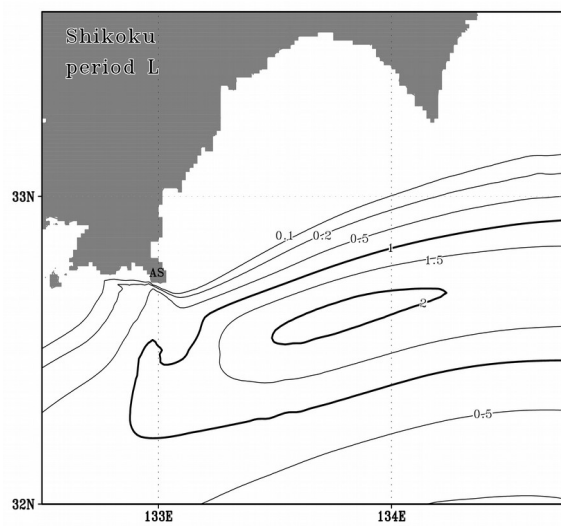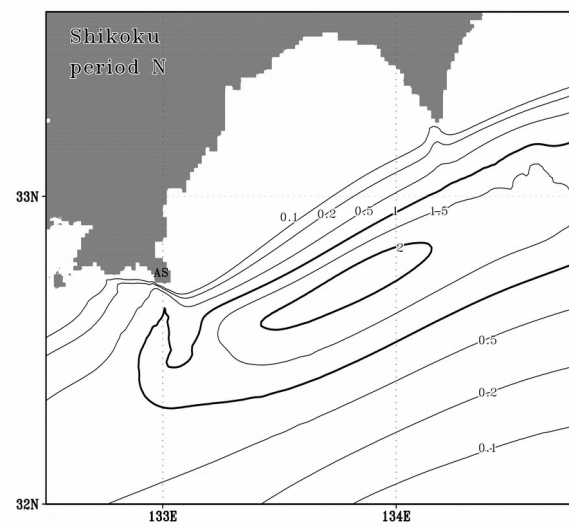
Fig. 2-9 continued
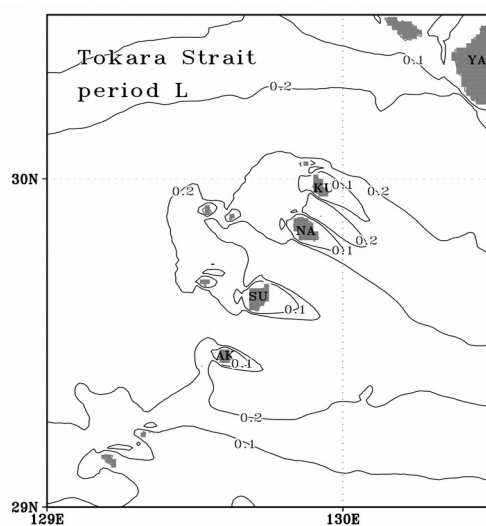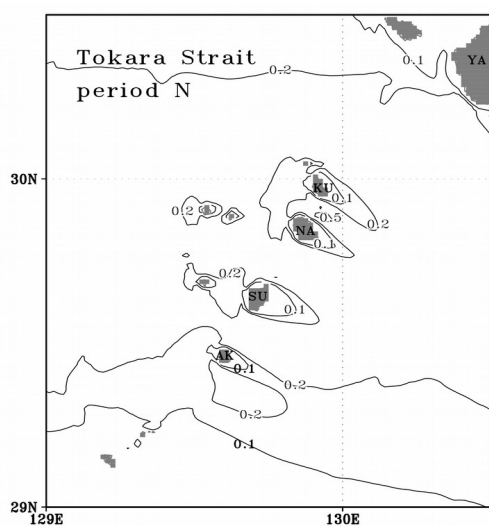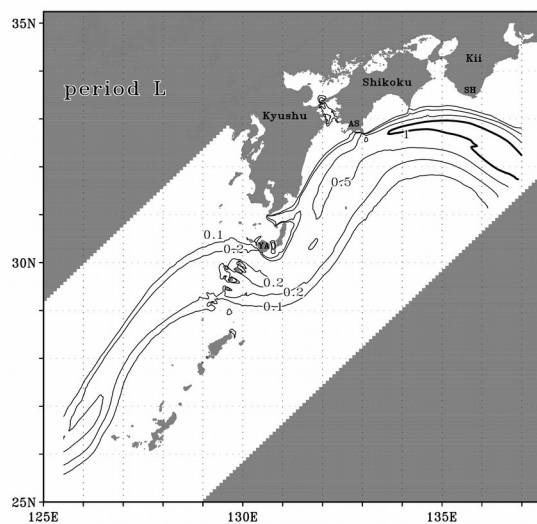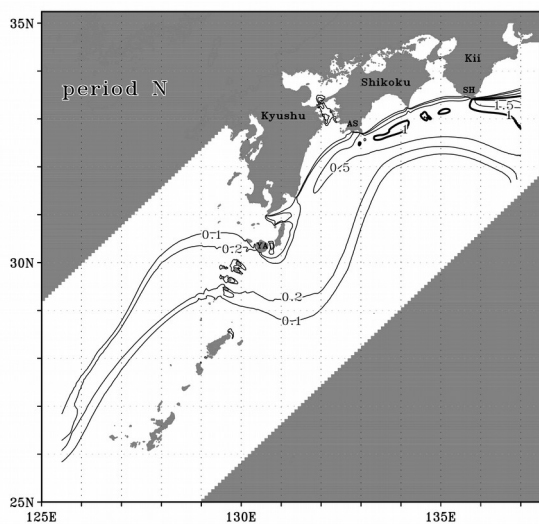
Fig. 2-10 Standard deviation of ocean current power density (unit: kW/m^2) at 50 m depth during periods N and L (ECS East China Sea, AS Cape Ashizuri, SH Cape Shionomisaki, YA Yakushima, KU Kuchinoshima, NA Nakanoshima, SU Suwanosejima, AK Akusekijima)
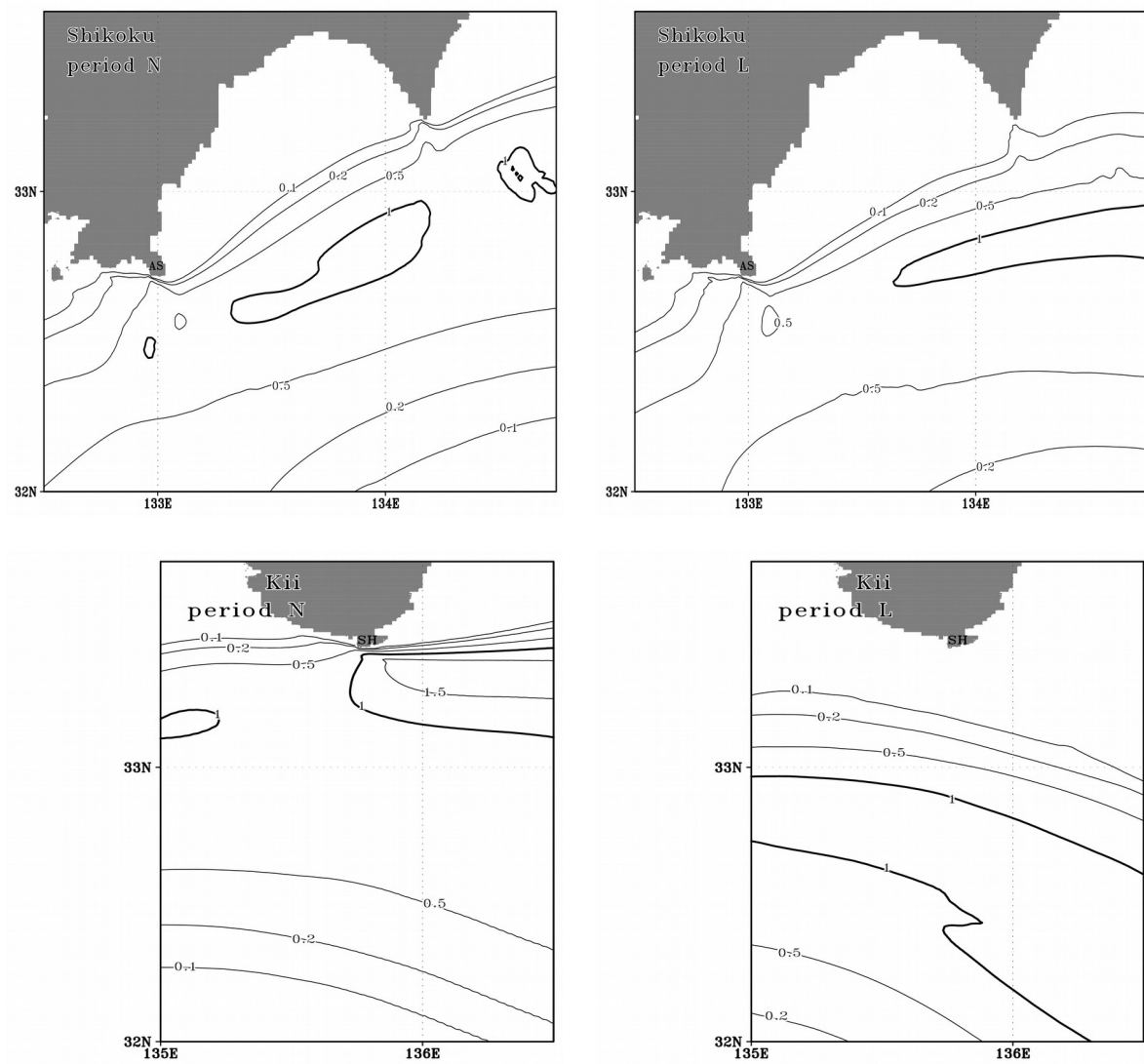
Fig. 2-10 continued
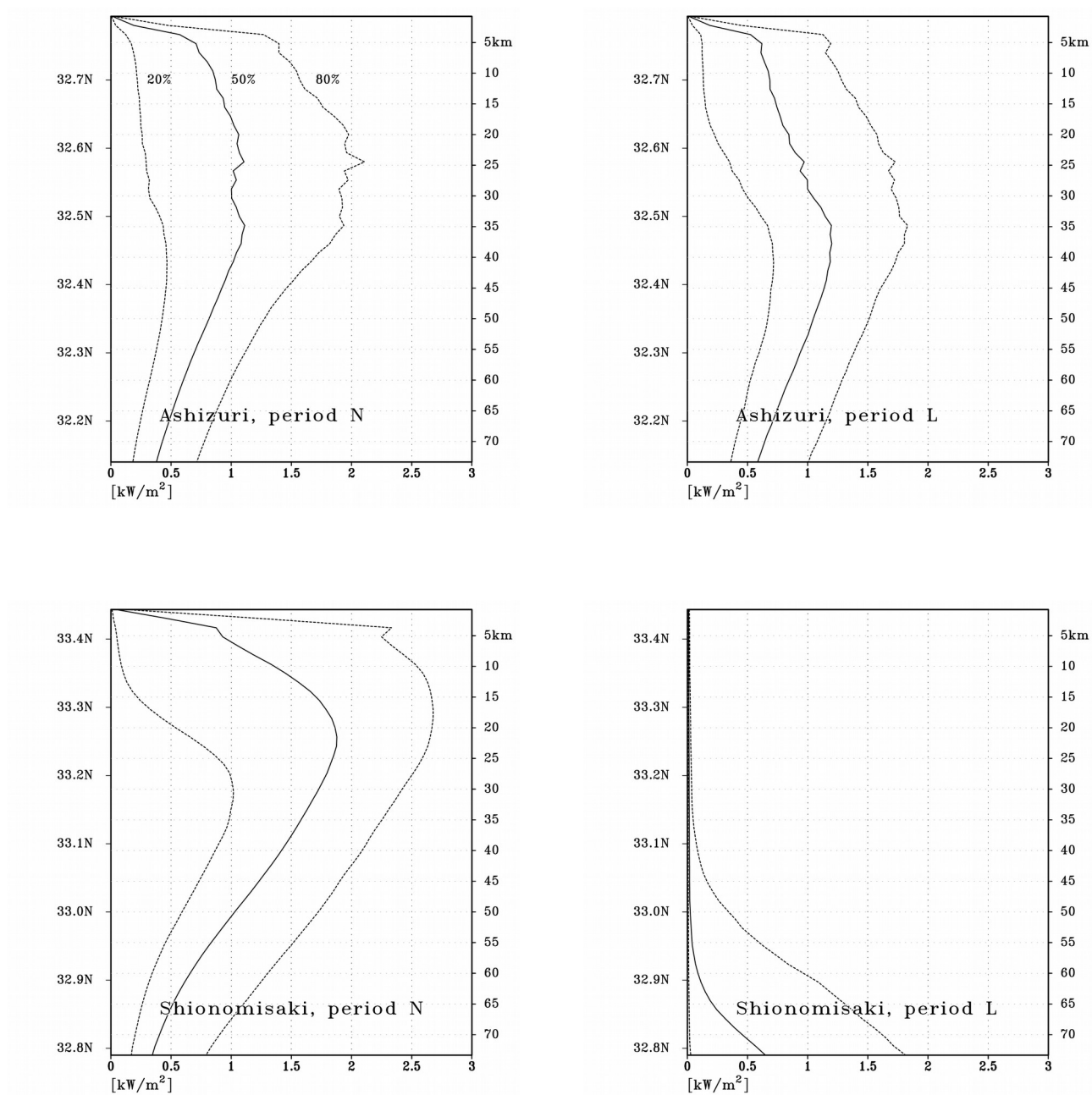
Fig. 2-11 Ocean current power density value of 20% (left dotted line), 50% (solid line), and 80% (right dotted line) cumulative frequency at 50 m south of Cape Ashizuri (133°E) and Cape Shionomisaki (135.8°E) during periods N and L
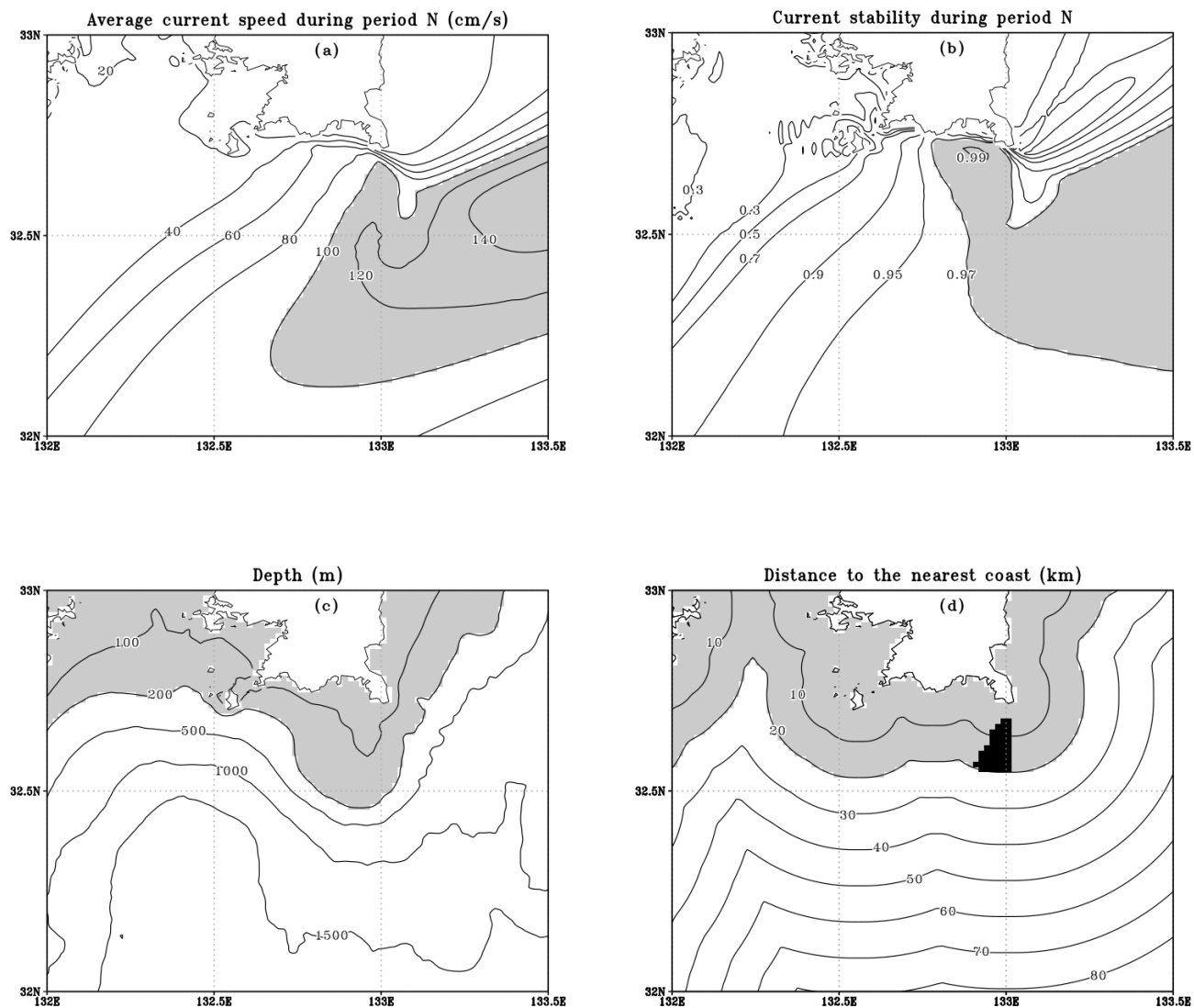
Fig. 2-12 The values of each criterion used for selecting the candidate sites of ocean current power generation experiment south of Cape Ashizuri: the average current speed (a) and stability (b) at 50 m during period N, the depth (c), and the distance to the nearest coast (d). The shade indicates the area satisfying the corresponding criterion. The black shade in (d) shows the area satisfying all the four criteria

Table 2-1 Root-mean-square difference of topography (unit: m) ETOPO1: 1 arc-minute grid, www.ngdc.noaa.gov/mgg/global/global.html GEBCO08: 1 arc-minute grid, www.gebco.net/data_and_products/gridded_bathymetry_data/version_20100927/ JTOPO30: 30 arc-second grid, www.mirc.jha.jp/products/finished/JTOPO30/JEGG500: 500 m grid, non-interpolated, www.jodc.go.jp/data_set/jodc/jegg_intro_j.html, sample number: 4415 KGSU: single-beam sonar measurements by Kagoshima University, sample number: 350

Gridded datasets	Fine-scale measurements (129.5°E–130.5°E, 29.4°N–30.4°N)	
	JEGG500	KGSU
ETOPO1	20.19	37.33
GEBCO08	38.39	36.26
JTOPO30	29.28	35.58
0.5 ETOPO1+0.5 JTOPO30	21.07	35.21

Table 2-2 Model parameters

Model parameters	Values
Zonal grids number	750
Meridional grids number	768
Vertical levels number	40
Internal time step	15 s
External time step	1.25 s
Smagorinsky constant	0.17
Horizontal Prandtl number	2.0
Vertical Prandtl number	0.8333
Bottom drag coefficient	0.0027

Chapter 3. Estimation of ocean thermal energy potential in the Aguni Basin

3.1 Introduction

Ocean thermal energy conversion (OTEC) is a technology that generates electricity using the temperature difference between warm surface and cold deep waters in the ocean. The power potential of OTEC depends on the equilibrium of the net gain of heat at the tropical and subtropical oceans and the net loss of heat at high latitude oceans. In a closed-cycle OTEC system (Fig. 3-1) first proposed by d'Arsonval (1881), a working fluid is evaporated by warm surface water and condensed by cold deep water in a Rankine cycle. Then a turbine is driven by the working fluid to generate electrical power. The ammonia is usually selected as the working fluid because of its low boiling point. The open-cycle OTEC system first proposed by Claude utilizes seawater as the working fluid directly, which differs from the closed-cycle (Finney 2008). As a marine renewable resource, OTEC is attracting increasing attention because of its sustainability and environment-friendly characteristics. It is also a stable resource that can generate power at all times, in contrast to the variable renewable energy such as solar and wind power. In addition, the open-cycle OTEC plants can produce fresh water as a byproduct. The other uses of OTEC and its environmental impact were discussed in (Finney 2008).

Several land-based OTEC plants have been constructed to date. The first OTEC plant in the world was constructed and used the waters around Cuba in 1930, although no net power was generated (Claude 1930). In 2013, an experimental plant called Okinawa OTEC Demonstration Facility (black triangle in Fig. 3-2b) was also constructed in Kumejima Island (see http://otecokinawa.com/). Its maximum power can reach 100 kW with 13,000 m^3/day intake rate. Furthermore, a 100 kW OTEC plant in Hawaii became operational in 2015 and was able to power 120 homes in Hawaiian Islands (see https://www.makai.com/). Besides these land-based OTEC

plants, an ocean thermal energy project called NEMO was made to construct a floating OTEC power plant off the west coast of Martinique in the Caribbean Sea. In 2019, a 10 MW floating OTEC power plant was planned to build off the coast of southern China. Recently, to reduce the capital cost, a floating structure of OTEC power plant from a converted oil tanker has been designed near Siberut Island, Indonesia (Adiputra et al. 2020).

The global ocean thermal energy potential was estimated by previous studies. Wick and Schmitt (1977) focused on the supply of deep cold water and estimated the maximum global power potential to be 2 TW (1 TW = 10^{12} W). The global OTEC resources were also estimated using numerical models. The OTEC power density in the Atlantic Ocean was estimated to be about 0.08 W/m^2 using an interhemispheric box model by Nihous (2007a). This result is greater than the global average of 0.03 W/m^2. Based on 1-D ocean models (Nihous 2005, 2007b), the maximum potential limited by the formation rate of cold deep water was estimated to be 3–5 TW. The value increases by approximately 60% with separate evaporator and condenser discharges (Nihous 2018). The result became one order of magnitude greater using a 3-D ocean model with a horizontal resolution of 4° (Rajagopalan and Nihous 2013c), but it dropped to 12–14 TW using the same model with higher horizontal resolution (Rajagopalan and Nihous 2013a,b). A coupled atmosphere-ocean model was used to allow the feedback between ocean and atmosphere, and the value became 8 to 10.2 TW (Jia et al. 2018). If the mechanical efficiency is excluded, these values may become even larger. The natural vertical heat flux in the deep ocean is actually the order of hundred TW (Cummins et al. 2016). However, the deep heat transport is yet smaller than the surface one, which reaches a few thousand TW. The formation of strong surface heat transport is due to vigorous downward shortwave radiation at the low latitude and compensating upward longwave radiation and turbulent flux at high latitude oceans. Therefore, the deep heat transport should be the critical limit as the OTEC potential for the full-depth environment of the oceans.

Recently, the OTEC power in coastal areas has been assessed using ocean data products and numerical models. Ul Haque et al. (2017) estimated the power near the coast of Pakistan based on the vertical temperature difference from the World Ocean Atlas 2013 dataset. Wicaksono and Putri (2018) also estimated it west of Sulawesi Island using similar oceanographic datasets. Van Zwieten et al. (2017) assessed the resources off the coast of Florida by analyzing the results of the HYCOM model with a horizontal resolution of 1/25° to identify appropriate sites for the construction of OTEC plants. However, these studies assessed the OTEC power using the temperature difference between the warm surface and cold deep waters with a fixed intake rate. Apparently, the environmental limit of the deep water motion should be taken into account for the heat transport calculation.

The M_2 internal tides are generated effectively around the Ryukyu Island chain due to its topographic features, and the strong mixing results from the local dissipation of the tidal energy (Fig. 12 in Niwa and Hibiya 2004). In this process, the energy cascade to dissipation scale is controlled by parametric subharmonic instability for low latitude ocean regions (Hibiya et al. 2002). Therefore, tidal mixing may play a key role around the Okinawa Trough. This mixing leads to large vertical diffusivities, which are 3 to 4 order-of-magnitude greater than the typical values in the open ocean, and the corresponding residence time is only 5 to 10 years there (Nishina et al. 2016). This study focuses on the ocean thermal energy potential in the Aguni Basin, which lies near the eastern boundary of the Okinawa Trough (Fig. 3-2a). We guess the tidal mixing and associated upwelling in deep layers are also strong in the Aguni Basin, as the Okinawa Trough, and the global timescale of thermohaline circulation (~ 1000 years) may not be directly applicable for coastal and marginal seas, such as the Aguni Basin, where local processes are dominant.

Therefore, we attempt to simulate the temperature and velocity fields and estimate the ocean thermal energy potential in the Aguni Basin. This study also aims to improve coastal ocean thermal energy potential estimation using various approaches based on the results of a high-resolution ocean

model. This model is introduced and validated in Section 3.2. The deep layer thermal equilibrium of the basin is analyzed in Section 3.3. The methods for estimating the ocean thermal energy potential and their results are shown in Section 3.4. The discussion and conclusions are presented in Section 3.5.

3.2 Model

3.2.1 Model configurations

The temperature and velocity fields used in this study are simulated using a high-resolution ocean model (named as DR_Ek). It is a 3-D, hydrostatic, z-coordinate, primitive equation model based on the RIAM Ocean Model (Lee et al. 2003). It is a B-grid model with free surface in spherical coordinates. The Boussinesq approximation and mode-splitting are adopted. The Smagorinsky scheme (Smagorinsky 1963) is used for calculating the horizontal eddy viscosity and diffusion coefficients (Prandtl number = 2.0, which is the ratio of viscosity to diffusivity), while the scheme developed by Noh and Kim (1999) is used for calculating the vertical eddy viscosity and diffusion coefficients (Prandtl number = 0.8333). The quadratic bottom friction and partial step topography are adopted at bottom layer.

As shown in Fig. 3-2a, the model covers the region 125°–128.4°E and 25°–28.4°N, west of Okinawa Island, with a horizontal resolution of 1/12° times 1/15°, corresponding to about 1.5 km resolution. It has 40 depth levels in the vertical direction. The layer thickness increases gradually from surface (2 m at 1 m depth) to bottom (960 m at 5674 m depth). The open boundary conditions are provided by the DR_M model (Hirose et al. 2013), which covers the East Asian marginal seas. The meteorological forcing data are from the Meso-Scale Model (MSM) provided by Japan Meteorological Agency. The main parameters are listed in Table 3-1. Other parameters used in this

39

model are basically the same as those in the model developed for the estimation of Kuroshio current power (Liu et al. 2018).

The experiment (named as CR) is carried out from January 2014 to December 2018. The results for the last 4 years are used for the estimation. The initial and open boundary conditions are based on the results of DR_M model, whose time-mean value is calibrated with an assimilation dataset, Four-dimensional Variational Ocean Reanalysis for the Western North Pacific over 30 years (FORA-WNP30) (Usui et al. 2017). The domain of this model covers the path of the Kuroshio current in the East China Sea (ECS). The current speed can exceed 50 cm/s at 400 m depth, which is illustrated in the northwestern region shown in Fig. 3-3. Additionally, the model is able to resolve the strong and complex tidal motions near the coast, which can be found by comparing the eastern parts. To clarify the tidal effect, a simulation without tide (named as NT) is conducted over the same period as CR. In this experiment, the open boundary forcing data are smoothed using 25-hour running means to eliminate tidal signals.

The circulation in and around the Aguni Basin is well represented because of large model domain and high horizontal resolution. However, the vertical resolution should be improved in future study, especially around the sill depth of the channels connecting the Aguni Basin with the Okinawa Trough (Fig. 3-2b).

3.2.2 Model validation

The simulated potential temperature and salinity are compared with the Expendable Conductivity-Temperature-Depth Profiler (XCTD) measurements shown in Figs. 3-4 and 3-5. These observations were conducted on October 22, 2014, January 24, 2015, April 19, 2015 and July 4, 2015. The location is near the OTEC plant on Kumejima Island, as shown in Fig. 3-2b. The model represents seasonal variations of temperature well in the upper mixed layer, while the simulation

results for temperature and salinity in deep layers are slightly greater than the observations. The intermediate water in the Okinawa Trough is mainly composed of North Pacific Intermediate Water (NPIW) and South China Sea Intermediate Water (SCSIW) (Nakamura et al. 2013), which is illustrated by the low salinity water between 600 m and 800 m depths shown in Fig. 3-5. This result indicates that the intrusion of cold deep water into the Aguni Basin is well represented by the model. Thus, the DR_Ek model can be used for the estimation of ocean thermal energy potential in the Aguni Basin.

3.3 Deep layer thermal equilibrium

The intrusion of NPIW and SCSIW through two channels connecting the Aguni Basin with the Okinawa Trough cools the water in the basin (Fig. 3-2b). The average eastward velocity component through these channels and upward velocity component at 1006 m depth around the Aguni Basin for CR are shown in Fig. 3-6. Cold water originating from the Okinawa Trough intrudes into the basin through these channels in deep layers (Fig. 3-6a,b). Then the cold water is transported upward through upwelling (Fig. 3-6c). To clarify the tidal effect, the results for NT are also shown in Fig. 3-7. Comparison of Figs. 3-6 and 3-7 illustrates that the cold deep water intrusion and upwelling are weakened markedly without tide.

The cold deep water intrusion cools the water in the Aguni Basin. So the direction of heat flux is inverse to the volume transport in deep layers. To maintain constant temperature, it must be balanced quantitatively with other processes that heat the water in deep layers. To validate this hypothesis, the thermal equilibrium is analyzed. The thermodynamic equation below 1006 m depth over the Aguni Basin can be expressed as:

$$\left\{\rho c_{\mathrm{p}}\iiint_{\mathrm{bottom}}^{1006m}\overline{\frac{\partial T}{\partial t}}\,\mathrm{d}x\,\mathrm{d}y\,\mathrm{d}z\right\}_{\mathrm{L}}=\left\{-\rho c_{\mathrm{p}}\oiint_{\mathrm{bottom}}^{1006m}\overline{T}\,\overline{u}\,\mathrm{d}y\,\mathrm{d}z+\overline{T}\,\overline{v}\,\mathrm{d}x\,\mathrm{d}z+\overline{T}\,\overline{w}\,\mathrm{d}x\,\mathrm{d}y\right\}_{\mathrm{MP}}$$

$$+\left\{-\rho c_{\mathrm{p}}\oiint_{\mathrm{bottom}}^{1006m}[\overline{T'u'}\,\mathrm{d}y\,\mathrm{d}z+\overline{T'v'}\,\mathrm{d}x\,\mathrm{d}z]_{\mathrm{HPP}}+[\overline{T'w'}\,\mathrm{d}x\,\mathrm{d}y]_{\mathrm{VPP}}\right\}_{\mathrm{PP}} \qquad (3\text{-}1)$$

$$+\left\{\rho c_{\mathrm{p}}\oiint_{\mathrm{bottom}}^{1006m}[\overline{K_{\mathrm{h}}\frac{\partial T}{\partial x}}\,\mathrm{d}y\,\mathrm{d}z+\overline{K_{\mathrm{h}}\frac{\partial T}{\partial y}}\,\mathrm{d}x\,\mathrm{d}z]_{\mathrm{HBD}}+[\overline{K_{\mathrm{v}}\frac{\partial T}{\partial z}}\,\mathrm{d}x\,\mathrm{d}y]_{\mathrm{VBD}}\right\}_{\mathrm{BD}}$$

where ρ and c_{p} are average seawater density (= 1025 kg/m^3) and seawater specific heat (= 4000 J/kg K), respectively. The influence of hot spots has been omitted in Eq. 3-1. This equation is similar to Eq. 4 in Nagai and Hibiya (2013). The terms L, MP, PP and BD are the local time variation of internal energy, and the heat transported by mean product, perturbation product, and background diffusion, respectively. The symbols H and V before PP and BD indicate their horizontal and vertical components.

The average values of each term in Eq. 3-1 over the Aguni Basin for CR are shown in Fig. 3-8. The two largest terms are MP and VPP that nearly offset each other, while HBD and VBD are negligible. The negative MP suggests that the intrusion of cold deep water cools the water in the basin. This process is balanced by horizontal and vertical mixing mainly caused by tide, which is reflected in the values of HPP and VPP. Hence, we can assume that the value of PP or MP gives the environmental limit of the OTEC power to consume the cold water in deep layers. Two methods in the present study are based on this assumption (see Sections 3.4.3 and 3.4.4). The average values of each term in Eq. 3-1 for NT are also shown in Fig. 3-8. Comparison of the results for CR and NT indicates that the values of MP, HPP and VPP for NT are only 14.8%, 14.7% and 16.6% of those for CR, respectively.

The monthly horizontal volume transport into the basin (across the black line shown in Fig. 3-2b) below 1006 m depth is shown in Fig. 3-9. The average horizontal volume transport into the basin is 0.0447 Sv (1 Sv = 10^6 m^3/s) for CR, and its monthly average is always positive. The average transport for NT is 0.0086 Sv, which is only 19.3% of that for CR. These results indicate

that the thermal equilibrium of the basin cannot be maintained without tide. Therefore, the tidal simulation plays a key role in estimation of the ocean thermal energy potential in the Aguni Basin.

3.4 Results

3.4.1 Wick-Schmitt method

Wick and Schmitt (1977) proposed a simple method for estimating OTEC power density. The temperature difference between the warm surface and cold deep waters is assumed to be ΔT, and the average thickness of the upper mixed layer is assumed to be h. Both of them can be output directly by the DR_Ek model. Then, the thermal energy contained in the upper mixed layer per unit area can be expressed as:

$$E = \rho c_p h \Delta T \tag{3-2}$$

For simplicity, we assume that the OTEC plant has no effect on the temperature field in this study. Therefore, the ocean thermal energy potential can be calculated off-line based on the model results. The depth of the surface layer is set to 20 m, which is the depth of warm surface water intake pipe. Then, ΔT can be determined by:

$$\Delta T = T_{20m} - T \tag{3-3}$$

The OTEC power density is calculated as:

$$P = \frac{\rho c_p h \Delta T}{\Delta s} \tag{3-4}$$

where Δ*s* is the turnover time for deep ocean. Its value was set to 1000 years in Wick and Schmitt (1977). In this study, it is estimated as:

$$\Delta s = \frac{V_{\text{basin}}}{Q_{\text{in}} - Q_{\text{out}}}$$
(3-5)

The estimated turnover time of the Aguni Basin is 0.31 (1.61) years for CR (NT) using Eq. 3-5, while the residence time is 4.7–9.4 years over the southern Okinawa Trough as estimated by Nakamura et al. (2013). Thus, coastal areas may have much shorter turnover time than the global average.

3.4.2 Native Nihous method

The formula of the Nihous method, which is similar to Eq. 2 in Rajagopalan and Nihous (2013c), is as follows:

$$P = w_{\text{cw}} \frac{3 \rho c_{\text{p}} \varepsilon_{\text{tg}} \gamma}{16(1+\gamma)} \frac{(\Delta T)^2}{T_{20\text{m}}} - P_{\text{pump}}$$
(3-6)

$$P_{\text{pump}} = w_{\text{cw}} 0.30 \frac{\rho c_{\text{p}} \varepsilon_{\text{tg}} \gamma}{4(1+\gamma)}$$
(3-7)

The OTEC power density *P* depends on Δ*T* and the vertical velocity of cold deep water w_{cw}. As w_{cw} increases, the vertical mixing caused by the OTEC plant leads to the reduction of Δ*T*. As a result, *P* should reach a maximum, as shown in Fig. 3 in Rajagopalan and Nihous (2013c).

However, P is proportional to w_{cw} in this study, because the OTEC plant is assumed to have no effect on the temperature field. For simplicity, the efficiency factors are omitted in this study. Thus, the formula of the Nihous method can be simplified as:

$$P = w_{cw} \frac{3 \rho c_p \gamma}{8(1+\gamma)}$$
(3-8)

$$w_{cw} = \frac{Q_{in} - Q_{out}}{A_{basin}}$$
(3-9)

This method is referred to as the native Nihous method. In this study, w_{cw} equals to the average upwelling velocity at 1006 m depth.

3.4.3 Modified Wick-Schmitt method

A new method or modified version of the Wick-Schmitt method is introduced here. The formula is similar to that of the original Wick-Schmitt method, but the mixed layer thickness h is replaced with H, which is the thickness of water used for OTEC. Its value is set to 100 m. The formula of the modified Wick-Schmitt method is as follows:

$$P = \frac{\rho c_p H \Delta T}{\Delta s}$$
(3-10)

where Δs is estimated using Eq. 3-5, and ΔT is defined as the temperature difference between the upper and lower boundaries of water used for the OTEC plant, with thickness H. So ΔT can be estimated as:

$$\Delta T = H \frac{\mathrm{d}T}{\mathrm{d}z} \tag{3-11}$$

The vertical temperature gradient dT/dz is calculated from the model results. Then, the formula becomes:

$$P = \frac{\rho c_{\mathrm{p}} H^2 \dfrac{\mathrm{d}T}{\mathrm{d}z}}{\Delta s} \tag{3-12}$$

3.4.4 Perturbation method

The estimation of OTEC power using the Wick-Schmitt and Nihous methods depends on the temperature difference between the warm surface and cold deep waters. However, if the temperature in surface layers is assumed to be stable, the heat transport by PP can be considered as the environmental limit of the OTEC power. Then, the formula of this method, referred to as the perturbation method, can be expressed as:

$$P = \frac{-\rho c_{\mathrm{p}} H \oiint \left(\overline{T'u'} \, \mathrm{d}y\,\mathrm{d}z + \overline{T'v'} \, \mathrm{d}x\,\mathrm{d}z + \overline{T'w'} \, \mathrm{d}x\,\mathrm{d}y \right)}{\iiint \mathrm{d}x\,\mathrm{d}y\,\mathrm{d}z} \tag{3-13}$$

The heat transported by zonal, meridional and vertical PP can be expressed as $\rho c_{\mathrm{p}} T'u'$, $\rho c_{\mathrm{p}} T'v'$ and $\rho c_{\mathrm{p}} T'w'$, respectively. The prime symbol stands for the perturbation. The overline stands for time average from January 2015 to December 2018. The OTEC power density P at a certain depth is proportional to the closed surface integral of time averaged heat transported by the zonal, meridional and vertical components of PP.

46

3.4.5 Estimation of ocean thermal energy potential

Figure 3-10 shows the comparison of average OTEC power density of the Aguni Basin estimated using these methods. Because the value estimated using the native Nihous method is very close to that estimated by the original Wick-Schmitt method, the result of the former method is not shown in Fig. 3-10.

The thermal energy estimated using the original (modified) Wick-Schmitt method increases (decreases) with an increase in depth. The value estimated using the modified Wick-Schmitt method is much lower than that estimated by the original Wick-Schmitt method or the native Nihous method especially in deep layers. This difference arises because of the definition of temperature difference, ΔT. The modified Wick-Schmitt method applies the local temperature gradient rather than the difference between the warm surface and cold deep waters, so ΔT is much smaller than that of the original method. Actually the results of the original Wick-Schmitt method seem unrealistic since the average OTEC power density exceeds 350 W/m^2, which is even greater than the average solar irradiation on the surface of the Earth (342 W/m^2). By definition, the original Wick-Schmitt method represents the surface heat transport rather than the deep flow. The modified method should provide more realistic estimate of the deep transport that is critical to the entire thermal structure.

For the perturbation method, the area-mean values are consistent with those estimated by the modified Wick-Schmitt method in deep layers. So the turnover times of 0.31 and 1.61 years for CR and NT experiments are quantitatively appropriate for the estimation of deep thermal balance in the Aguni Basin. The strong fluctuations at middle layers shown in Fig. 3-10a can be ascribed to the explicit tidal motion because the fluctuations are much smaller in Fig. 3-10b. This fluctuation depends on the length of analysis period and thus we can expect smoother profile for infinitely

longer period of simulation. It is also noted here that the strong tidal mixing maintaining the deep OTEC power for CR is 5 times larger than that for NT.

The spatial distribution of OTEC power density can be studied using the perturbation method. The estimated OTEC power density distributions at 1006 m depth, and along the section for CR, are shown in Fig. 3-11. High value appears near the boundary of the basin. This method also reveals that the northeastern slope of Kumejima Island is a promising area for effective OTEC power generation because the OTEC power density can exceed 50 W/m^2 at 1006 m depth (Fig. 3-11a) and the distance to the coast of Kumejima Island is short (< 10 km). The estimated average OTEC power density from all methods (Fig. 3-10) is larger than the average deep heat flux in the global ocean, which is less than 10 W/m^2 below 1000 m depth (Cummins et al. 2016). The difference between Figs. 3-11 and 3-12 suggests that the neglect of tides results in the underestimation of OTEC power density. The estimated OTEC power density for NT is less than 20 W/m^2 at 1006 m depth near the northeastern slope of Kumejima Island, as shown in Fig. 3-12a. Therefore, the tidal simulation is crucial for estimating ocean thermal energy potential for coastal areas.

3.5 Discussion and conclusions

The ocean thermal energy potential of the Aguni Basin was estimated based on the results of a high-resolution ocean model. The environmental limit of the deep water motion was taken into account for the estimation. The estimated turnover time (< 1 year) for the Aguni Basin, based on Eq. 3-5, is much shorter than the global average (about 1000 years) owing to the cold deep water intrusion (e.g., Fig. 3-6). The Wick-Schmitt method (1977) and Nihous method (Adiputra et al. 2020; Nihous 2005, 2007a,b, 2018; Rajagopalan and Nihous 2013a,b,c; Jia et al. 2018; Van Zwieten et al. 2017) overestimated the ocean thermal energy potential with the realistic turnover time in the Aguni Basin (Fig. 3-10), which implies that methods and parameters used for global estimation may

not be applicable to the Aguni Basin. Therefore, the modified Wick-Schmitt and perturbation methods were proposed to improve the estimation. Both of the two methods adopted the temperature difference in deep layers rather than that between the warm surface and cold deep waters, although the turnover time was unchanged.

The estimated average OTEC power density in the Aguni Basin is larger than that in the global ocean. This difference is basically attributed to strong tidal mixing. The importance of tidal motion to the estimation of ocean thermal energy potential is demonstrated based on the results of an additional simulation without tide and analysis of deep layer thermal equilibrium in the Aguni Basin. Besides the deep layer thermal equilibrium (Fig. 3-8) and the cold deep water intrusion (Fig. 3-9), the tidal effects are also illustrated in Fig. 3-13, which compares the difference of heat transport between CR and NT. The vertical heat transport and the intrusion of cold deep water are markedly weakened in NT (Fig. 3-13b). This difference is attributed to the stronger $T'w'$ by tidal mixing, which transports more heat downward in CR.

The generation of strong upwelling near the boundary of the basin results from the strong mixing. The tides result in strong mixing owing to parametric subharmonic instability (Niwa and Hibiya 2004). In addition, the strong mixing is also favored by near-critical angles of the slope there. This is because that the reflection of internal wave can strengthen the internal wave mixing if the characteristic slope of internal waves is close to the bottom slope. This phenomenon was found by Schafstall et al. (2010) in the Mauritanian upwelling region. The characteristic angle α of internal wave can be calculated by Eq. 3-14, which derives from Eq. 2 in Schafstall et al. (2010).

$$\alpha = \tan^{-1} \sqrt{\frac{\sigma^2 - f^2}{N^2 - \sigma^2}} \qquad (3\text{-}14)$$

In Eq. 3-14, σ is the frequency of M_2 tide, f is the inertial frequency, and N is the buoyancy frequency. The topographic slope angle and M_2 internal wave characteristic angle are compared in

Fig. 3-14. The dashed line is the 1006 m depth contour. The characteristic angle of M_2 internal wave is nearly uniform in the basin and the dashed line is basically along the 1° contour, while the topographic slope angle varies significantly along the dashed line. The slope of the southeastern boundary at 1006 m is steeper than that of other areas, and its slope angle can exceed 8°. This area is consistent with the low OTEC power density in the southeastern part of the basin shown in Fig. 3-11a. The topographic slope angle is close to 1° around the western and northern boundaries, where the upwelling is vigorous (Fig. 3-6c) and the OTEC power density reaches large value (Fig. 3-11a).

The standard deviation of monthly OTEC power density in the basin estimated using the perturbation method is of the same magnitude as the mean value (results not shown). This finding suggests that the large negative and positive values shown in Fig. 3-11 may be due to the effect of M_2 internal tides, which are effectively generated around the Ryukyu Island chain and/or continental shelf in the ECS (Niwa and Hibiya 2004). Alford et al. (2015) found that the Kuroshio current can noticeably refract internal tides around the Luzon Strait, suggesting a strong influence of the Kuroshio current on the tidal signal. This study concludes that both of the available cold deep water transport and ocean thermal energy potential in the Aguni Basin are five orders larger than the present mechanical limit. Huge ocean thermal energy seems available in the Aguni Basin. The results have revealed that strong and sustainable power generation is possible near the northeastern slope of Kumejima Island within a short distance of the coast (Fig. 3-11).
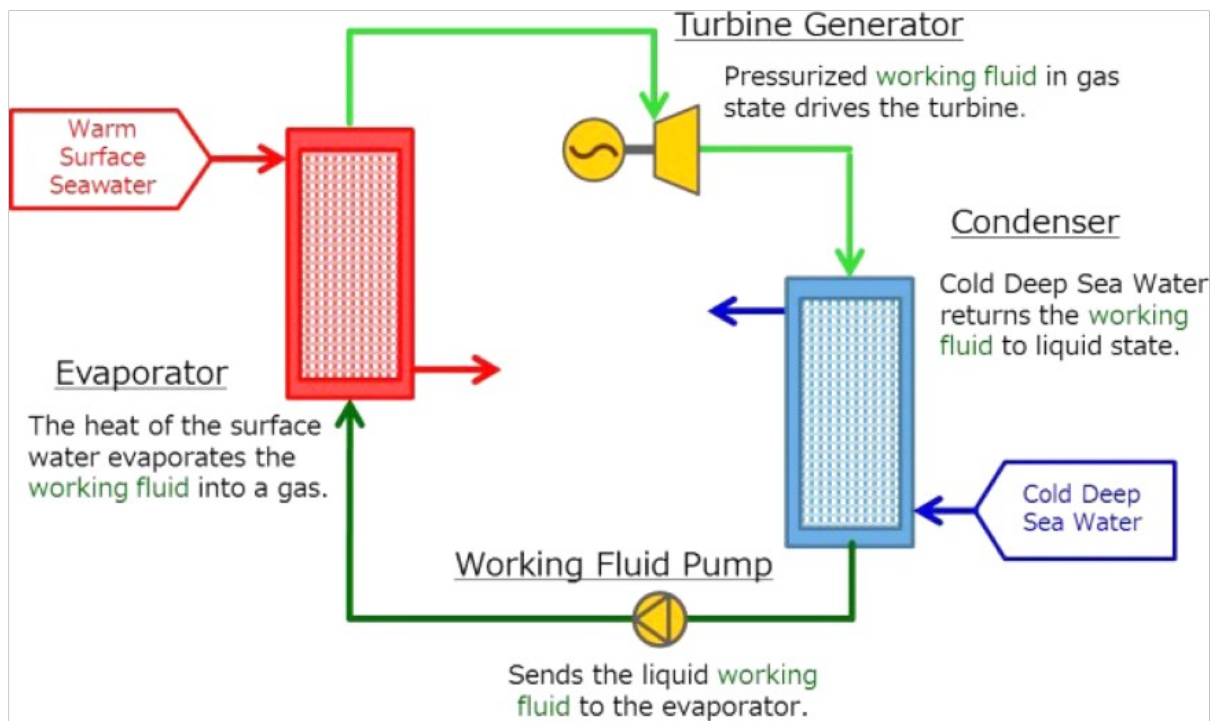
Fig. 3-1 Schematic diagram of the ocean thermal energy conversion (OTEC). Source:

http://otecokinawa.com/en/OTEC/OTECBasics.jpg
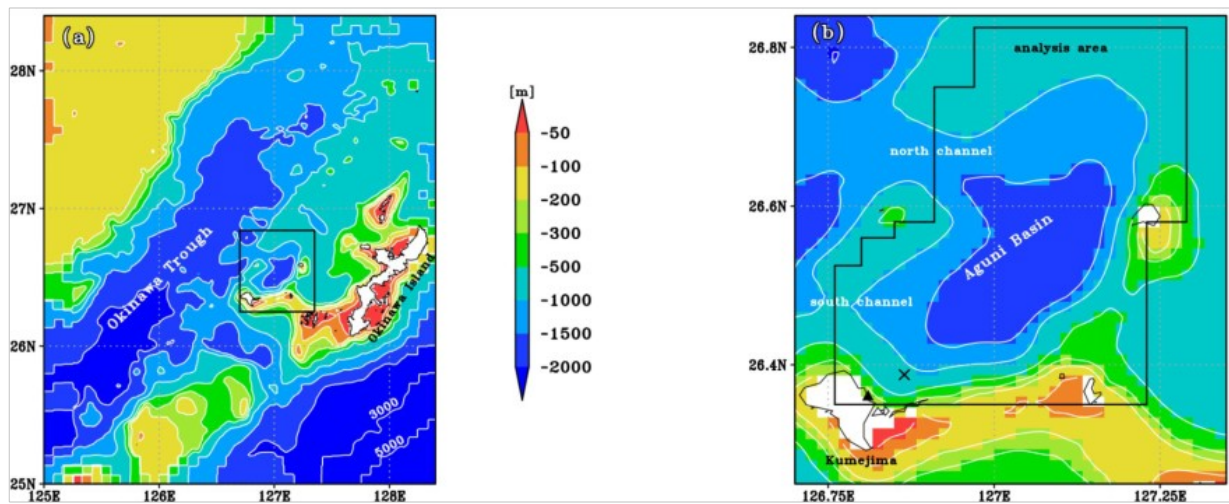
Fig. 3-2 Topography of the model domain (a). The box in (a) is enlarged as (b) to show the Aguni Basin. The black line in (b) outlines the analysis area. The triangle and cross marks show the locations of the Okinawa OTEC Demonstration Facility (126.81°E, 26.36°N) and the temperature and salinity measurements (126.86°E, 26.39°N)
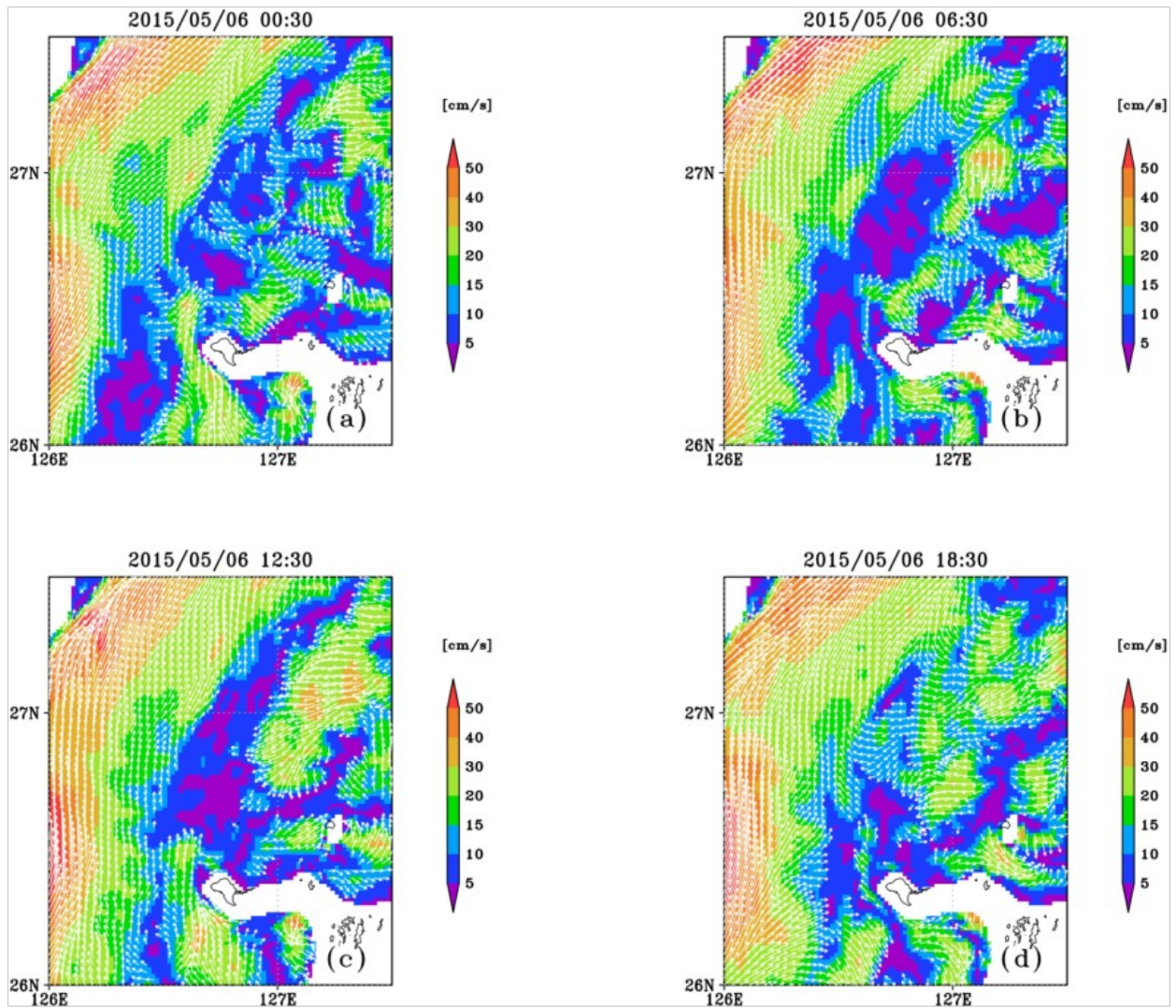
Fig. 3-3 Current vectors (cm/s) at 400 m depth based on the results of CR for 00:30 (a), 06:30 (b),

12:30 (c), and 18:30 (d) on May 6, 2015 (UTC). Vectors with speeds less than 10 cm/s are not

shown
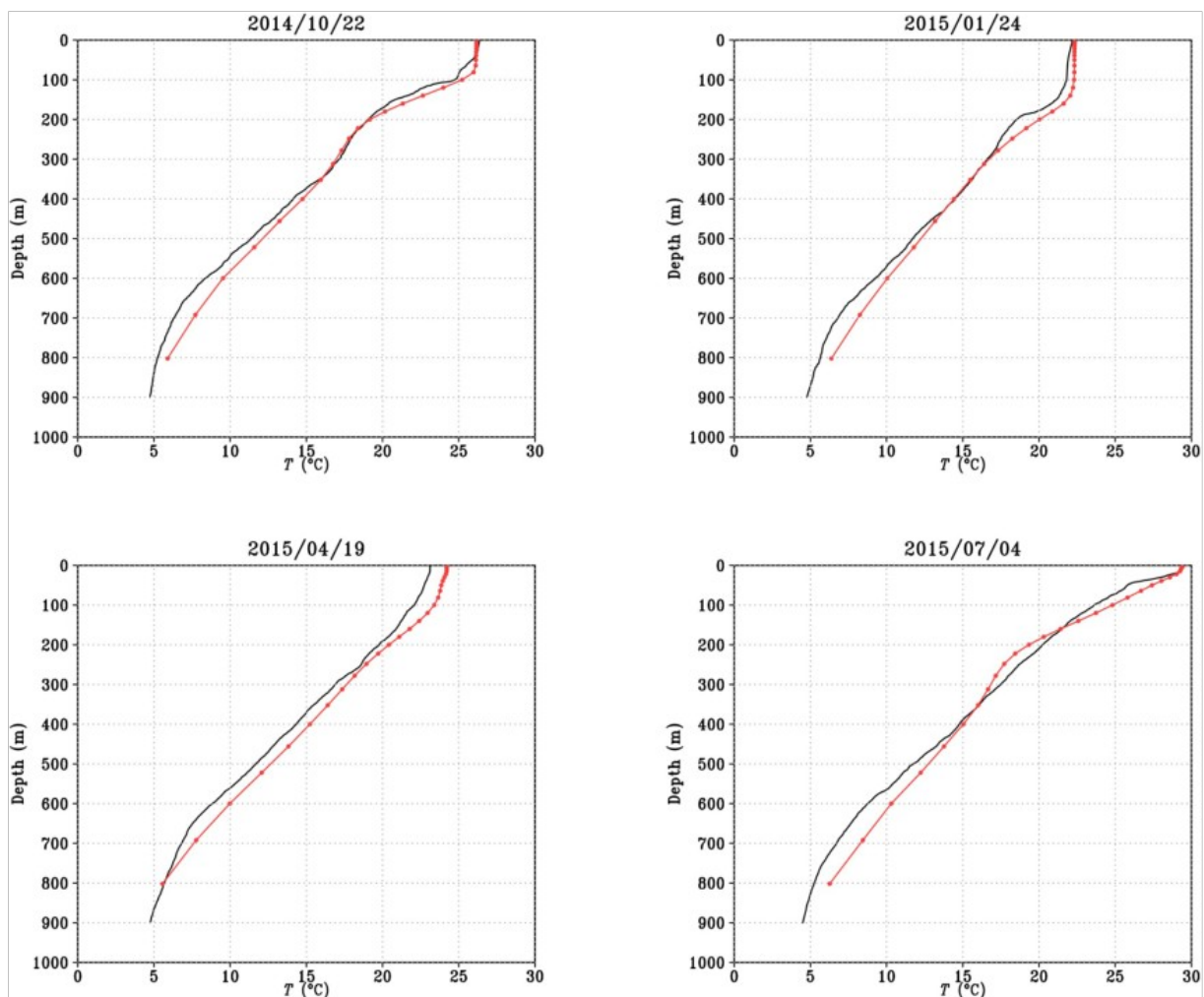
Fig. 3-4 Comparison of potential temperature (°C) observations and simulations at 126.86°E, 26.39°N (black: Expendable Conductivity-Temperature-Depth Profiler [XCTD] measurements; red: DR_Ek simulations)
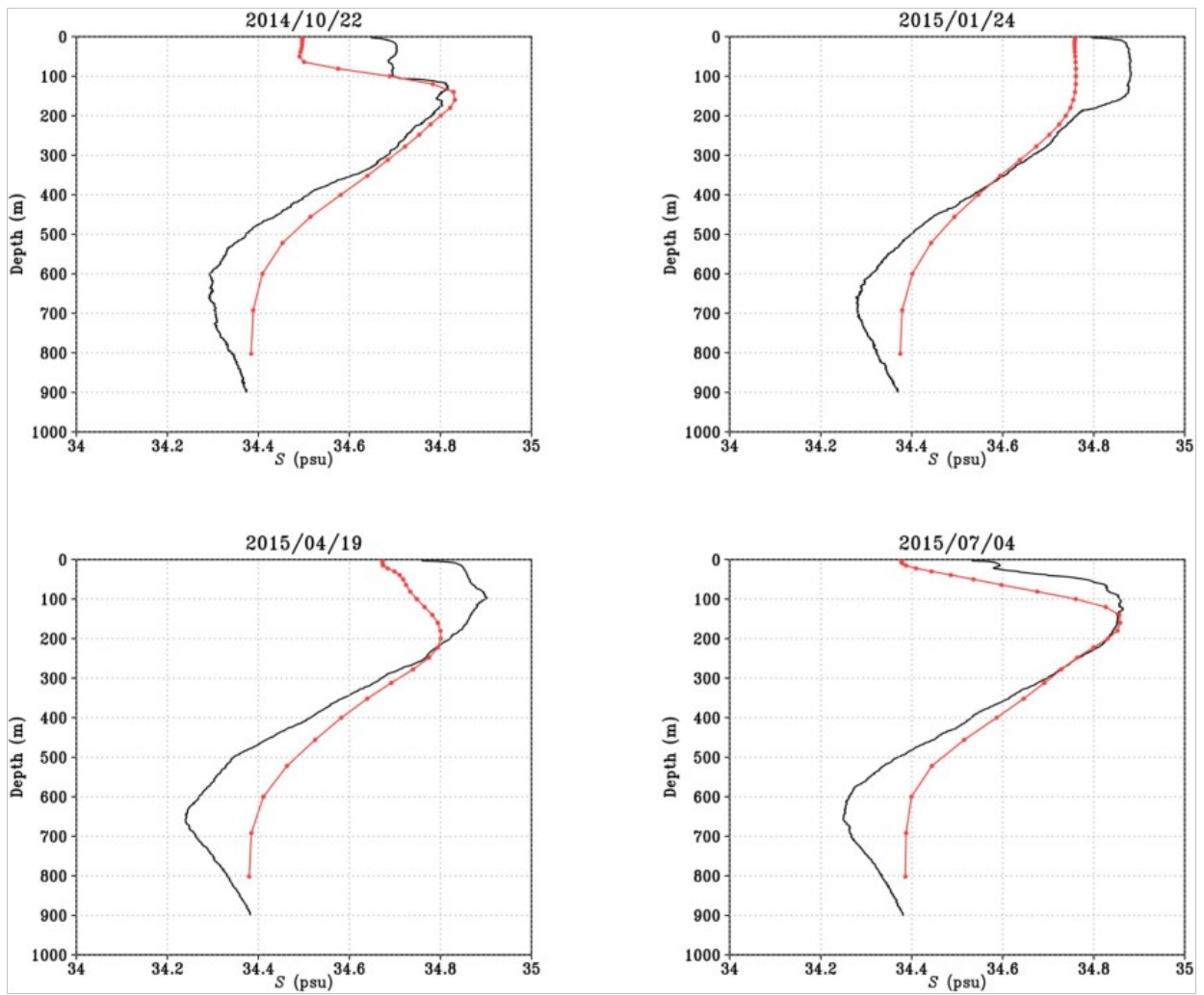
Fig. 3-5 Same as Fig. 3-4 but for salinity (psu)
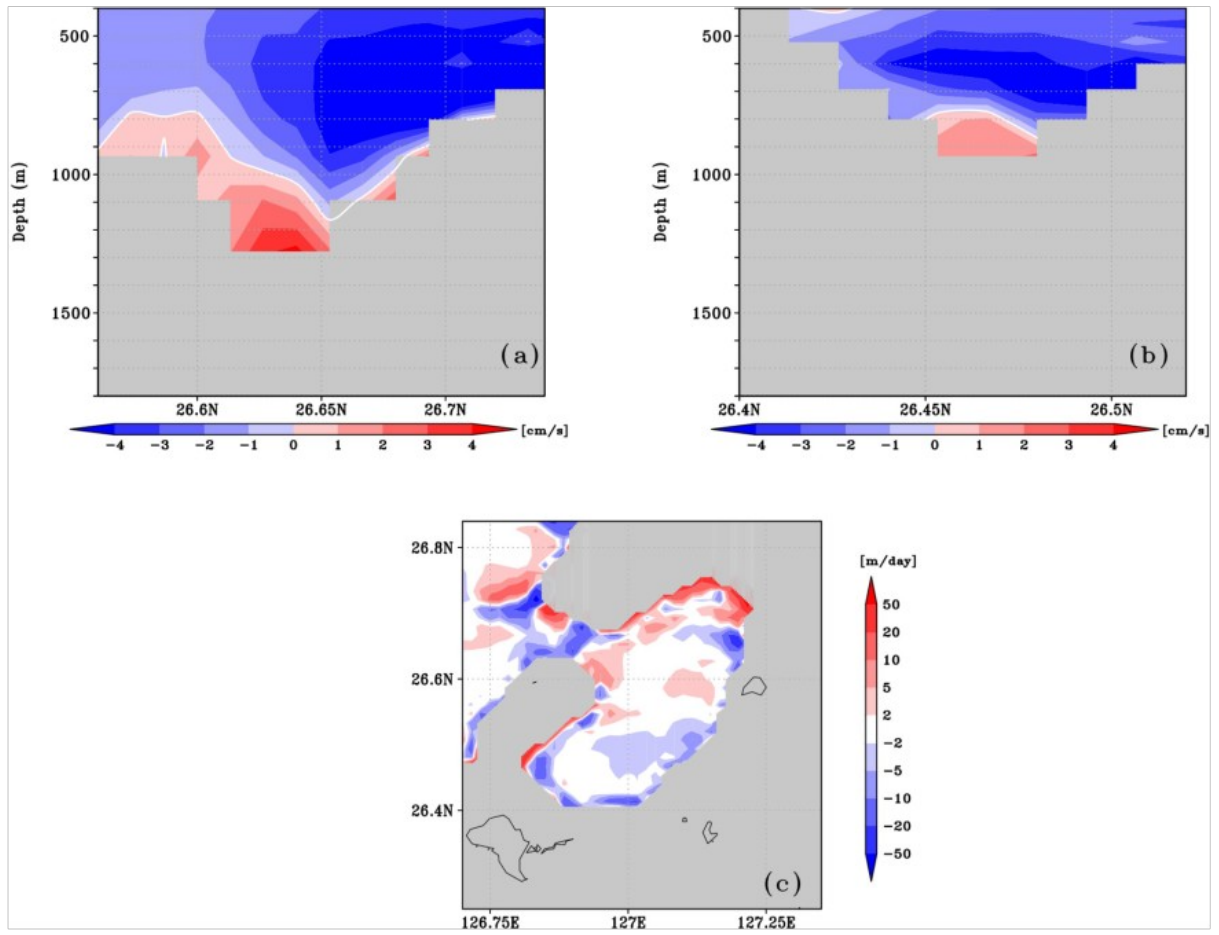
Fig. 3-6 Average eastward velocity component (cm/s) through the northern (a; 126.91°E section) and southern (b; 126.76°E section) channels, and upward velocity component (m/day) at 1006 m depth around the Aguni Basin (c) for CR. The value of the white contour in (a, b) is 0
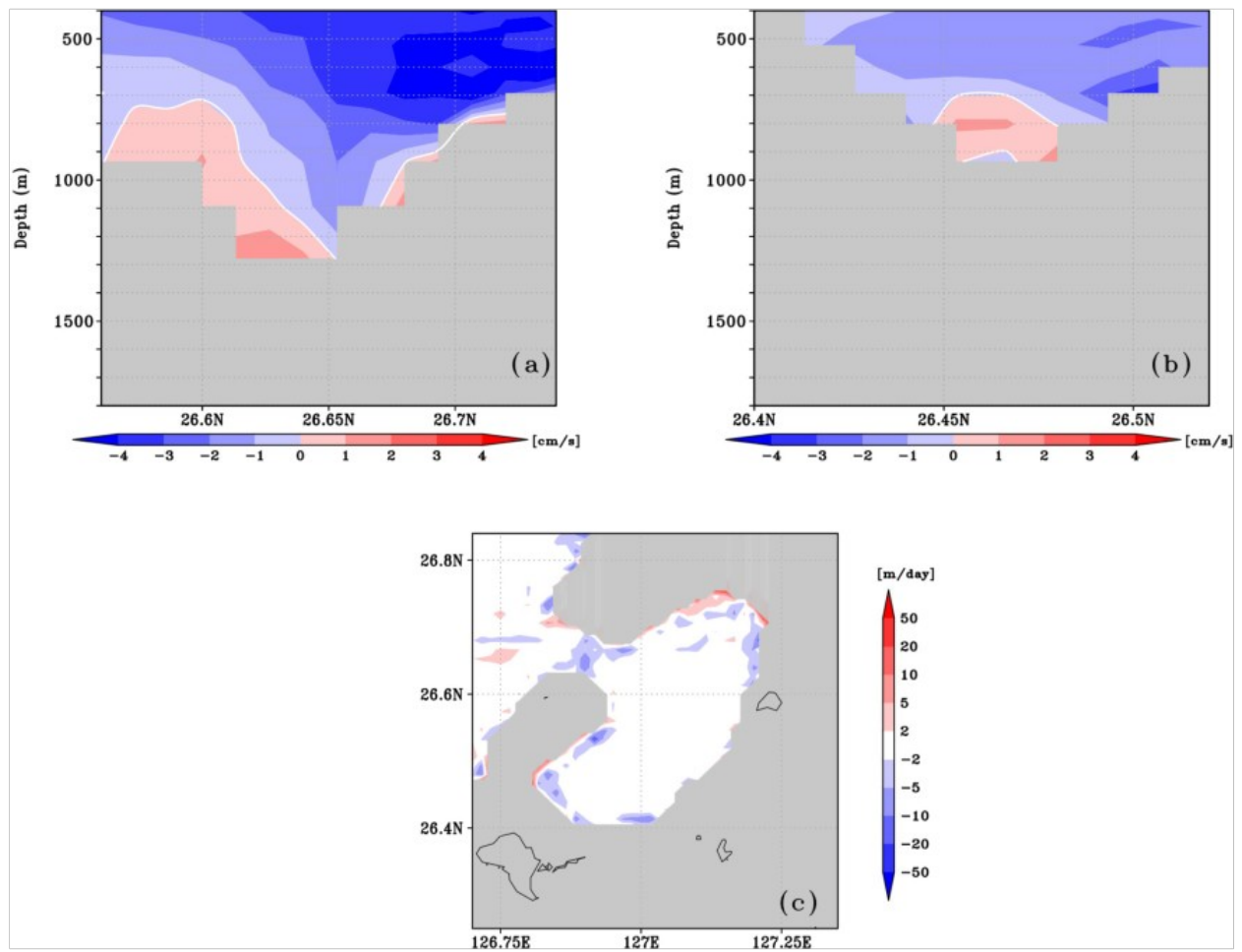
Fig. 3-7 Same as Fig. 3-6 but for NT
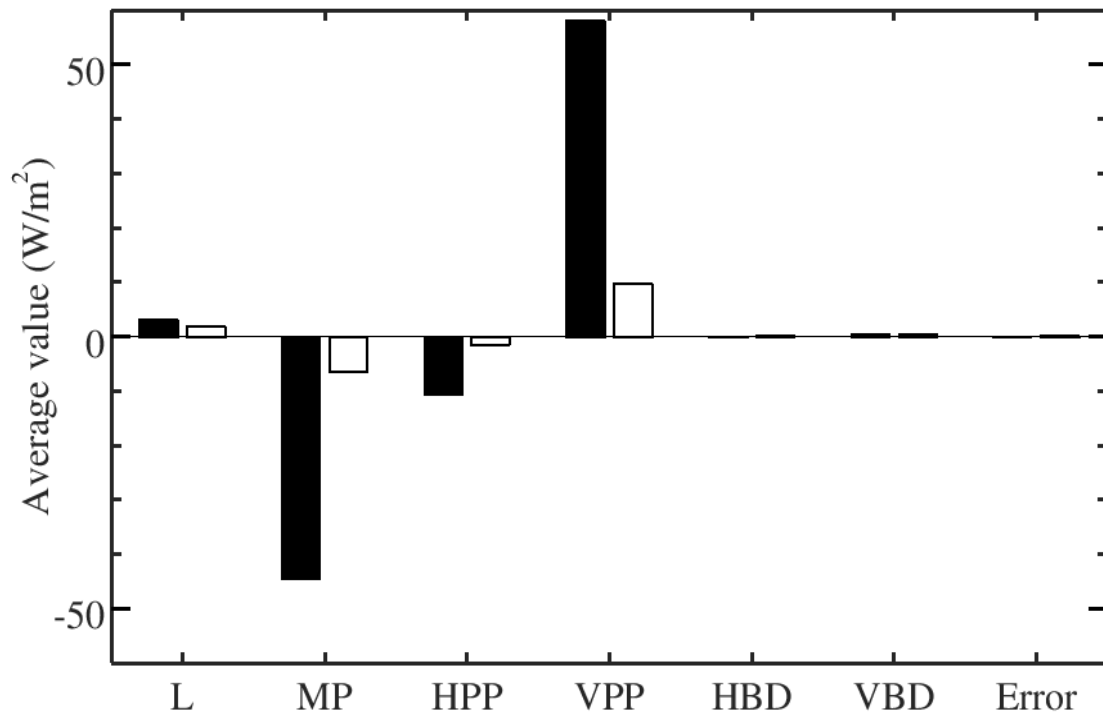
Fig. 3-8 Average values (W/m²) of each term in Eq. 3-1 for CR (filled) and NT (open) below 1006

m depth over the Aguni Basin
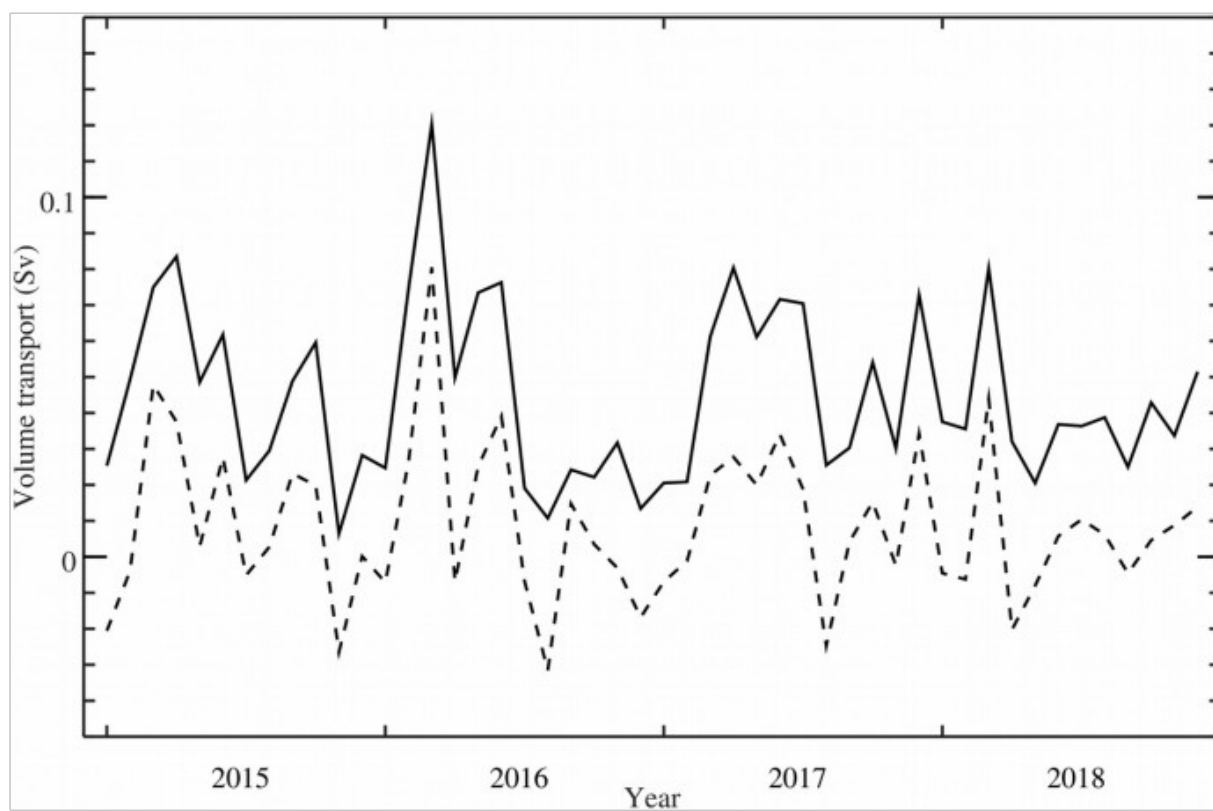
Fig. 3-9 Monthly horizontal volume transport into the Aguni Basin below 1006 m depth (solid line: CR; dashed line: NT)
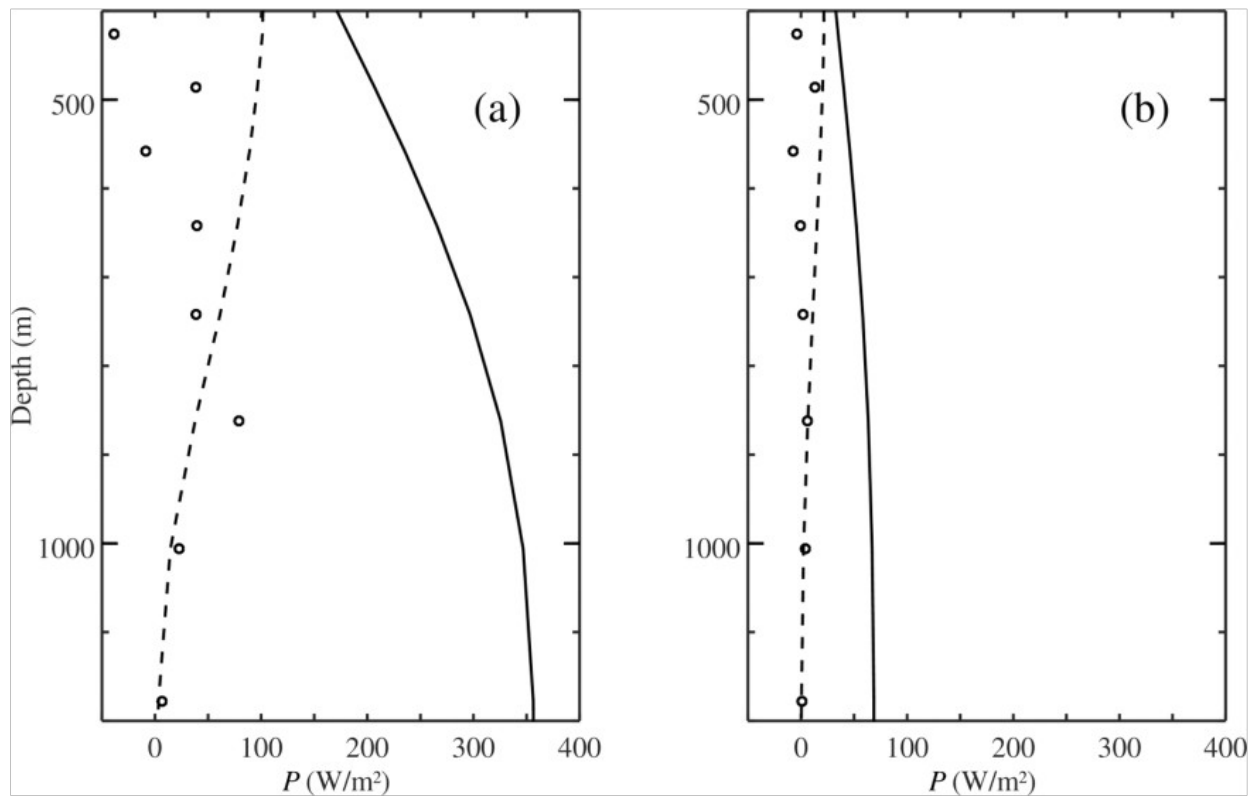
Fig. 3-10 The OTEC power density (W/m²) averaged over the Aguni Basin estimated using the Wick-Schmitt method (solid), modified Wick-Schmitt method (dashed), and perturbation method (circle) for CR (a) and NT (b)
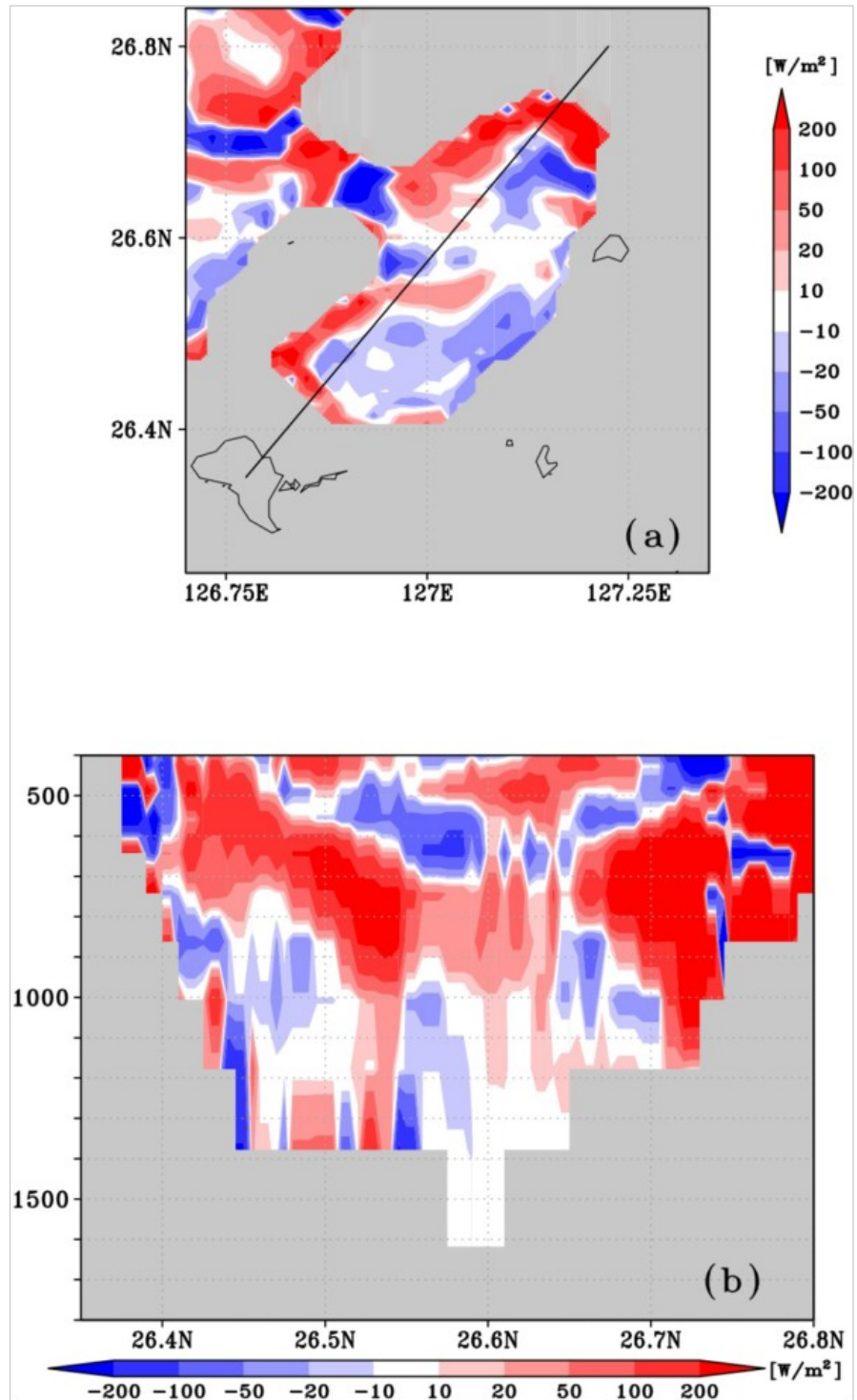
Fig. 3-11 Average OTEC power density (W/m^2) at 1006 m depth (a), and along the section (b)

estimated using the perturbation method for CR

61
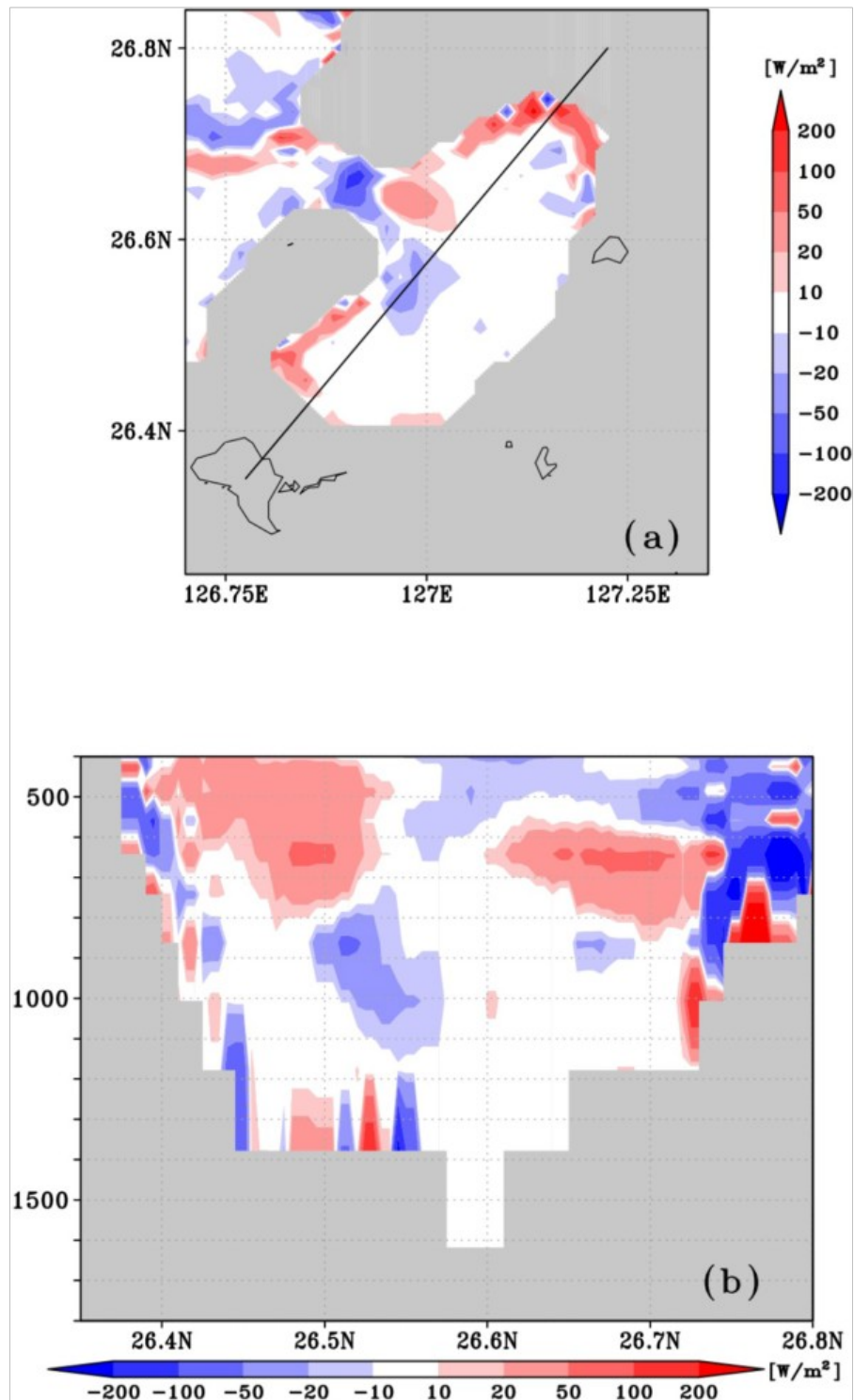
Fig. 3-12 Same as Fig. 3-11 but for NT
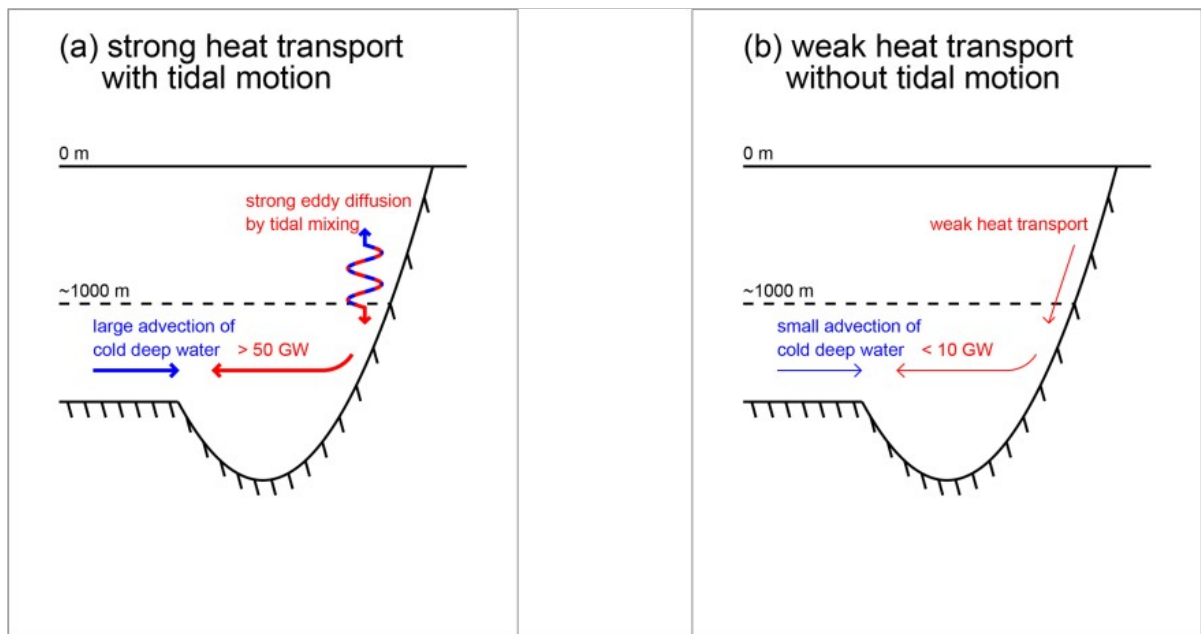
Fig. 3-13 Schematic illustration showing the tidal effect on the heat transport in the Aguni Basin by comparing the difference between CR (a) and NT (b)
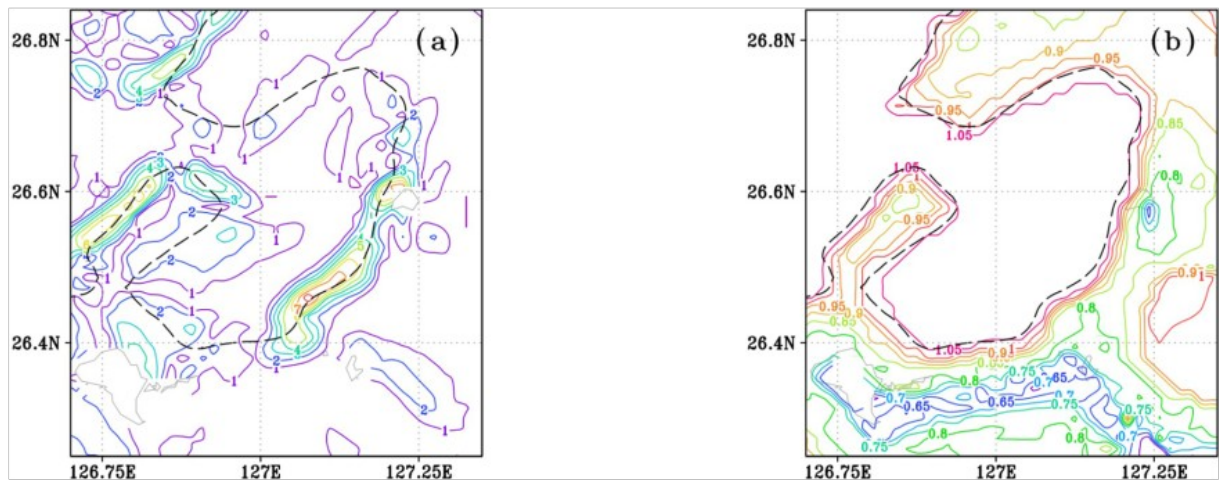
Fig. 3-14 Topographic slope angle (a) and M_2 internal wave characteristic angle (b). The unit is

degree. The dashed line shows the 1006 m depth contour

Table 3-1 Main parameters of the DR_Ek model

Parameters	Values
Number of zonal grids	205
Zonal resolution	1/60°
Number of meridional grids	265
Meridional resolution	1/75°
Number of vertical levels	40
Smagorinsky constant	0.17
Bottom drag coefficient	0.0027

Chapter 4. Comparison of surface and lateral boundary conditions controlled by pseudo-altimeter data assimilation for a regional Kuroshio model

4.1 Introduction

High-resolution ocean forecast is beneficial to fishery, ocean power, navigation safety, and so on. For swift and accurate predictions in particular areas, a high-resolution regional ocean model simulation with lateral boundary conditions provided by lower resolution parent model is reasonable. To reduce system error (i.e., process noise) and improve simulations, satellite altimeter data were commonly assimilated into regional ocean models in the literature (e.g., Wu et al. 1999; Hirose et al. 2005).

Regardless of linear or nonlinear capabilities, the effect of data assimilation to ocean models relies much on the determination of the process noise, which has been often given by empirical or simplified procedures. Understanding the ocean circulations as a decaying system, one rational approximation may be the form of surface meteorological forcings for the additive system noise (e.g., Fukumori et al. 1993; Hirose et al. 1999, 2005).

In addition, accurate lateral boundary conditions were proved to be critical to regional ocean models. For example, lateral boundary conditions were able to control the circulation of a coastal ocean model (Koenig et al. 2020). The influence of lateral boundary condition errors was reduced when the measurements close to the inflow boundary were assimilated by an extended Kalman filter with a nonlinear multilayer quasi-geostrophic ocean model (Evensen 1993). The impacts of surface meteorological condition are expected to decay rapidly to depths and may not propagate into deep layers. In this study, we therefore attempt to use lateral boundary condition data assimilation to improve the representation of the Kuroshio current southwest of Japan.

Satellite altimeter data were assimilated into the regional ocean models around Japan archipelago in previous studies using various methods. Empirical data assimilation such as nudging method has been adopted in the satellite altimeter data assimilation over the Kuroshio current and its extension (e.g., Kamachi et al. 2004; Nishihama and Ikeda 2007). Alternatively, optimal schemes such as Kalman filter and variational methods have also been used later (e.g., Miyazawa et al. 2012; Usui et al. 2015). The ensemble Kalman filter proposed by Evensen (1994) is an effective data assimilation method for nonlinear models with huge degrees of freedom. However, this method still requires large computational cost for high-resolution regional ocean model simulations. Thus, an approximate Kalman filter based on Fukumori and Malanotte-Rizzoli (1995) is used as the data assimilation method in this study.

Twin experiment was broadly used to evaluate the data assimilation. In a twin experiment, the results of one simulation are regarded as the "true" state, and another simulation assimilates the pseudo-observations of the "true" state. Then the applied assimilation can be evaluated by comparing these results. To create the pseudo-observations, the "true" state is subsampled following the spatial and temporal positions of real observations such as satellite altimeter data (e.g., Fukumori et al. 1993; Korres et al. 2007) and oceanic data (e.g., Fukumori and Malanotte-Rizzoli 1995; Broquet et al. 2011). This paper will study and compare surface and lateral boundary forcings based on twin experiments. The pseudo-observations are generated along the tracks of satellite altimeter data southwest of Japan.

This paper is organized as follows. The model and data are introduced in Section 4.2. The approximate Kalman filter used in this study is described in Section 4.3. The results of experiments are shown in Section 4.4. Last, the summary and discussion are presented in Section 4.5.

4.2 Model and data

4.2.1 Regional ocean model

The present data assimilation research of the East Asia marine system used in this study is named as DR_Ep. It is based on the Research Institute for Applied Mechanics Ocean Model (RIAMOM) originally developed by Lee et al. (2003). The model is a 3-dimensional primitive equation ocean model formulated in spherical coordinates with Arakawa B-grid and z-coordinate. Hydrostatic balance and Boussinesq approximation are adopted. Its horizontal resolution is $1/60° \times 1/75°$ corresponding to about 1.5 km, and it has 114 levels in the vertical direction. The model domain is a rectangle region of 126–132.65°E and 26–33.24°N southwest of Japan (Fig. 4-1). It covers part of the shallow East China Sea shelf and deep Okinawa Trough southwest of Japan. The topography is derived from JTOPO30 dataset provided by the Marine Information Research Center of the Japan Hydrographic Association (http://www.mirc.jha.jp).

The lateral boundary conditions of DR_Ep model are specified from the hourly results of its parent model, DR_M (Hirose et al. 2013). The one-way nesting is applied to the forward modeling in this study. The hourly meteorological forcing data are derived from the Meso-Scale Model provided by Japan Meteorological Agency. The Smagorinsky scheme (Smagorinsky 1963) is used to calculate the horizontal viscosity and diffusion coefficients, while the scheme developed by Noh and Kim (1999) is used to calculate the vertical viscosity and diffusion coefficients. At the bottom layer, quadratic bottom friction and partial step topography are adopted. The Smagorinsky constant is 0.17, and the bottom drag coefficient is 0.001. Similar models but over different domains have been applied in estimating the Kuroshio current power south of Japan (Liu et al. 2018) and ocean thermal energy potential around the Aguni Basin (Liu et al. 2020).

4.2.2 Satellite altimeter data

As quasi-routine ocean observations for mesoscale and large scale (De Mey 1997), satellite altimeter observations are fit for operational data assimilation, so we adopt the satellite altimeter data in this study. The main characteristics of four altimeter missions involved here are shown in Tab. 4-1. They are obtained from the AVISO website (https://aviso.altimetry.fr). Previous studies indicate that assimilating multi-satellite observations can acquire better assimilation effect than assimilating one single satellite (Smedstad and Fox 1994; Blayo et al. 1997). The sea level anomaly (SLA) data of multi-satellite altimeter observations from 1 January 2014 to 31 December 2014 are used here, and their positions are shown in Fig. 4-2.

4.3 Approximate Kalman filter

The model state vector $\mathbf{x}$ contains the temperature, salinity, zonal and meridional velocities, and sea surface height in the model grid. Given the huge degrees of freedom of the DR_Ep model, an approximate Kalman filter based on Fukumori and Malanotte-Rizzoli (1995) is adopted to reduce the computational cost. Then $\mathbf{x}$ can be expressed as follows:

$$\mathbf{x} = \mathbf{B}\,\mathbf{x}' \tag{4-1}$$

where $\mathbf{B}$ is a transformation matrix from coarse grid to fine grid, the prime symbol stands for reduced-order, and thus $\mathbf{x}'$ is the reduced-order state vector which contains the variables of $\mathbf{x}$ defined on the coarse grid in Fig. 4-3. The reference state of sea surface height is used to calculate SLA during the data assimilation. The transformation matrix $\mathbf{B}$ can be further divided into its horizontal part $\mathbf{B}_h$ and vertical part $\mathbf{B}_v$ (Eq. 4-2).

$$\mathbf{B} = \mathbf{B}_v \mathbf{B}_h \tag{4-2}$$

The mapping method from coarse grid to fine grid is the objective interpolation (Bretherton et al. 1976) with a decorrelation length of 25 grid points in the horizontal direction and 10-level decorrelation scale in the vertical direction.

The model is also linearized to reduce the computational cost when error covariance matrix $\mathbf{P}'$ is updated from original time step t-1 to new time step t using Lyapunove equation shown as follows:

$$\mathbf{P}'^{f}_{t}=\mathbf{A}'\mathbf{P}'^{a}_{t-1}\mathbf{A}'^{T}+\mathbf{\Gamma}'\mathbf{Q}'\mathbf{\Gamma}'^{T} \tag{4-3}$$

where the superscripts "a" and "f" stand for analysis and forecast. $\mathbf{A}'$ is the linearized model operator, which is invariant in time for this study, and thus, the subscript "t" is omitted. $\mathbf{\Gamma}'\mathbf{Q}'\mathbf{\Gamma}'^{T}$ is the process noise matrix which stands for uncertain elements in the model, the noises in surface and lateral boundary conditions. The corresponding linearized model can be expressed as follows:

$$\mathbf{x}'^{f}_{t}=\mathbf{A}'\mathbf{x}'^{a}_{t-1}+\mathbf{G}'\mathbf{w}'_{t-1}+\mathbf{\Gamma}'\mathbf{q}'_{t-1} \tag{4-4}$$

where $\mathbf{G}'$ is the time-invariant forcing operator, $\mathbf{w}'$ stands for the surface meteorological or lateral boundary forcing in this study, and $\mathbf{q}'$ is the process noise. In this study, $\mathbf{\Gamma}'$ is assumed to equal to $\mathbf{G}'$.

The model linearization can be expressed as follows:

$$\mathbf{A}'=\frac{\mathcal{F}\left(\mathbf{x}'+\delta\mathbf{x}',\mathbf{w}'\right)-\mathcal{F}\left(\mathbf{x}',\mathbf{w}'\right)}{\delta\mathbf{x}'} \tag{4-5}$$

70

where $\mathcal{F}$ is the DR_Ep model operator which means 1-day simulation on 1 December 2015, and $\delta\mathbf{x}'$ represents the amount of perturbation in reduced-order vector $\mathbf{x}'$. The perturbation $\delta\mathbf{x}'$ is 0.1°C for temperature, 0.1 psu for salinity, 1 cm/s for horizontal velocities, and 1 cm for sea surface height.

Based on these simplifications, Kalman gain $\mathbf{K}$ can be calculated by the equations as follows:

$$\mathbf{B}_{\mathrm{v}}\mathbf{B}_{\mathrm{h}}\mathbf{P}_t'^{\mathrm{a}}=\left[\mathbf{I}-\mathbf{B}_{\mathrm{v}}\mathbf{B}_{\mathrm{h}}\mathbf{P}_t'^{\mathrm{f}}\mathbf{B}_{\mathrm{h}}^{\mathrm{T}}\mathbf{B}_{\mathrm{v}}^{\mathrm{T}}\mathbf{H}_t^{\mathrm{T}}\left(\mathbf{R}+\mathbf{H}_t\mathbf{B}_{\mathrm{v}}\mathbf{B}_{\mathrm{h}}\mathbf{P}_t'^{\mathrm{f}}\mathbf{B}_{\mathrm{h}}^{\mathrm{T}}\mathbf{B}_{\mathrm{v}}^{\mathrm{T}}\mathbf{H}_t^{\mathrm{T}}\right)^{-1}\mathbf{H}_t\right]\mathbf{B}_{\mathrm{v}}\mathbf{B}_{\mathrm{h}}\mathbf{P}_t'^{\mathrm{f}} \qquad (4\text{-}6)$$

$$\mathbf{K}_t=\mathbf{B}_{\mathrm{v}}\mathbf{B}_{\mathrm{h}}\mathbf{P}_t'^{\mathrm{a}}\mathbf{B}_{\mathrm{h}}^{\mathrm{T}}\mathbf{B}_{\mathrm{v}}^{\mathrm{T}}\mathbf{H}_t^{\mathrm{T}}\mathbf{R}^{-1} \qquad (4\text{-}7)$$

where $\mathbf{I}$ is the identity matrix, $\mathbf{H}$ is the observation projector matrix, and $\mathbf{R}$ is the observation error covariance matrix.

In addition, the analysis value of model state vector $\mathbf{x}$ is updated through adding an increment term as follows:

$$\mathbf{x}_t'^{\mathrm{a}}=\mathbf{x}_t'^{\mathrm{f}}+\mathbf{K}_t\left(\mathbf{y}_t-\mathbf{H}_t\mathbf{x}_t'^{\mathrm{f}}\right) \qquad (4\text{-}8)$$

where $\mathbf{y}$ is the pseudo-observations of SLA from the reference solution (named as RS), which is the simulation without data assimilation from 1 January 2015. The lateral boundary condition $\mathbf{x}_{\mathrm{l}}$ from the parent model DR_M is also updated through adding an increment term $\mathbf{b}$, which is similar to Friedland (1969). This increment term is daily multiplied by a factor β to make the lateral boundary condition modification damp as time evolves (Eqs. 4-9 and 4-10).

$$\mathbf{b}_t'^{\mathrm{f}}=\beta\mathbf{b}_{t-1}'^{\mathrm{a}}+\mathbf{\Gamma}_{\mathrm{b}}'\mathbf{q}_{t-1}' \qquad (4\text{-}9)$$

$$\mathbf{b}_t'^{\mathrm{a}}=\mathbf{b}_t'^{\mathrm{f}}+\mathbf{K}_{1,t}\left(\mathbf{y}_t-\mathbf{H}_t\mathbf{x}_t'^{\mathrm{f}}\right) \qquad (4\text{-}10)$$

The factor β is set to 13/14 corresponding to an *e*-folding time scale of about 14 d (because β^{14} approximates to $1/e$), which is based on the Kuroshio front fluctuation in the East China Sea with period ranged between 5 and 30 d (e.g., Qiu et al., 1990; James et al. 1999). $\mathbf{K}_l$ is the Kalman gain in lateral boundary. $\mathbf{\Gamma'}_b$ is basically same as the components of $\mathbf{\Gamma'}$ at the lateral boundary. The data assimilation domain is the East China Sea west of the Ryukyu and Kyushu Islands (Fig. 4-3). Only results in the data assimilation domain are shown in this study.

4.4 Experiments

4.4.1 Experiment design

Twin experiment (e.g., Fukumori and Malanotte-Rizzoli 1995) was frequently used to study the satellite altimeter data assimilation. In this study, true solutions of the twin experiment are given by RS. The other experiments are carried out from 1 January 2014 using the same model. These experiments can be divided into 3 groups, which is summarized in Tab. 4-2. The first group has one experiment named as ND, which is a 2-year simulation without data assimilation. The results of ND in 2015 are regarded as RS. The other two groups are two series of experiments named as QS and QL. They assimilate the pseudo-observations of SLA subsampled from RS with time interval of 1 day. The temporal and spatial positions of these pseudo-observations follow to the multi-satellite altimeter observations of AVISO in the year 2014.

For the second group QS, $\mathbf{\Gamma'}_s$ is used to study the effect of modified surface meteorological conditions (horizontal wind stress, shortwave heat flux, and precipitation) on the model state. The corresponding linearized model Eq. 4-4 can be expressed as:

$$\mathbf{x}'^f_t = \mathbf{A}'\mathbf{x}'^a_{t-1} + \mathbf{G}'_s\mathbf{w}'_{s,t-1} + \mathbf{\Gamma}'_s\mathbf{q}'_{s,t-1} \tag{4-11}$$

where $\mathbf{G}'_s$ is the linearized surface forcing operator, and $\mathbf{w}'_s$ is the surface meteorological forcing, and $\mathbf{q}'_s$ is the process noise from surface meteorological conditions. Then $\mathbf{\Gamma}'_s$ can be estimated by the equation as follows:

$$\mathbf{\Gamma}'_s = \frac{\mathcal{F}\left(\mathbf{x}',\mathbf{w}'_s + \delta\mathbf{w}'_s\right) - \mathcal{F}\left(\mathbf{x}',\mathbf{w}'_s\right)}{\delta\mathbf{w}'_s} \tag{4-12}$$

where $\delta\mathbf{w}'_s$ represents the amount of perturbation in surface meteorological forcing $\mathbf{w}'_s$. The perturbation $\delta\mathbf{w}'_s$ in this study is 0.1 Pa for horizontal wind stress components, 1 W/m^2 for shortwave heat flux, and 1 mm/hr for precipitation.

Then Eq. 4-3 becomes

$$\mathbf{P}'^f_t = \mathbf{A}'\mathbf{P}'^a_{t-1}\mathbf{A}'^T + \gamma_s\mathbf{\Gamma}'_s\mathbf{Q}'_s\mathbf{\Gamma}'^T_s \tag{4-13}$$

where γ_s is a positive factor whose value increases from 0.02 in experiment QS002 to 1.0 in experiment QS1 (Tab. 4-2). The process noise for QS then can be modulated by changing the value of γ_s. The assimilated data coverage by QS is over the East China Sea which is illustrated by the positions of multi-satellite altimeter observations in Fig. 4-2.

Finally, the corresponding lateral boundary conditions increment term $\mathbf{b}_s$ becomes as follows:

$$\mathbf{b}'^f_{s,t} = \beta\mathbf{b}'^a_{s,t-1} + \mathbf{\Gamma}'_{s,b}\mathbf{q}'_{s,t-1} \tag{4-14}$$

where $\mathbf{\Gamma}'_{s,b}$ is basically same as the components of $\mathbf{\Gamma}'_s$ at the lateral boundary.

For the third group QL, the effect of modified lateral boundary conditions (temperature, salinity, horizontal velocities, and sea surface height) on the model state is reflected by $\mathbf{\Gamma'}_l$, which equals to the amount of $\mathbf{A'}$ in lateral boundary points. The corresponding linearized equations are same as Eqs. 4-11 and 4-14 but the subscript "s" is replaced with "l".

For instance, Eq. 4-3 can be rewritten as

$$\mathbf{P'}_t^f = \mathbf{A'}\mathbf{P'}_{t-1}^a \mathbf{A'}^T + \gamma_l \mathbf{\Gamma'}_l \mathbf{Q'}_l \mathbf{\Gamma'}_l^T \tag{4-15}$$

where γ_l is another positive factor whose value is 0.1 for the experiments of subgroup QL01 and 1.0 for the experiments of subgroup QL1 (Tab. 4-2). The lateral boundary points used in QL are mainly in the western boundary (Fig. 4-3), where the variability of the Kuroshio current in the upstream area propagates eastward. Additionally, the influence of assimilated data coverage on QL is also studied by the experiments in each subgroup. The "w2" shown in Tab. 4-2, for example, means that the data in the East China Sea between 126°E and 128°E are assimilated in the experiments.

The boundary forcing error covariance matrices (process noise) $\mathbf{\Gamma'}_s \mathbf{Q'}_s \mathbf{\Gamma'}_s^T$ and $\mathbf{\Gamma'}_l \mathbf{Q'}_l \mathbf{\Gamma'}_l^T$, and observation data error covariance matrix $\mathbf{R}$ are assumed to be diagonal matrices in this study. The ranges of diagonal components of these covariance matrices are shown in Tab. 4-3. First, the upper limits of the surface meteorological forcing error covariances are determined by calculating the variances of hourly meteorological forcing data (horizontal wind stress, shortwave heat flux, and precipitation). Next, the lateral boundary forcing error covariances are estimated from the 6-year average results of another DR_Ep model simulation from the year 2014 with temperature and salinity relaxed to DR_M model. Their variances at each boundary point of coarse grid are calculated and regarded as the diagonal components of the lateral boundary forcing error covariances. Finally, the diagonal components of observation error covariance are assumed to be in the same order as the residual variance of daily mean sea surface height shown in Fig. 4-4a.

74

4.4.2 Simulation without data assimilation

In this subsection, the results of ND are described. The temperature and horizontal velocities at 1 m and 200 m depths are averaged over the year 2014 and shown in Fig. 4-5. The Kuroshio current transports warm water with sea surface temperature greater than 25°C northeastward along the Okinawa Trough and turns to the east around 129°E (Fig. 4-5a). It can be seen that the western boundary conditions control the current speed and temperature of the Kuroshio current, so the data assimilation near the western boundary may be crucial to the representation of ocean state. We can also find a warm tongue around 129.5°E, 31.5°N west of the southern end of the Kyushu Island, which may be due to the warm eddies separated from the Kuroshio current (Qiu et al. 1990). The current field at 200 m depth has similar feature, but the temperature gradient is stronger than the surface layer (Fig. 4-5b). The western boundary conditions also control the state of the Kuroshio current as in the surface layer, although the western open boundary only exists in the area south of 27.5°N at 200 m depth. This suggests that the effect of data assimilation below the surface layer is also important to the representation of the Kuroshio current.

To study the variability of sea surface height and temperature, the root-mean-square differences (RMSDs) of their daily mean values between the years 2014 and 2015 are calculated, and the results are shown in Fig. 4-4. The black line stands for the mean Kuroshio current axis at 50 m depth derived from the 2-year results of ND. Large RMSD of sea surface height appears near the Kuroshio current axis (Fig. 4-4a). The maximum value exceeds 14 cm around 129°E west of the Tokara Strait, which is due to the Kuroshio front fluctuation studied by Qiu et al. (1990). The RMSDs of temperature in the surface, subsurface, and deep layers are shown in Fig. 4-4b–d, respectively. The RMSD of temperature is similar to that of sea surface height, although the pattern in the surface layer has large values at both inshore and offshore sides of the Kuroshio current. This

implies that the satellite altimeter data assimilation can reduce the RMSD through adjusting the phase of the Kuroshio front fluctuation. The RMSD has large value in the subsurface layer (Fig. 4-4c). The maximum value can be up to 2.2°C west of the Tokara Strait. These results imply that lateral forcing may be crucial for the representation of the ocean state, especially in the subsurface layer.

4.4.3 Surface boundary control

In this section, we calculate the RMSDs of temperature as a function of depth to determine the optimal process noise of QS. The decreasing of RMSD for salinity and horizontal velocities relative to ND is not significant in the data assimilation experiments, so we only focus on the RMSD of temperature in this study.

We try to minimize the RMSD by modulating the value of γ_s in Eq. 4-13. The RMSD calculated over the East China Sea is shown in Fig. 4-6a. The black dots indicate the RMSD for ND. It reaches a peak which is greater than 1.5°C around 170 m depth. This is consistent with the large value of subsurface layer shown in Fig. 4-4c. The lines with different colors are the results of QS experiments. It can be seen that QS01 (black line) performs the best above 100 m depth. All the QS experiments below 150 m depth show minor difference from ND case, indicating that the effect of surface forcing control decreases to depths. For the area south of 30°N where the water can be deeper than 2000 m depth, the RMSDs of QS experiments are very close to ND at all levels (Fig. 4-6b), which implies surface meteorological condition data assimilation may be not fit for deep areas. On the other hand, over the area north of 30°N where the water depth is shallow (Fig. 4-6c), the curves show similar pattern as Fig. 4-6a. QS02 has lower RMSD than QS01 below 75 m depth. However, the value of QS02 above this depth is greater than QS01.

76

To further discuss the optimal process noise for surface forcing, the RMSDs of temperature over the area north of 30°N above 100 m depth are calculated and shown in Fig. 4-7a. It is worth noticing that QS01 has the lowest RMSD of all the QS experiments. As a result, $0.1\mathbf{\Gamma'_s}\mathbf{Q'_s}\mathbf{\Gamma'_s}^T$ is determined to be the process noise for surface forcing. The results between 100 m and 500 m depth (Fig. 4-7b) show minor differences among these experiments, indicating the effect of surface forcing control decreases to depths.

4.4.4 Lateral boundary control

To determine the optimal process noise for QL, the RMSDs of temperature as a function of depth are calculated as subsection 4.4.3 and shown in Fig. 4-8. In experiments of QL01, the original process noise $\mathbf{\Gamma'_l}\mathbf{Q'_l}\mathbf{\Gamma'_l}^T$ is multiplied by 0.1. Comparing the results of QL1w2 (yellow line) with original process noise and QL01w2 (black line) over the East China Sea (Fig. 4-8a), it can be found that the original process noise is overestimated, and the QL1w2 performs even worse than ND below 300 m depth. Therefore, we regard $0.1\mathbf{\Gamma'_s}\mathbf{Q'_s}\mathbf{\Gamma'_s}^T$ as the optimal process noise for QL.

Additionally, the QL results with different assimilation data coverage for QL01 are also compared (Fig. 4-8a). We can find that QL01w2 performed better than QL01w1 (purple line) or QL01w3 (blue line), although QL01w3 has lower RMSD than QL01w1 above 175 m depth. It is noted that the experiments with largest assimilated data coverage QL01w3 (QL1w3) perform worse than other experiments of QL01 (QL1). This is probably because of the strong nonlinear behavior of the jet advection (Fukumori and Malanotte-Rizzoli 1995). Thus, the linear assumption of the data assimilation method used in this study did not work well for the lateral boundary correction using remote (~ 300 km) measurement data.

If we divided the domain into four areas based on the distance away from the western boundary, the results are shown in Fig. 4-8b–e. The experiment QL01w2 shows the smallest RMSD

in deep layer except the results over the area of 126–127°E, where QL1w1 performs the best (Fig. 4-8b). This suggests that lateral boundary condition data assimilation is more effective for small area close to the lateral boundary. It can be also found that the lowest RMSD curves by the QL experiments become closer to ND as the distance away from the western boundary increases. This is because the effect of lateral control becomes weak due to strong nonlinearity of the model.

In conclusion, QL01w2 performs the best in the deep layer over the East China Sea, so $0.1\boldsymbol{\Gamma'}_1\mathbf{Q'}_1\boldsymbol{\Gamma'}_1^T$ is determined to be the process noise and the assimilated data are over the area west of 128°E.

4.4.5 Comparison of surface and lateral boundary effects

The RMSDs of temperature at 50 m depth for ND and the experiments with optimal process noise (QS01 and QL01w2) are calculated and shown in Fig. 4-9. The area north of the Kuroshio current axis shows relatively high RMSD value that can exceed 1.8°C because of the different phases of the Kuroshio front fluctuation between ND in 2014 and RS. There is another high RMSD area west of the southern end of the Kyushu Island (Fig. 4-9a). It may be because of the warm eddies separated from the Kuroshio current (Qiu et al. 1990), which are also shown in Fig. 4-5a. This high RMSD is reduced to about 1.0°C by QS01 (Fig. 4-9b) and about 1.4°C by QL01w2 (Fig. 4-9c), indicating that surface forcing control is more effective than lateral one in this area. However, for the area south of 30°N close to the Kuroshio current axis, the RMSD of QL01w2 is basically lower than QS01, implying that lateral forcing control is more effective than its counterpart.

To further compare the effects of surface and lateral boundary forcings, the RMSD profiles above 1000 m depth along 127°E section are shown in Fig. 4-10. The reduced value of RMSD by QL01w2 can exceed 0.2°C at 28°N around the Kuroshio current axis, while the decreasing by QS01 is insignificant. Figure 4-11 shows the RMSDs of temperature at 200 m depth. The decreasing by

QL01w2 is obvious in the area north of the Kuroshio current axis around 129°E, while the RMSD value of QS01 is very close to or even greater than that of ND. These comparisons suggest that lateral forcing control can improve the representation of the Kuroshio current that depends much on its upstream conditions. The previous numerical experiments (Evensen 1993) also showed that the effect of data assimilation is significant near the lateral boundary with strong inflow, which was ascribed to the signal at the boundary propagating into the domain repeatedly. Therefore, we conclude that lateral boundary condition data assimilation is promising around the upstream area of strong currents, especially in the deep layer. Conversely, in the shallow area north of 30°N shown in Fig. 4-10, QS01 reduces the RMSD, while the value of QL01w2 is greater than that of ND. Thus, for shallow areas, surface meteorological condition data assimilation performs better than its counterpart.

The cross-spectral analysis (Thomson and Emery 2014) is also carried out to study the effect of lateral forcing control on variances at different time scales. Figure 4-12 shows the coherence curves of temperature time series at 127°E, 28°N, 300 m depth for ND and QL01w2. The higher coherence reflects that the data assimilation is effective at certain period. The dashed line is the critical value of the F test at 95% confidence level. The comparison between ND and QL01w2 indicates that the coherence of QL01w2 increases maximally by about 0.3 with periods longer than about 22 d. This indicates that the satellite altimeter data assimilation can improve the representation of the long-term Kuroshio current variability. However, the cross-spectral analysis also implies that the high-frequency variability of Kuroshio current axis position may not be easily improved only by assimilating multi-satellite altimeter observations. This is because of strong flow instabilities with short temporal and spatial scales (Smedstad et al. 1997) and sparse distribution of the satellite altimeter data. Therefore, more measurements are needed to promote the representation of Kuroshio front fluctuations with periods around 10 and 20 d (e.g., Sugimoto et al 1988; Qiu et al. 1990) in the East China Sea.

The further study indicates that the incoming transports of Kuroshio has the similar tendency. At the western boundary, the annual-mean transport of Kuroshio for the ND experiment is 26.1 Sv, which is 2.2 Sv weaker than the RS experiment (28.3 Sv). The transport stays weak for QS01, but increases to 27.9 Sv by QL01w2. The low-frequency variation seems to be corrected effectively by the lateral boundary updates. On the other hand, the RMSD and correlation coefficient relative to the RS experiment are improved only slightly from ND to QL01w2 experiments, indicating the difficulty to control high-frequency transport variability.

4.5 Summary and discussion

The satellite altimeter data assimilation into the regional ocean model DR_Ep based on the reduced-order Kalman filter was studied. Process noise was traditionally ascribed to surface meteorological conditions. However, the effect of surface meteorological condition data assimilation may not propagate into deep layers. Therefore, we attempted to assimilate the altimeter data using lateral boundary condition data assimilation, as well. To minimize the RMSD of temperature, twin experiments (Tab. 4-2) were carried out through assimilating pseudo-observations of SLA and comparing the results with RS. These SLA data were subsampled from RS, and their temporal and spatial positions followed to the AVISO multi-satellite altimeter observations. The data assimilation domain was limited in the East China Sea because of the large computational requirements by data assimilation over all model domain (Fig. 4-3).

The results of twin experiments indicated that QS01 (QL01w2) has the least RMSD of temperature in the QS (QL) experiments. It is noted that the optimal error covariances were found at around 10% of forcing variances for both the surface and lateral boundary conditions. Then, we compared surface meteorological and lateral boundary condition data assimilation through calculating the RMSDs of temperature for QS01 and QL01w2 (Figs. 4-9 and 4-10). The results

showed that only the latter one can propagate into deep layers (Fig. 4-10). The initial value and annual mean in 2014 of diagonal average temperature part of **P**′ also indicate this conclusion (Fig. 4-13). The thin line is the initial value calculated by doubling algorithm without observation data, while the thick line is the annual average over 2014. For QS01, **P**′ is large only in the surface layer, so the error cannot propagate to depths for surface boundary data assimilation. The diagonal values of **P**′ for QL01 are large in both the surface and subsurface layers, and the error can propagate to depths, although its surface values are lower than QS01. The surface boundary data assimilation (solid line) can reduce the diagonal values of **P**′ only for surface layer, while the lateral boundary data assimilation (dashed line) can reduce them not only for surface layer but also for subsurface and deep layers. This indicates that the effect of lateral (surface) boundary data assimilation can (cannot) propagate to depths. Other diagonal components of **P**′ such as salinity and velocities have similar pattern (not shown). On the other hand, for the area north of 30°N where the water depth is shallow, surface forcing control is more effective than its counterpart (Figs. 4-9 and 4-10).

To study the effect of lateral forcing control on variances at different time scales, the cross-spectral analysis was also carried out (Fig. 4-12). The results indicated that the long-term Kuroshio current variability can be improved by assimilating satellite altimeter data. The results also suggested that high-frequency variability of the Kuroshio current may not be easily improved only by assimilating multi-satellite altimeter observations due to strong flow instabilities and sparse distribution of the satellite altimeter data. Therefore, other types of measurements such as CTD and ADCP may be needed to improve the representation of the Kuroshio front fluctuations.

In the previous literature, it was found that the Kuroshio front fluctuation propagates downstream with a speed about 20 to 26 cm/s (Qiu et al. 1990). Given the *e*-folding damping time scale of 14 d for the increment of lateral boundary condition, the maximum propagating distance of the Kuroshio front fluctuation signal from the lateral boundary is about 300 km. This suggests that the area 300 km away from the western boundary along the Kuroshio current cannot be effectively

modified by lateral forcing control, which may be only fit for regional model data assimilation over limited area. The reason for that QL1w3 (QL01w3) performed worse than QL1w2 (QL01w2) may also be associated with strong nonlinear effect of the jet advection. This study revealed that the linear sparse KF performs well with the measurement data within 200 km only from the western boundary. The nonlinear inverse problem for distant relationship can be overcome if we use the nonlinear ensemble Kalman filter with its flow-dependent features in the future.

Based on these results, we will attempt to develop a regional ocean forecast system in the future. We hope it can provide a swift and accurate prediction of background fields at all levels to fishery, ocean power, navigation safety, and so on.
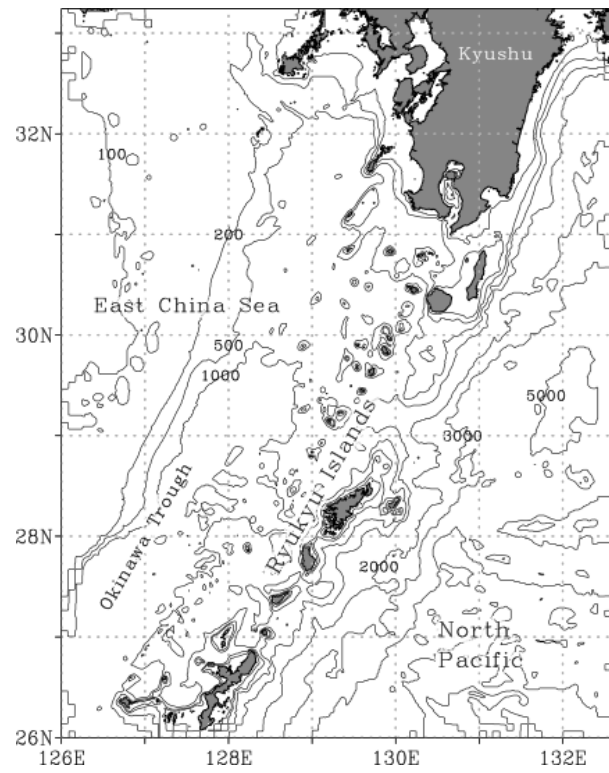
Fig. 4-1 Topography (m) of model domain
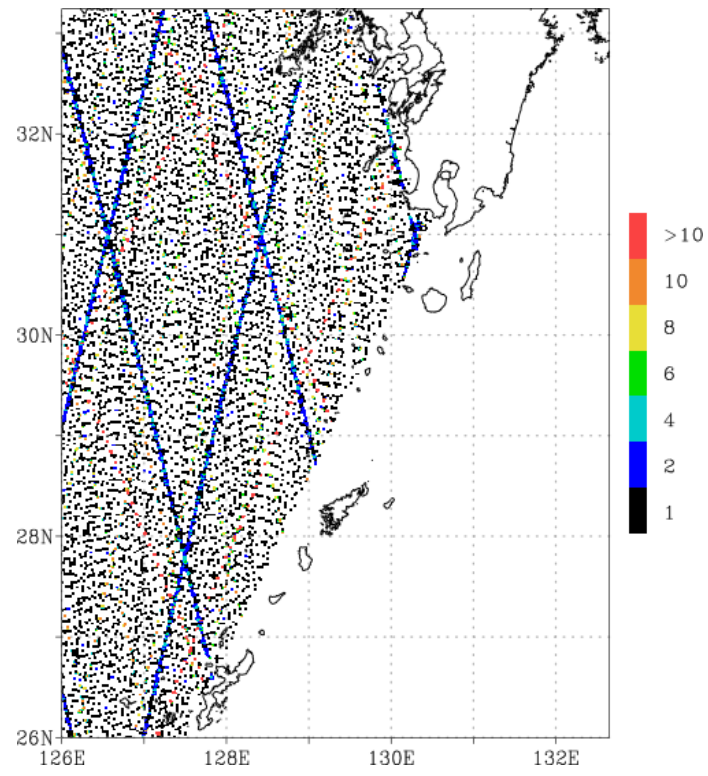
Fig. 4-2 Number of multi-satellite altimeter observations in 2014
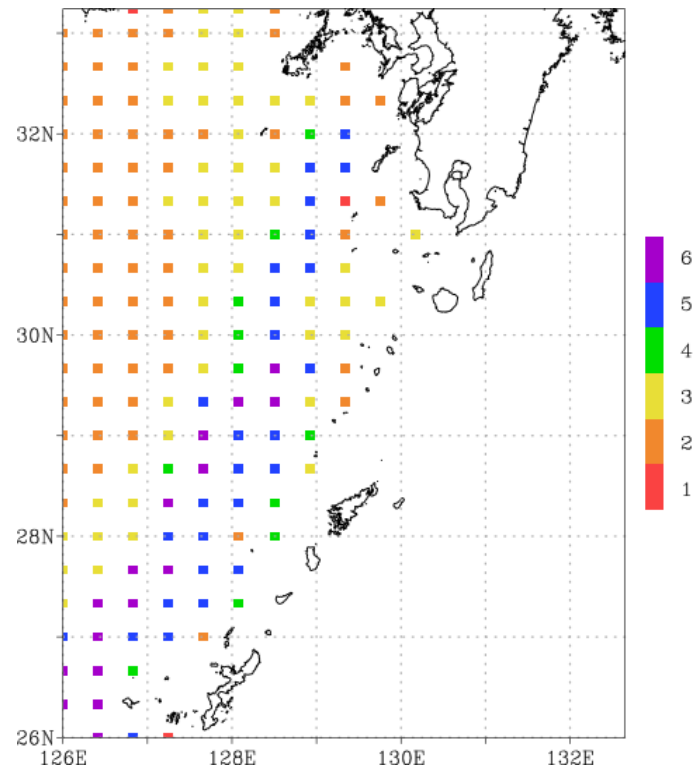
Fig. 4-3 Reduced-order model grid system for error covariance calculation. The color stands for the

total number of vertical levels
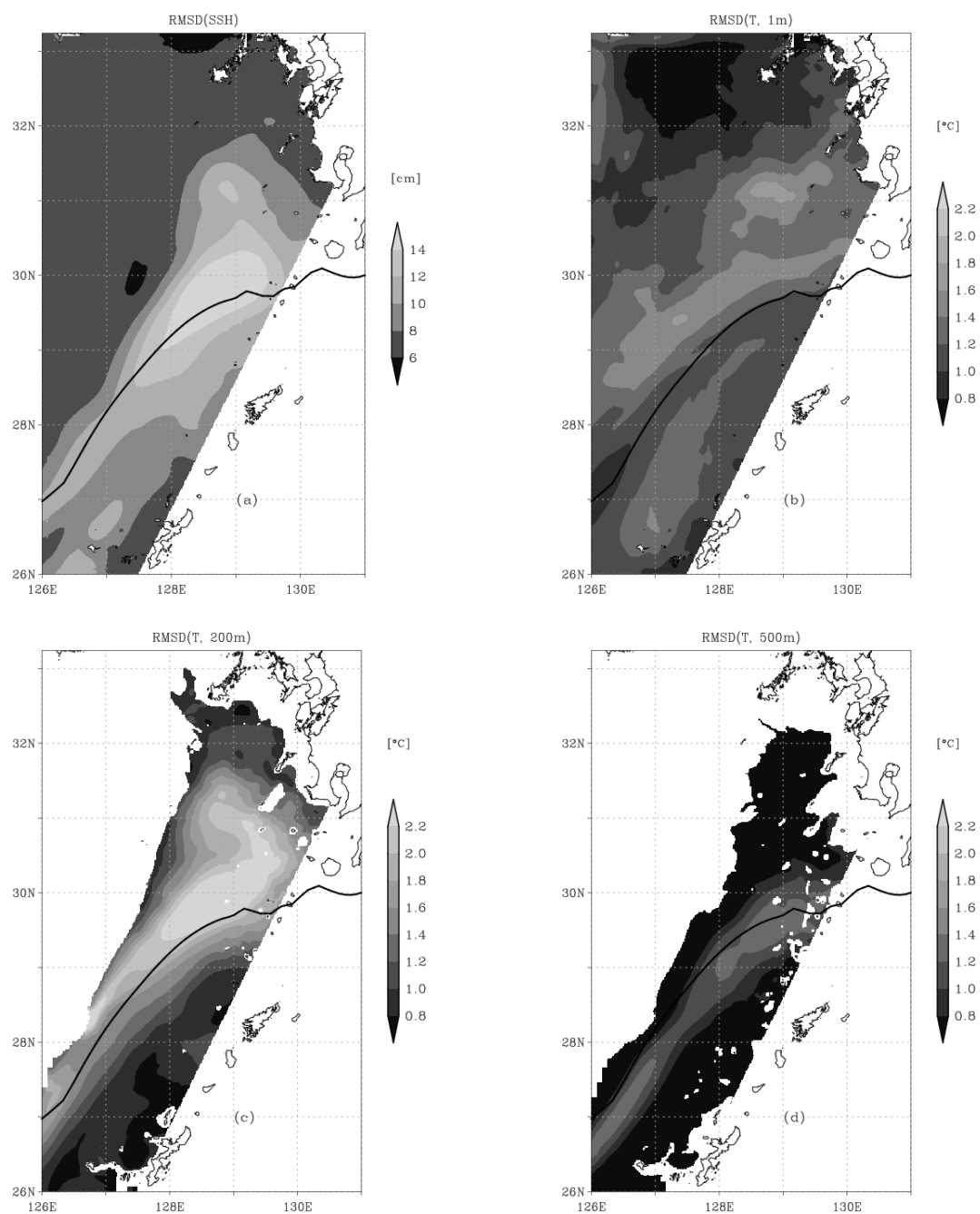
Fig. 4-4 RMSDs of daily mean (a) sea surface height (cm) and temperature (°C) at (b) 1 m, (c) 200 m, and (d) 500 m between the simulations of the year 2014 and 2015. The black line shows the mean Kuroshio current axis at 50 m
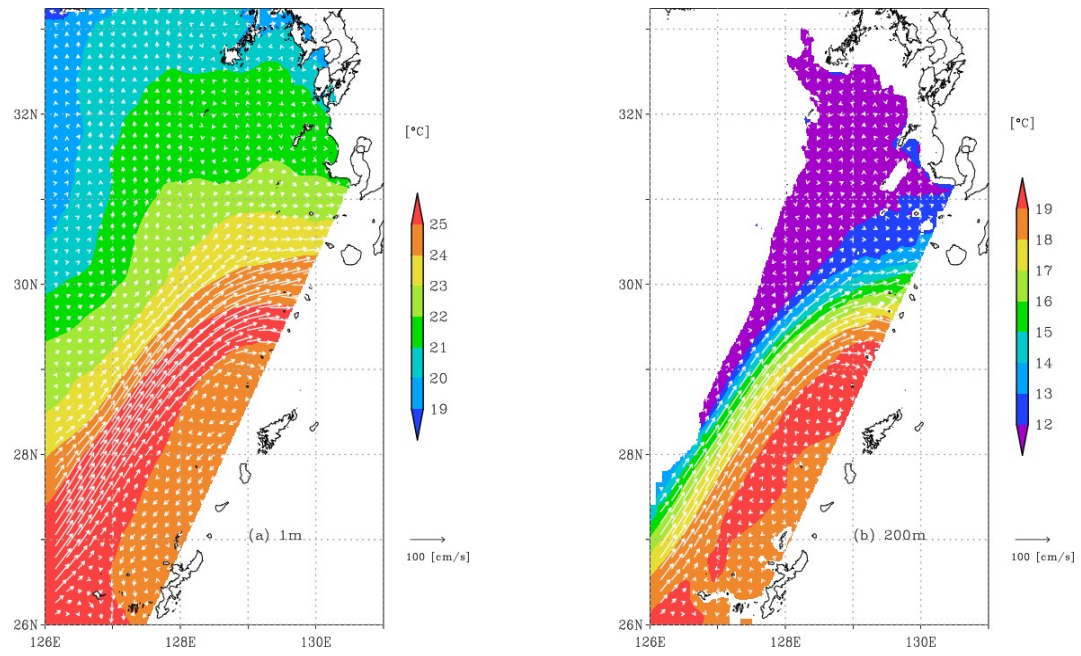
Fig. 4-5 Simulated temperature (°C) and horizontal current vectors (cm/s) averaged over the year

2014 at (a) 1 m and (b) 200 m depth
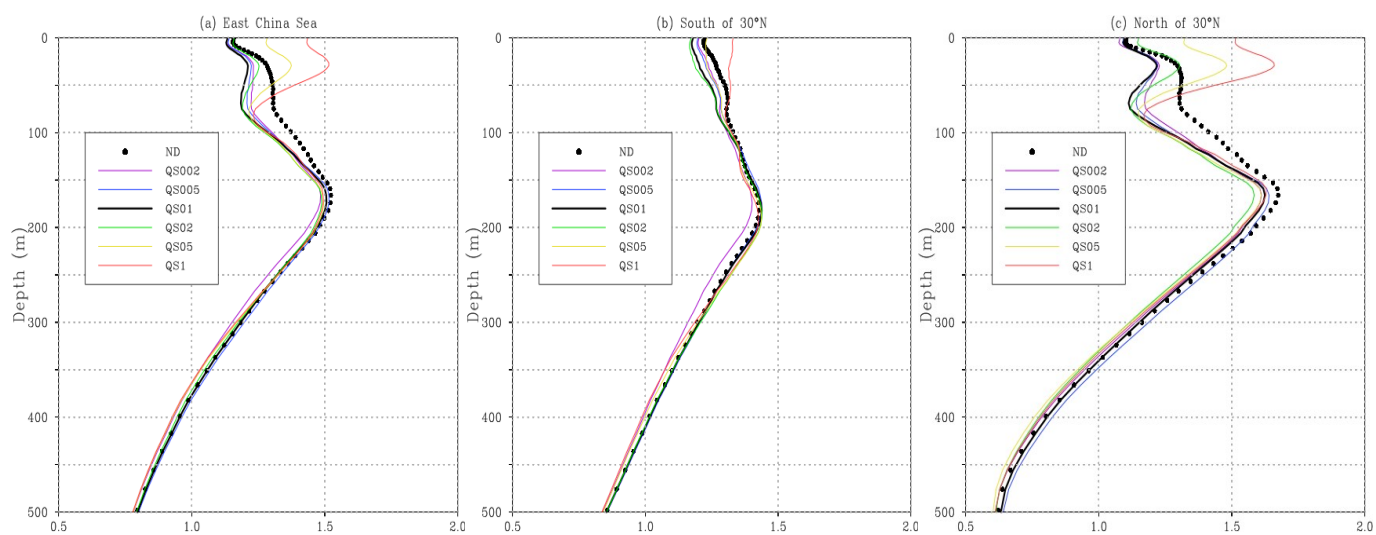
Fig. 4-6 RMSDs of temperature (°C) as a function of depth for QS over (a) the East China Sea, (b) the area south of 30°N, and (c) the area north of 30°N
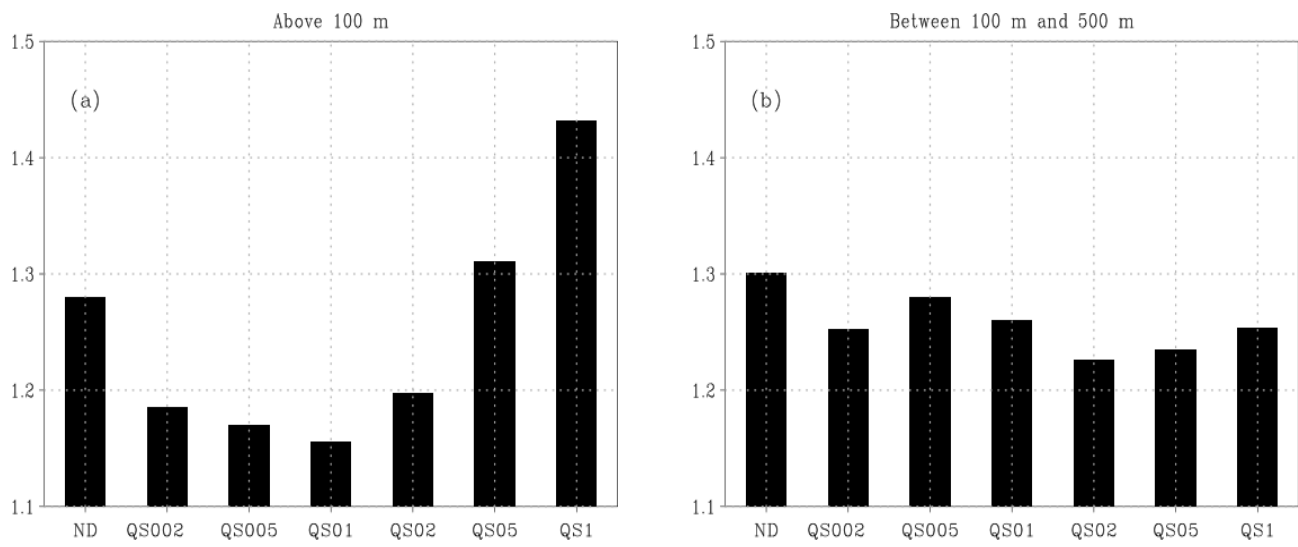
Fig. 4-7 RMSDs of temperature (°C) for QS over the area north of 30°N (a) above 100 m depth and

(b) between 100 m and 500 m depth
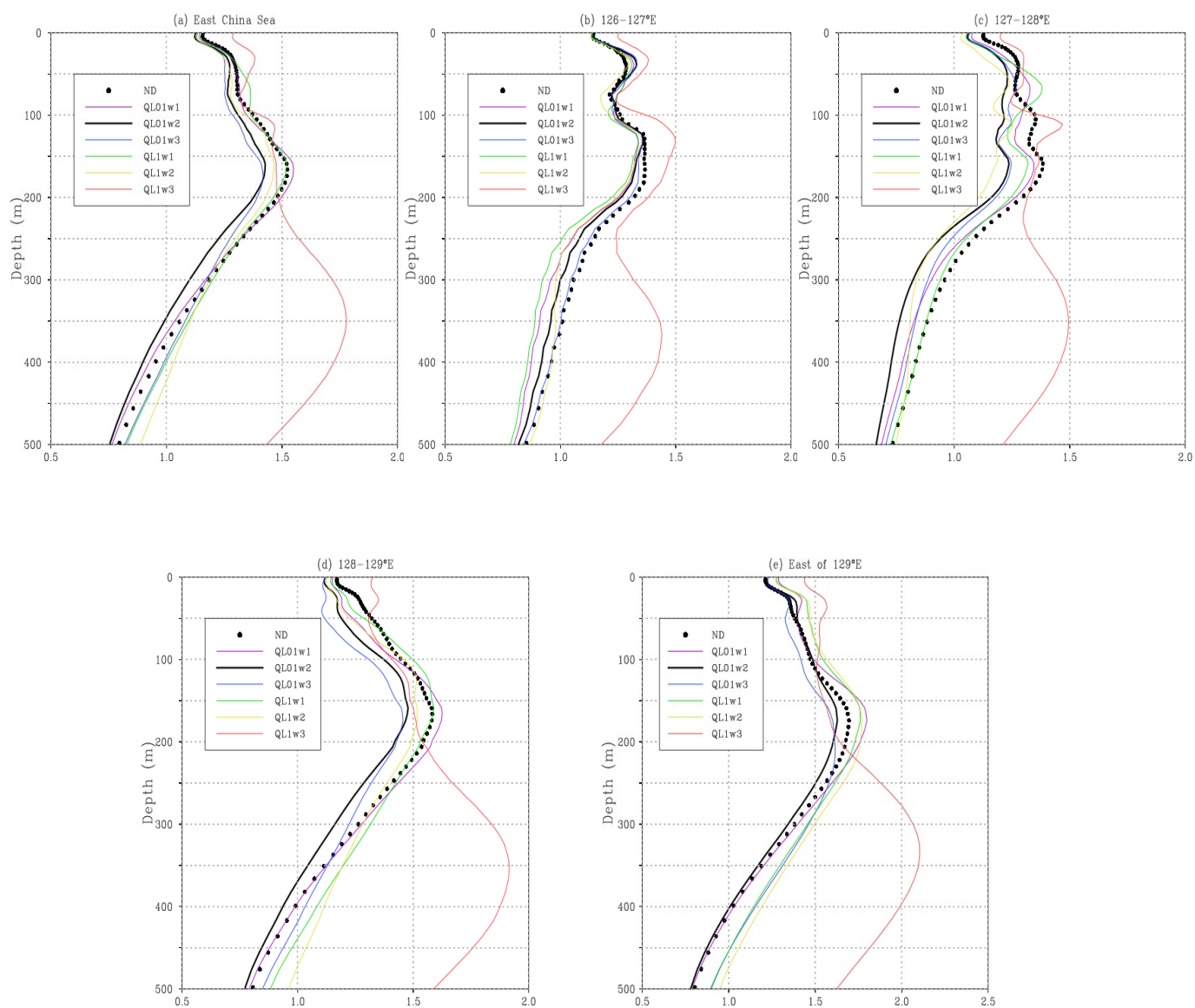
Fig. 4-8 RMSDs of temperature (°C) as a function of depth for QL over (a) the East China Sea, (b) the area of 126-127°E, (c) the area of 127-128°E, (d) the area of 128-129°E, and (e) the area east of 129°E
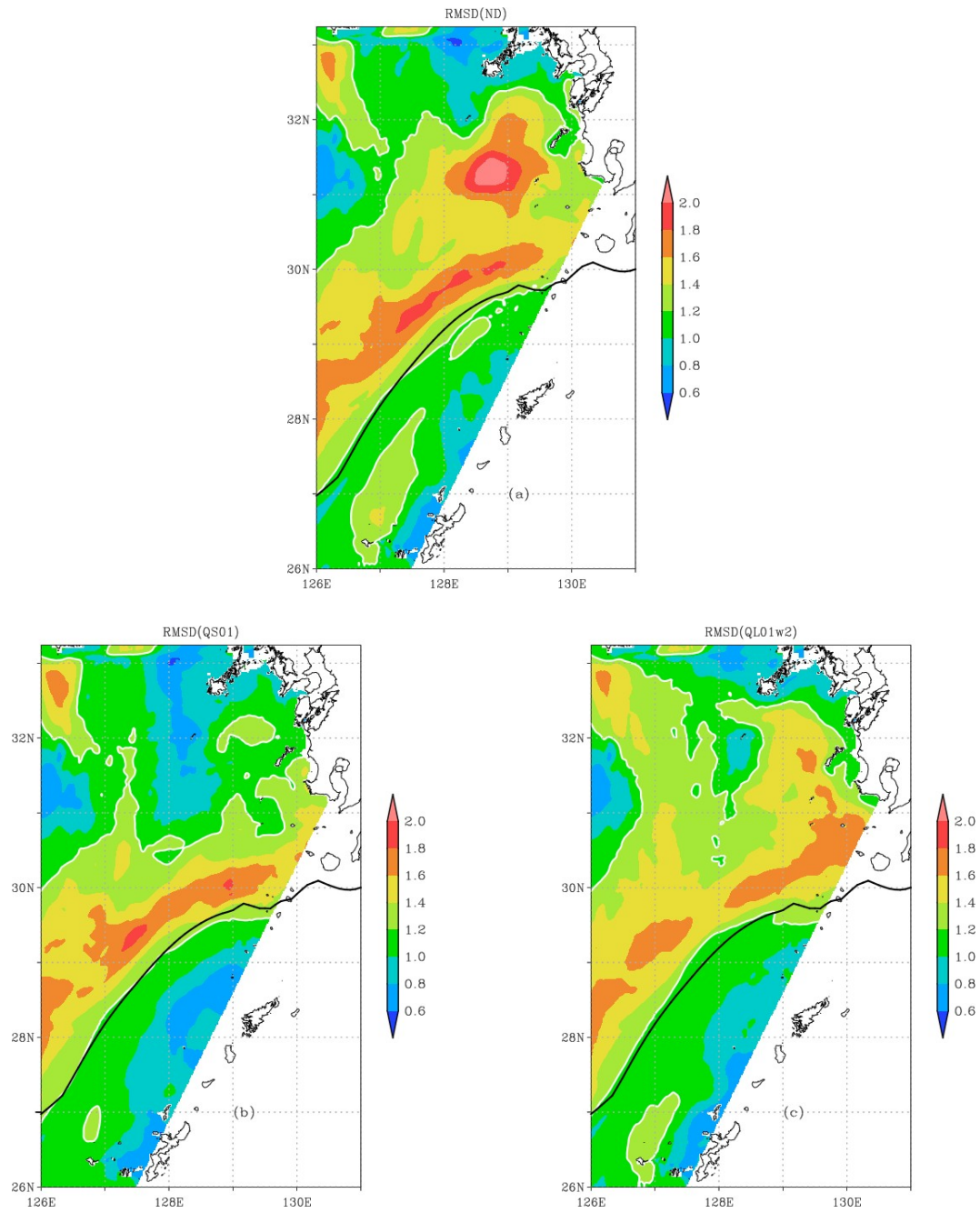
Fig. 4-9 RMSDs of temperature (°C) at 50 m depth for (a) ND, (b) QS01, and (c) QL01w2. The

black line shows the mean Kuroshio current axis at 50 m. The white solid line is the contour of

1.2°C
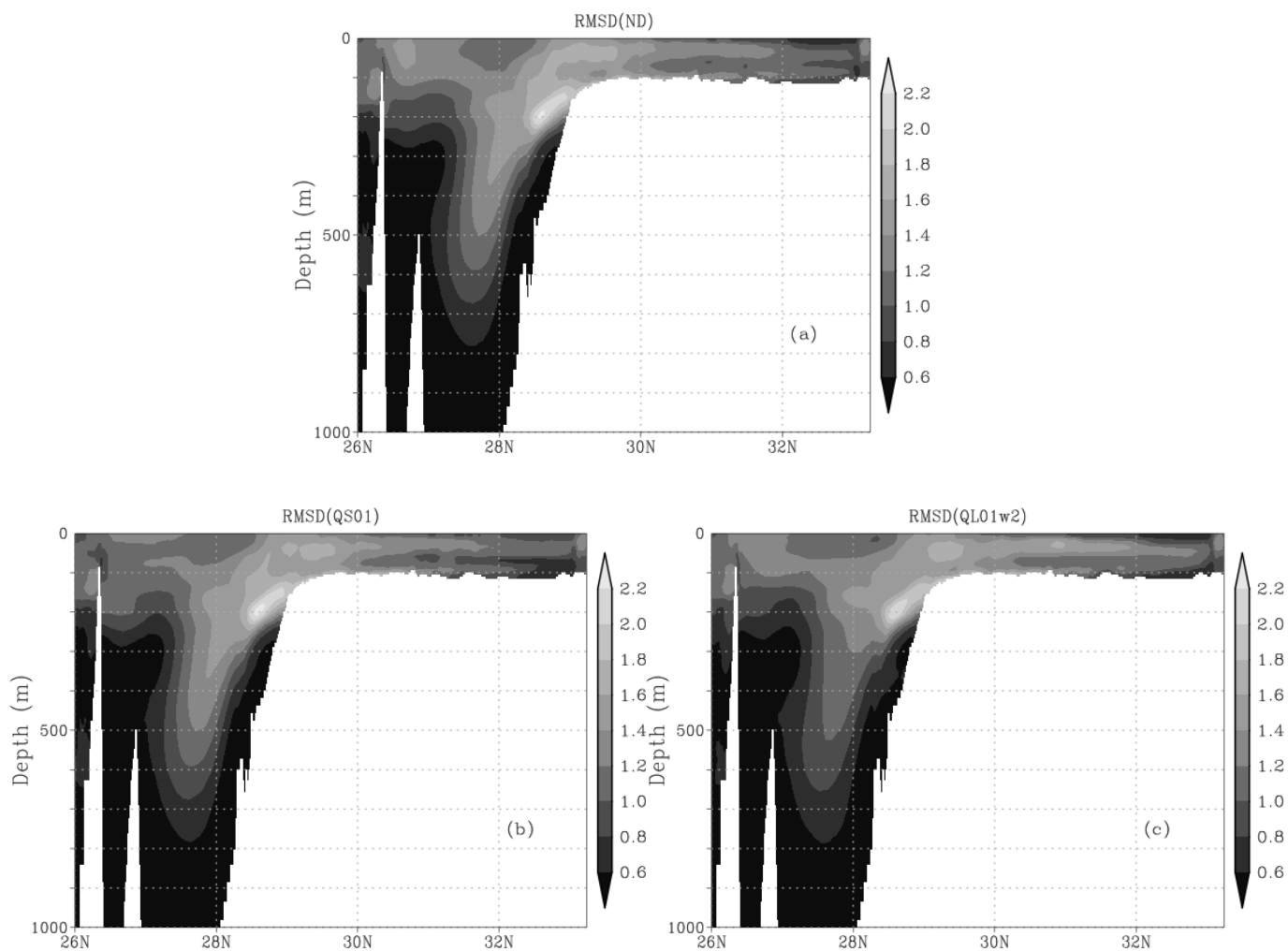
Fig. 4-10 RMSDs of temperature (°C) along the 127°E section for (a) ND, (b) QS01, and (c)
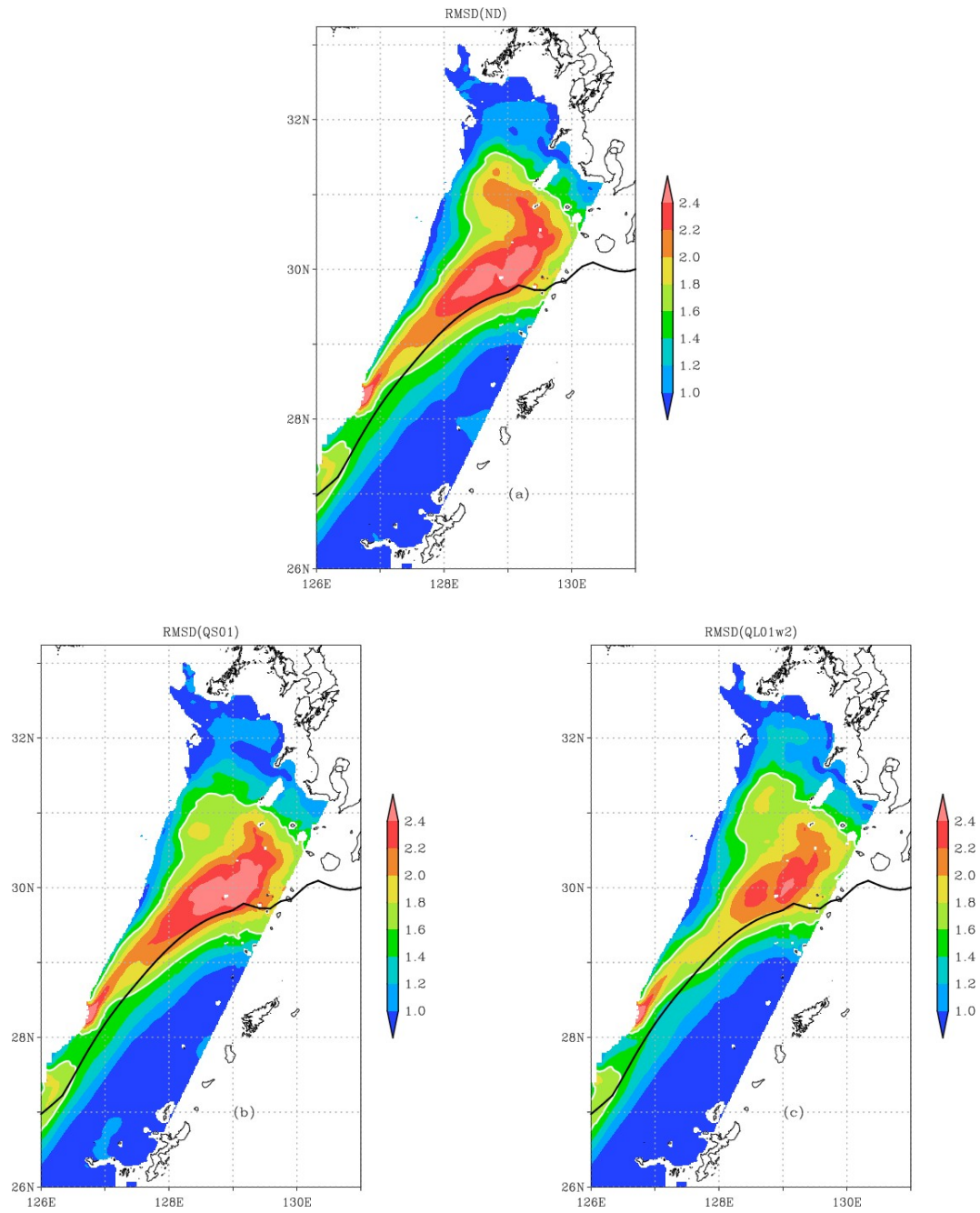
QL01w2

Fig. 4-11 Same as Fig. 4-9 but at 200 m depth. The white solid line is the contour of 1.6°C
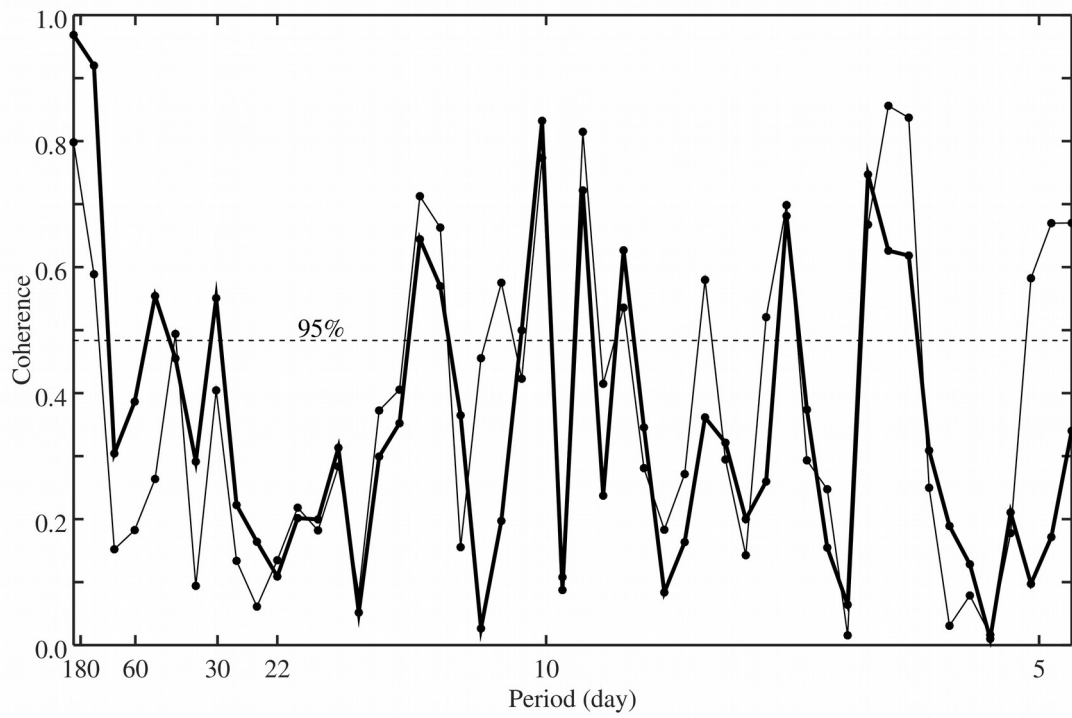
Fig. 4-12 Coherence curves between RS and two experiments for temperature time series at 127°E, 28°N, 300 m depth. The thin and thick curves indicate ND and QL01w2, respectively. The dashed line shows the critical value of the F test at 95% confidence level
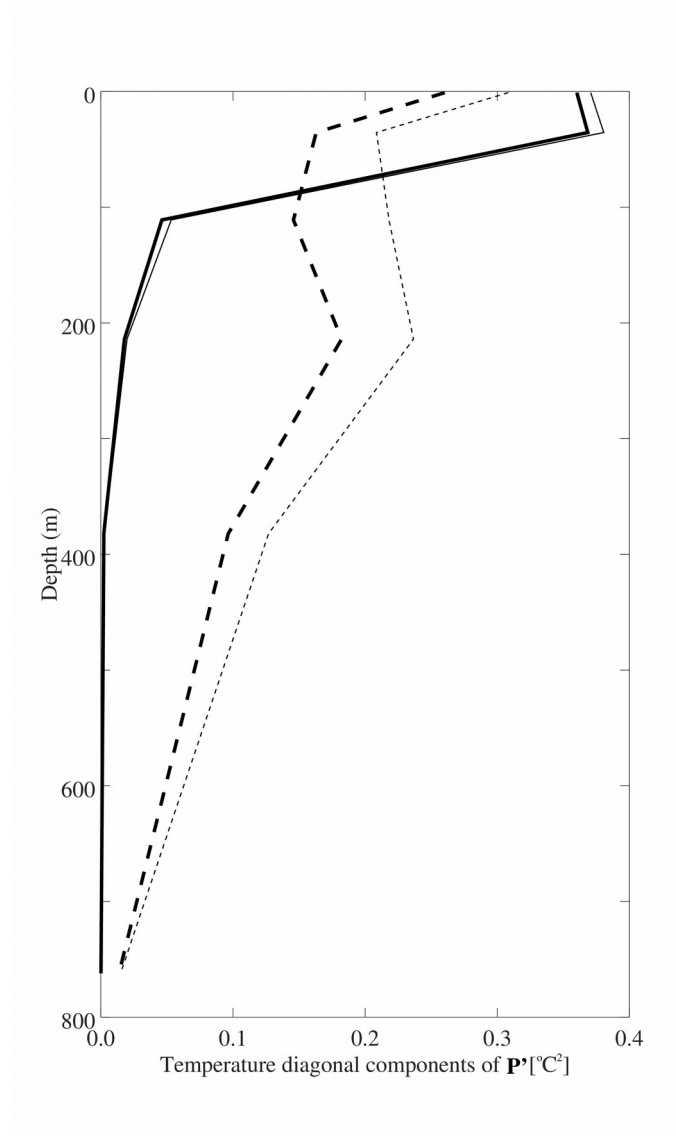
Fig. 4-13 Initial value (thin) and annual mean (thick) in 2014 of the diagonal average temperature

part of **P**'. The solid line indicates the result of QS01, while the dashed line indicates the result of

QL01

Table 4-1 Main characteristics of altimeter missions used in this study

Mission	Cycle duration (day)	Inter-track distance at equator (km)
Cryosat-2	29	98
HaiYang-2A	14	210
OSTM/Jason-2	10	315
SARAL/Altika	35	80

Table 4-2 Experiments in this study

Experiments	γ	Data coverage
ND	---	---
QS002	0.02	East China Sea
QS005	0.05	East China Sea
QS01	0.1	East China Sea
QS02	0.2	East China Sea
QS05	0.5	East China Sea
QS1	1	East China Sea
QL01w1	0.1	west of 127°E
QL01w2	0.1	west of 128°E
QL01w3	0.1	west of 129°E
QL1w1	1	west of 127°E
QL1w2	1	west of 128°E
QL1w3	1	west of 129°E

Table 4-3 Ranges of diagonal components of error covariance matrices of boundary forcing and

observation data

Surface meteorological forcing	zonal wind stress	0.1^2 Pa^2
	meridional wind stress	0.1^2 Pa^2
	shortwave heat flux	100^2 $(W/m^2)^2$
	precipitation	1^2 $(mm/hr)^2$
Lateral boundary forcing	temperature	0.237^2–2.26^2°C^2
	salinity	0.0005^2–0.474^2 psu^2
	zonal velocity	1.84^2–23.0^2 $(cm/s)^2$
	meridional velocity	1.26^2–23.3^2 $(cm/s)^2$
	sea surface height	4.75^2–7.20^2 cm^2
Observation data	sea surface height	10^2 cm^2

Chapter 5. General conclusions

This thesis attempted to establish a regional ocean forecasting system with high resolution. The models, DR_E, DR_Ek, and DR_Ep, used in this thesis are all based on RIAMOM over the area southwest of Japan. We hope this system will be used to select the proper site for ocean renewable power plant construction.

In Chapter 2, the DR_E model was used to represent the ocean state south of Japan. The ocean current power potential of the Kuroshio current was estimated based on the simulation results which were validated using the ADCP measurements. Three candidate areas for ocean current power generation experiment were assessed by comparing the average current speed, the stability of the current vector, and the ocean current power potential. To study the impact of Kuroshio large meander on the current field, two experiments during the periods with and without large meander were designed. The results showed that the average current speed around the Tokara Strait is the weakest of the three candidate areas. In addition, the current speed south of Cape Shionomisaki is the greatest among the candidate areas during non-large-meander period. However, the current speed and stability decrease significantly when the Kuroshio large meander appears. In contrast, the current is stable and strong in the area south of AS regardless of the Kuroshio large meander. Thus, the area south of AS is a promising site for ocean current power generation experiment, and the average ocean current power density there can reach 1 kW/m^2. However, an extraordinary strong and long-term Kuroshio large meander has been occurring from August 2017. The Kuroshio axis occasionally leaves far away from the coast south off Cape Ashizuri, which has not been expected by the results in Chapter 2. We also calculated 4 criteria to select the candidate area for ocean current power generation south of AS, and we found the maximum number of ocean current power plants constructed in the promising area is 378 (total power can be up to about 458 MW).

In Chapter 3, the ocean thermal energy potential around the Aguni Basin west of the Okinawa Island was estimated using DR_Ek model, considering the environmental limit of the deep water motion. To study the tidal effect, the simulation without tide was also conducted over the same period as the control run. In the Aguni Basin, the cold deep water intrusion cools the water, which is balanced by eddy diffusion. Based on this deep layer thermal equilibrium, we proposed the perturbation method estimating the ocean thermal energy potential. This method and a modified Wick-Schmitt method were compared with the original Wick-Schmitt method and Nihous method. The two traditional methods overestimated the OTEC power density, while two new approaches can improve the estimation. The results showed that the ocean thermal energy potential in the Aguni Basin is five orders greater than the present mechanical limit, which was attributed to vigorous tidal mixing. The results also indicated that strong and sustainable power generation is available northeast off Kumejima Island. The strong upwelling near the boundary of the Aguni Basin results from the strong mixing. The large OTEC power can be also expected in the East China Sea due to vigorous tidal mixing.

In Chapter 4, the satellite altimeter data assimilation into the DR_Ep model based on the approximate Kalman filter was studied. Twin experiments were carried out to compare the effects of surface and lateral boundary conditions data assimilation. The process noises of the surface and lateral boundary forcings were separately determined by minimizing the RMSD of temperature. The results showed that the traditional surface boundary conditions data assimilation performed well in shallow area of the model domain, but its effects decay rapidly to depth. By comparison, the lateral boundary control improved the surface and subsurface representation of the ocean state in deep area. The cross spectral analysis indicated that the long-term variability with period longer than several weeks can be effectively improved by assimilating satellite altimeter data. Thus, other types of measurements may be needed to promote the representation of the Kuroshio variations.

The future's work after these studies is to construct a high-resolution regional ocean forecast system which can accurately predict the background fields at all levels to fishery, ocean power, navigation safety, and so on.

References

Adiputra R, Utsunomiya T, Koto J, Yasunaga T, Ikegami Y (2020) Preliminary design of a 100 MW-net ocean thermal energy conversion (OTEC) power plant study case: Mentawai island, Indonesia. J Mar Sci Tech 25(1):48–68

Alford MH, Peacock T, MacKinnon JA, Nash JD, Buijsman MC, Centurioni LR, Chao SY, Chang MH, Farmer DM, Fringer OB, Fu KH, Gallacher PC, Graber HC, Helfrich KR, Jachec SM, Jackson CR, Klymak JM, Ko DS, Jan S, Johnston TMS, Legg S, Lee IH, Lien RC, Mercier MJ, Moum JN, Musgrave R, Park JH, Pickering AI, Pinkel R, Rainville L, Ramp SR, Rudnick DL, Sarkar S, Scotti A, Simmons HL, Laurent LCS, Venayagamoorthy SK, Wang YH, Wang J, Yang YJ, Paluszkiewicz T, Tang TY (David) (2015) The formation and fate of internal waves in the South China Sea. Nature 521(7550):65–69

Ambe D, Imawaki S, Uchida H, Ichikawa K (2004) Estimating the Kuroshio axis south of Japan using combination of satellite altimetry and drifting buoys. J Oceanogr 60(2):375–382

Awaji T, Akitomo K, Imasato N (1991) Numerical study of shelf water motion driven by the Kuroshio: Barotropic model. J Phys Ocean 21(1):11–27

Blayo E, Mailly T, Barnier B, Brasseur P, Le Provost C, Molines JM, Verron J (1997) Complementarity of ERS 1 and TOPEX/POSEIDON altimeter data in estimating the ocean circulation: Assimilation into a model of the North Atlantic. J Geophys Res 102(C8):18573–18584

Bretherton FP, Davis RE, Fandry CB (1976) A technique for objective analysis and design of oceanographic experiments applied to MODE-73. Deep Sea Res 23(7):559–582

Broquet G, Moore AM, Arango HG, Edwards CA (2011) Corrections to ocean surface forcing in the California Current System using 4D variational data assimilation. Ocean Model 36(1–2):116–132

Chang YC, Chu PC, Tseng RS (2015) Site selection of ocean current power generation from drifter measurements. Renew Energy 80(C):737–745

Chen F (2010) Kuroshio power plant development plan. Renew Sustain Energy Rev 14(9):2655–2668

Cummins PF, Masson D, Saenko OA (2016) Vertical heat flux in the ocean: Estimates from observations and from a coupled general circulation model. J Geophys Res 121(6):3790–3802

D'Arsonval JA (1881) Utilization des forces naturelles: Avenir del'electricite. Rev Sci Tech 17:370–372 (in French)

Davis BV, Farrell JR, Swan DH, Jeffers KA (1986) Generation of electrical power from the Florida Current of the Gulf Stream. In: Proceedings of the Eighteenth Offshore Technology Conference, Houston, TX, USA, pp. 353–360

De Mey P (1997) Data assimilation at the oceanic mesoscale: A review. J Met Soc Japan 75(1B): 415–427

Egawa T, Nagata Y, Sato S (1993) Seasonal variation of the current in the Tsushima Strait deduced from ADCP data of ship-of-opportunity. J Oceanogr 49(1):39–50

Evensen G (1993) Open boundary conditions for the extended Kalman filter with a quasi-geostrophic ocean model. J Geophys Res 98(C9):16529–16546

Evensen G (1994) Sequential data assimilation with a nonlinear quasi-geostrophic model using Monte Carlo methods to forecast error statistics. J Geophys Res 99(C5):10143–10162

Feng M, Mitsudera H, Yoshikawa Y (2000) Structure and variability of the Kuroshio Current in Tokara Strait. J Phys Ocean 30(9):2257–2276

Finkl CW, Charlier R (2009) Electrical power generation from ocean currents in the Straits of Florida: Some environmental considerations. Renew Sustain Energy Rev 13(9):2597–2604

Finney KA (2008) Ocean thermal energy conversion. Guelph Eng J 1:17–23

Francis PA, Jithin AK, Effy JB, Chatterjee A, Chakraborty K, Paul A, Balaji B, Shenoi SSC, Biswamoy P, Mukherjee A, Singh P, Deepsankar B, Reddy SS, Vinayachandran PN, Kumar MSG, Bhaskar TVSU, Ravichandran M, Unnikrishnan AS, Shankar D, Prakash A, Aparna SG, Harikumar R, Kaviyazhahu K, Suprit K, Shesu RV, Kumar NK, Rao NS, Annapurnaiah K, Venkatesan R, Rao AS, Rajagopal EN, Prasad VS, Gupta MD, Nair TMB, Rao EPR, Satyanarayana BV (2020) High-resolution operational ocean forecast and reanalysis system for the Indian Ocean. Bull Amer Meteor Soc 101(8):E1340–E1356

Friedland B (1969) Treatment of bias in recursive filtering. IEEE Trans Autom Contr 14(4):359–367

Fujimoto M, Momota M, Sakamoto H, Nakagawa N (1985) On the fluctuations of the stream axes of the Kuroshio southwest of Japan. Bull Nansei Reg Fish Res Lab 19:99–109 (in Japanese with English abstract)

Fukumori I, Benveniste J, Wunsch C, Haidvogel DB (1993) Assimilation of sea surface topography into an ocean circulation model using a steady-state smoother. J Phys Oceanogr 23(8):1831–1855

Fukumori I, Malanotte-Rizzoli P (1995) An approximate Kalman filter for ocean data assimilation: An example with an idealized Gulf Stream model. J Geophys Res 100(C4):6777–6793

Hibiya T, Nagasawa M, Niwa Y (2002) Nonlinear energy transfer within the oceanic internal wave spectrum at mid and high latitudes. J Geophys Res 107(C11):28-1–28-8

Hirose N, Fukumori I, Yoon JH (1999) Assimilation of TOPEX/POSEIDON altimeter data with a reduced gravity model of the Japan Sea. J Oceanogr 55(1):53–64

Hirose N, Fukumori I, Kim CH, Yoon JH (2005) Numerical simulation and satellite altimeter data assimilation of the Japan Sea circulation. Deep Res II Top Stud Oceanogr 52:1443–1463

Hirose N, Kumaki Y, Kaneda A, Ayukawa K, Okei N, Ikeda S, Igeta Y, Watanabe T (2017) Numerical simulation of the abrupt occurrence of strong current in the southeastern Japan Sea. Cont Shelf Res 143:194–205

Hirose N, Takayama K, Moon JH, Watanabe T, Nishida Y (2013) Regional data assimilation system extended to the East Asian marginal seas. Umi Sora (Sea Sky) 89(2):43–51 (in Japanese with English abstract)

James C, Wimbush M, Ichikawa H (1999) Kuroshio meanders in the East China Sea. J Phys Oceanogr 29(2):259–272

Jia Y, Nihous GC, Rajagopalan K (2018) An evaluation of the large-scale implementation of Ocean Thermal Energy Conversion (OTEC) using an ocean general circulation model with low-complexity atmospheric feedback effects. J Mar Sci Eng 6(1):12

Kamachi M, Kuragano T, Ichikawa H, Nakamura H, Nishina A, Isobe A, Ambe D, Arai M, Gohda N, Sugimoto S, Yoshita K, Sakurai T, Uboldi F (2004) Operational data assimilation system for the Kuroshio south of Japan: Reanalysis and validation. J Oceanogr 60(2):303–312

Kashima M, Ito S, Ichikawa K, Imawaki S, Umatani S, Uchida H, Setou T (2009) Quasiperiodic small meanders of the Kuroshio off Cape Ashizuri and their inter-annual modulation caused by quasiperiodic arrivals of mesoscale eddies. J Oceanogr 65(1):73–80

Kawabe M (1980) Sea level variations around the Nansei Islands and the large meander in the Kuroshio south of central Japan. J Oceanogr Soc Jpn 36:227–235

Kodaira T, Waseda T, Nakagawa T, Isoguchi O, Miyazawa Y (2013) Measuring the Kuroshio Current around Miyake Island, a potential site for ocean-current power generation. Int J Offshore Polar Eng 23(4):272–278

Koenig G, Aldebert C, Chevalier C, Devenon JL (2020) Identifying lateral boundary conditions for the M_2 tide in a coastal model using a stochastic gradient descent algorithm. Ocean Model 156(8):101709

Komaki H, Yamashiro T, Jomoto K, Nishina A, Nakamura H, Hirose N (2013) Investigation of the Kuroshio Current in the Tokara Strait for ocean current power generation. J Jpn Soc Civil Eng Ser B3 (Ocean Engineering) 69(2):I_109–I_113 (in Japanese with English abstract)

Korres G, Hoteit I, Triantafyllou G (2007) Data assimilation into a Princeton Ocean Model of the Mediterranean Sea using advanced Kalman filters. J Mar System 65:84–104

Kuroda H, Setou T, Aoki K, Takahashi D, Shimizu M, Watanabe T (2013) A numerical study of the Kuroshio-induced circulation in Tosa Bay, off the southern coast of Japan. Cont Shelf Res 53:50–62

Lee HJ, Yoon JH, Kawamura H, Kang HW (2003) Comparison of RIAMOM and MOM in modeling the East Sea/Japan Sea circulation. Ocean Polar Res 25(3):287–302

Li R, Zhang Z, Wu L (2014) High-resolution modeling study of the Kuroshio path variations south of Japan. Adv Atmos Sci 31:1233–1244

Liu T, Hirose N, Yamada H, Ikegami Y (2020) Estimation of ocean thermal energy potential in the Aguni Basin. App Ocean Res 101:102185

Liu T, Wang B, Hirose N, Yamashiro T, Yamada H (2018) High-resolution modeling of the Kuroshio current power south of Japan. J Ocean Eng Mar Energy 4(1):37–55

Miyazawa Y, Miyama T, Varlamov SM, Guo X, Waseda T (2012) Open and coastal seas interactions south of Japan represented by an ensemble Kalman filter. Ocean Dynam 62:645–659

Nagano A, Ichikawa K, Ichikawa H, Tomita H, Tokinaga H, Konda M (2010) Stable volume and heat transports of the North Pacific subtropical gyre revealed by identifying the Kuroshio in synoptic hydrography south of Japan. J Geophys Res 115:C09002

Nihous GC (2005) An order-of-magnitude estimate of Ocean Thermal Energy Conversion resources. J Energy Resour Technol 127(4):328–333

Nihous GC (2007) A preliminary assessment of Ocean Thermal Energy Conversion resources. J Energy Resour Technol 129(1):10–17

Nihous GC (2007) An estimate of Atlantic Ocean thermal energy conversion (OTEC) resources. Ocean Eng 34(17–18):2210–2221

Nihous GC (2018) A preliminary investigation of the effect of Ocean Thermal Energy Conversion (OTEC) effluent discharge options on global OTEC resources. J Mar Sci Eng 6(1):25

Nagai T, Hibiya T (2013) Effects of tidally induced eddies on sporadic Kuroshio-water intrusion (kyucho). J Oceanogr 69(4):369–377

Nakamura H, Nishina A, Liu Z, Tanaka F, Wimbush M, Park JH (2013) Intermediate and deep water formation in the Okinawa Trough. J Geophys Res 118(12):6881–6893

Nishihama Y, Ikeda M (2007) Kuroshio extension variability explored through assimilation of TOPEX/POSEIDON altimeter data into a quasi-geostrophic model. J Oceanogr 63(6):879–895

Nishina A, Nakamura H, Park JH, Hasegawa D, Tanaka Y, Seo S, Hibiya T (2016) Deep ventilation in the Okinawa Trough induced by Kerama Gap overflow. J Geophys Res Oceans 121(8):6092–6102

Niwa Y, Hibiya T (2004) Three-dimensional numerical simulation of M_2 internal tides in the East China Sea. J Geophys Res 109:C04027

Noh Y, Kim HJ (1999) Simulations of temperature and turbulence structure of the oceanic boundary layer with the improved near-surface process. J Geophys Res 104(C7):15621–15634

Qiu B, Toda T, Imasato N (1990) On Kuroshio front fluctuations in the East China Sea using satellite and in situ observational data. J Geophys Res 95(C10):18191–18204

Rajagopalan K, Nihous GC (2013) An assessment of global Ocean Thermal Energy Conversion resources with a high-resolution ocean general circulation model. J Energy Resour Technol 135(4):041202

Rajagopalan K, Nihous GC (2013) An assessment of global Ocean Thermal Energy Conversion resources under broad geographical constraints. J Renew Sustain Energy 5(6):063124

Rajagopalan K, Nihous GC (2013) Estimates of global Ocean Thermal Energy Conversion (OTEC) resources using an ocean general circulation model. Renew Energy 50:532–540

Roberts A, Thomas B, Sewell P, Khan Z, Balmain S, Gillman J (2016) Current tidal power technologies and their suitability for applications in coastal and marine areas. J Ocean Eng Mar Energy 2:227–245

Sakamoto TT, Hasumi H, Ishii M, Emori S, Suzuki T, Nishimura T, Sumi A (2005) Responses of the Kuroshio and the Kuroshio Extension to global warming in a high-resolution climate model. Geophys Res Lett 32(14):L14617

Schafstall J, Dengler M, Brandt P, Bange H (2010) Tidal-induced mixing and diapycnal nutrient fluxes in the Mauritanian upwelling region. J Geophys Res 115:C10014

Smagorinsky J (1963) General circulation experiments with the primitive equations: I. The basic experiment. Mon Weather Rev 91(3):99–164

Smedstad OM, Fox DN (1994) Assimilation of altimeter data in a two-layer primitive equation model of the Gulf Stream. J Phys Oceanogr 24(2):305–325

Smedstad OM, Fox DN, Hurlburt HE, Jacobs GA, Metzger EJ, Mitchell JL (1997) Altimeter data assimilation into a 1/8° eddy resolving model of the Pacific Ocean. J Met Soc Japan 75(1B):429–444

Sugimoto T, Kimura S, Miyaji K (1988) Meander of the Kuroshio front and current variability in the East China Sea. J Oceanogr Soc Jpn 44:125–135

Taft B (1972) Characteristics of the flow of the Kuroshio south of Japan. In: Stommel H, yoshida K (eds) Kuroshio: its physical aspects. University of Tokyo Press, Tokyo, pp 165–216

Takeuchi J, Honda N, Morikawa Y, Koike T, Nagata Y (1998) Bifurcation current along the southwest coast of the Kii Peninsula. J Oceanogr 54:45–52

Thomson RE, Emery WJ (2014) Chapter 5 - Time series analysis methods. In: Thomson RE, Emery WJ (eds) Data analysis methods in physical oceanography (Third Edition). Elsevier, Boston, pp. 425–591

Ul Haque SMS, Hadi AM, Ahmed S, Rehman A, Fareed A (2017) Feasibility of OTEC in Arabian Sea. Int J Min Metall Mech Eng 5(1):11–17

Usui N, Fujii Y, Sakamato K, Kamachi M (2015) Development of a four-dimensional variational assimilation system for coastal data assimilation around Japan. Mon Weather Rev 143(1):3874–3892

Usui N, Tsujino H, Fujii Y, Kamachi M (2008) Generation of a trigger meander for the 2004 Kuroshio large meander. J Geophys Res 113:C01012

Usui N, Tsujino H, Nakano H, Matsumoto S (2013) Long-term variability of the Kuroshio path south of Japan. J Oceanogr 69:647–670

Usui N, Wakamatsu T, Tanaka Y, Hirose N, Toyoda T, Nishikawa S, Fujii Y, Takatsuki Y, Igarashi H, Nishikawa H, Ishikawa Y, Kuragano T, Kamachi M (2017) Four-dimensional variational ocean reanalysis: a 30-year high-resolution dataset in the western North Pacific (FORA-WNP30). J Oceanogr 73(2):205–233

Van Zwienten JH, Rauchenstein LT, Lee L (2017) An assessment of Florida's ocean thermal energy conversion (OTEC) resource. Renew Sust Energy Rev 75:683–691

Wicaksono YB, Putri MR (2018) Study of ocean thermal energy resources in Para'baya, West Sulawes. IOP Conf Ser 162:012037

Wick GL, Schmitt WR (1977) Prospects for renewable energy from the sea. Mar Technol Soc J 11(5/6):16–21

Wu CR, Shaw PT, Chao SY (1999) Assimilating altimetric data into a South China Sea model. J Geophys Res 104(C12):29987–30005